NASA-CR-205018

ANALYSIS OF TECHNOLOGY FOR SOLID STATE COHERENT LIDAR

IN ... ...
... ...
O ... T
038430

CONTRACT No. NAS8-38609

Delivery Order No. 178

Contract Period:
September 20, 1996 - June 30, 1997

Submitted To:

NASA/MSFC
Marshall Space Flight Center, AL 35812

Prepared By:
Farzin Amzajerdian
Center For Applied Optics
University Of Alabama In Huntsville
Huntsville, Al 35899
(205) 890-6030 ext. 452

June 30, 1997

UAH/CAO

FOREWORD

ACKNOWLEDGMENTS

CONTENTS

1.0 INTRODUCTION

Over past few years, considerable advances have been made in the areas of the diode-pumped, eye-safe, solid state lasers and room temperature, wide bandwidth, semiconductor detectors operating in the near-infrared region. These advances have created new possibilities for the development of low-cost, reliable, and compact coherent lidar systems for measurements of atmospheric winds and aerosol backscattering from a space-based platform.

The work performed by the UAH personnel under this Delivery Order concentrated on design and analyses of solid state pulsed coherent lidar systems capable of measuring atmospheric winds from space, and design and perform laboratory experiments and measurements in support of solid state laser radar remote sensing systems which are to be designed, deployed, and used by NASA to measure atmospheric processes and constituents. Under this delivery order, a lidar testbed system was designed and analyzed by considering the major space operational and environmental requirements, and its associated physical constraints. The lidar optical system include a wedge scanner and the compact telescope designed by the UAH personnel. The other major optical components included in the design and analyses were: polarizing beam splitter, routing mirrors, wave plates, signal beam derotator, and lag angle compensator. The testbed lidar optical train was designed and analyzed, and different design options for mounting and packaging the lidar subsystems and components and support structure were investigated. All the optical components are to be mounted in a stress-free and stable manner to allow easy integration and alignment, and for a long term stability. The lidar structure and all of its mechanical components were specified to be fabricated or procured by NASA/MSFC. The necessary optical components including the routing mirrors, polarizing beam splitter, waveplates and lenses were also specified to be procured. Once this lidar system is integrated, the NASA/MSFC existing 100 mJ laser will be used to align and test it. In the future, the MSFC 100 mJ laser may be replaced by the 500 mJ transmitter laser under development at NASA/LaRC and the frequency-agile local oscillator laser being developed at the NASA Jet Propulsion Laboratory. This lidar system is also intended to be used for evaluating the performance of various lidar subsystems and components that are to be integrated into a flight unit and for demonstrating the integrity of the signal processing algorithms by performing actual atmospheric measurements from a ground station.

A number of laboratory experiments and measurements were performed at the NASA/MSFC Detector Characterization Facility, previously developed by the UAH personnel. These laboratory measurements include the characterization of a 2-micron InGaAs detectors suitable for use in coherent lidars, characterization of a Diffractive Optical Element Scanner, and measurement of compact lidar telescope.

UAH personnel actively participated in the development of performance and operational requirements for the development of the high pulse energy transmitter laser and frequency-agile local oscillator laser, that are in-progress at NASA Langley Research Center and Jet Propulsion Laboratory. During the period of performance of this delivery order, UAH personnel participated several technical coordination meetings with the other NASA centers, and attended several meetings and conferences to report on the progresses and accomplishments made under this work.

2.0 LIDAR OPTICAL DESIGN AND ANALYSES

The lidar optical subsystem has two major functions: first, it expands the laser beam and directs it toward the atmosphere in a conical scan. Second, it receives the backscattered radiation, compensates for the scanner and spacecraft motions, and directs it toward the lidar photodetector to be effectively mixed with the optical local oscillator. The optical subsystem consists of a large-aperture telescope, a laser beam scanner, a signal beam de-rotator, a lag angle compensator, and an automatic alignment mechanism. The signal beam de-rotator and the lag angle compensator correct for the predictable signal beam misalignment due to the scanner and spacecraft motions, respectively, and the automatic alignment mechanism corrects any residual misalignment that may occur during the launch or during the lidar operation in the orbit.

Previously, an optical design study was performed that resulted in the development of compact and robust designs for the lidar telescope, scanner, and de-rotator. The telescope design is based on a novel off-axis catadioptric configuration that uses a parabolic mirror as its primary and a combination of a hyperbolic mirror and an off-axis negative lens as its secondary. A 25-cm version of this telescope was then fabricated at NASA MSFC and UAH facilities. The scanner is a Silicon prism with about a 9 degree wedge angle for deflecting the laser beam through an angle of 30 degrees. By rotating this "optical wedge" about a fixed axis along the input beam, a conical scan pattern can be generated. A 28-cm Silicon prism was also specified and acquired by MSFC. The de-rotator, which compensates for the continuous scanner motion, utilizes a monolithic optical element for maintaining the received signal beam direction along a constant axis to the lidar photodetector.

Under this delivery order, the design and development of the remaining components of the optical subsystem that includes the lag angle compensator and autoalignment mechanism were addressed. One of the objectives of this task was to study the possible sources of misalignment for a space-based coherent Doppler lidar and investigate different active and passive alignment maintaining technologies suitable for the lidar operation in space. The other objective of this task was to specify the requirements for the lag angle compensation and autoalignment, and to design and analyze an advanced lag angle compensator, and to investigate various autoalignment mechanism concepts.

In a Doppler laser radar system, utilizing optical heterodyne detection, the relative alignment of the received signal with respect to the local oscillator beam is particularly critical. There are several sources of misalignment for a space-based coherent Doppler lidar that need to be quantified and, if necessary, compensated for by using passive and active alignment correction mechanisms. There are two classes of alignment correction for a space-based lidar, referred to as static (slant range to atmospheric target) and dynamic (slant depth of atmospheric target) corrections. Static correction occurs during the pulse round trip time to the top of the atmospheric sensing volume. Dynamic correction occurs during the atmospheric signal reception time. In general, the static corrections are easier to do than the dynamic corrections because of the much longer time (lower bandwidth) associated with the static corrections. For a 20 km measurement

depth, the pulse reception time is about 160 microseconds and the pulse round trip time for a 830 km orbit altitude is about 6.6 milliseconds.

The predictable sources of misalignment in space are the scanner continuous motion, the spacecraft continuous nadir tipping, and changes in spacecraft altitude, pointing and velocity. Unpredictable sources of misalignment include spacecraft vibrations, instrument variations due to launch forces, and lidar optical subsystem thermal expansions and contractions in orbit. Table 1 summarizes the specifications for two different missions that have been proposed and used as baselines for this study.

Table 1. Shuttle And NPOESS Preliminary Mission Specifications

	Shuttle	NPOESS
Aperture (cm)	25	50
Pulse Energy (mJ)	100	500
PRF (Hz)	10	20
Scan Angel (deg.)	30	30
Orbit Altitude (km)	300 (300-400)	833
Spacecraft Velocity (m/s)	7733	7442

Table 2 and 3 categorizes the misalignments associated with the Shuttle and NPOESS platforms and specify their magnitudes. In these tables the type of alignment correction mechanism associated with each misalignment have also been provided.

For the purpose of this study, the scanner has been assumed to be a continuous conical scanner as opposed to a step-stare scanner which will not require any scanner corrections. A continuous motion scanner will require both static and dynamic corrections. In this case, as the laser energy reflects off the atmospheric aerosols and travels back to the lidar telescope, the scanner continues to move. This causes the received signal beam to follow a different path through the telescope than that of the transmitted beam. Therefore, as the scanner continues to rotate and the transmitted beam sweeps a conical pattern in the atmosphere, the received signal beam orbits about the transmitter/local oscillator (LO) optical axis that extends to the lidar photodetector.

Table 2. Predictable Misalignment

Shuttle \ NPOESS	Nadir Tipping	Continuous Scanner Rotation
Target Range **"Static"**	3 µrad Ignore / 7 µrad Steering Mirror	1 mrad De-rotator / 3 mrad De-rotator
Target Depth **"Dynamic"**	0.2 µrad Ignore / 0.2 µrad Ignore	80 µrad Steering Mirror / 80 µrad Steering Mirror

Table 3. Unpredictable Misalignment

Shuttle \ NPOESS	Target Depth 160 µs	Target Range 2-6 ms	PRF 0.1 s	Scanner Rotation 6 s	Orbit 90 min	Mission
Zero Mean Random σ < X µrad	Mech Design / MD	MD / MD	N/A	N/A	N/A	N/A
Fixed Sudden	N/A	N/A	N/A	N/A	Search Mirror / SM/Det Array	N/A
Fixed Gradual	N/A	N/A	N/A	N/A	TBD / TBD	TBD / TBD

For the purpose of this study, the scanner has been assumed to be a continuous conical scanner as opposed to a step-stare scanner which will not require any scanner corrections. A continuous motion scanner will require both static and dynamic corrections. In this case, as the laser energy reflects off the atmospheric aerosols and travels back to the lidar telescope, the scanner continues to move. This causes the received signal beam to follow a different path through the telescope than that of the transmitted beam. Therefore, as the scanner continues to rotate and the transmitted beam sweeps a conical pattern in the atmosphere, the received signal beam orbits about the transmitter/local oscillator (LO) optical axis that extends to the lidar photodetector. Fortunately, it was shown earlier that the scanner continuous motion can be compensated, in a relatively easy manner, by using a small substrate with a shallow wedge angle . We refer to this mechanism as the signal beam "de-rotator". The de-rotator performs two functions: changing the signal beam direction to be always parallel to the transmitter/LO optical axis, and translating the signal beam to lie directly on the optical axis that coincides with the LO beam and extends to the photodetector. By synchronizing the rotation of the de-rotator about the optical axis with that of the scanner, the signal beam is maintained along the optical axis and aligned with respect to the LO beam.

The spacecraft continuous nadir tipping, due to orbiting the earth, introduces the next largest misalignment angle, which is about an order of magnitude smaller than the misalignment due to the scanner continuous motion. We refer to this misalignment as the signal beam "Lag Angle". For an 830 km orbit, the static portion of this misalignment is about 7 microradians, which has to be compensated. However, the dynamic portion of the spacecraft nadir tipping is less than 0.2 microradians which can be neglected without any degradation in the system performance. In this study, the variations in the size of the lag angle effect were also considered. These variations are caused by the natural changes in the spacecraft altitude, orbital velocity and pointing. Using a set of typical spacecraft specifications, it was shown that these spacecraft orbital variations will introduce less than 0.3 microradians change in the lag angle. This is well within 3 microradians misalignment budget for a 50 cm telescope aperture diameter.

A single two-axis steering mirror concept has been devised to perform the lag angle compensation. The two-axis concept will also allow correction of any unpredictable fixed and zero mean variable misalignments that may be introduced during the launch or during the lidar operation on orbit. The correction for the variable misalignments may not be necessary depending on the lidar opto-mechanical design, the spacecraft type, and the vibration characteristics of other instruments onboard. Therefore, further analysis is required to determine if this capability should be included in the instrument design. If necessary, operational and design requirements will be defined. We name the technology that corrects any fixed unpredictable misalignment errors the autoalignment (AA) technology. The autoalignment mechanism must be capable of detecting the transmitter, LO, or signal beam misalignment magnitude and direction, and then realigning the errant beam using an active control loop. The misalignment error may be measured using the large signal from the surface return or using onboard alignment sensors.

2.1   Signal Beam Derotator

Based on the revised optical layout design, the derotator were defined and optimized with SYNOPSYS optical design software. The derotator element material was chosen to be Zinc Sulfide (ZnS), becuase of its relatively high index of refraction and its high transmission at both 2-micron and visible wavelengths. The derotator substrate specifications are:

Wedge angle = 0.9716^0
Thicknees = 9 mm
Diameter = 25.4 mm
Material = ZnS)

Using this design, the wave front errors were analyzed for the derotator rotations of 180 and 90 degrees. The top, bottom, and right most field of view rays have been traced through the system, and the resultant beam wandering has been analyzed and verified.
The derotator optical prescription and along with other transmitter/receiver optical elements that were used in this analysis are provided in the following pages.

The design and performance of the derotator are summerized in figures 1-11. Figures 1-3 show the derotator optical layout and position with the telescope top FOV rays, and figure 4 shows the corresponding wavefront model at the derotator exit pupil. Figures 5-8 are similar plots for the telescope bottom FOV rays, and figures 9-11 show the telescope right FOV rays. Figure 12 shows the derotator element fabrication drawing.

Polarization is off, coatings are ignored.
WARNING -- WAVEFRONT COORDS. ROTATED
MIXED GENERIC ANALYSIS MAY BE INACCURATE.

EVALUATING IMAGE AT WAVELENGTH   2.06700 REL. FIELD   1.00000   0.00000
COORD XFRM   0.1257E-10 -0.8074E-11 0.1571E+01 ILLUM. COSINE   0.1000E+01
UNVIGNETTED F/NUMBER IN YZ PLANE: 0.2609E+01

RAYS THRU PUPIL   THRU LENS ENERGY/RAY LENS TRANS

         293   293   0.100000E+01   0.100000E+01
   VARIANCE   STD. DEV.   STREHL R.   XIP   YIP
  0.259736E-04 0.509643E-02   0.998975   0.211263E-06 0.700194E-16
IMAGE
IMAGE> SYNOPSYS AI> RLE P
ID CLRTBDT-CLR TEL BREAD BOARD TESTING   51
WAVL   2.077000   2.067000   2.057000
APS   1
AFOCAL
GLOBAL
UNITS   MM
OBB 0.00   0.08021 125.00000   0.00000   0.08021   0.00000   125.00000
  0 AIR
  1 CV   0.00000000   TH   225.00000000
  1 AIR
  2 CAO   137.50000000   0.00000000   187.50000000
  2 RAD   -412.13152000   TH   -175.00232000
  2 CC   -1.00000000
  2 -AIR
  2 DECEN   0.00000000   -187.50000000   0.00000000 39
  2 AT   0.00000000   0.00000000 39
  3 CAO   30.00000000   0.00000000   30.00000000
  3 RAD   -89.19634000   TH   65.86275000
  3 CC   -3.49767000
  3 AIR
  4 CAO   10.00000000   0.00000000   10.00000000
  4 CV   0.00000000   TH   1.20000000
  4 N1   1.51962377   N2   1.51979280   N3   1.51996117
  4 GTB   U   'CRQZB   '
  5 CAO   10.00000000   0.00000000   10.00000000
  5 CV   0.00000000   TH   6.80000000
  5 AIR
  6 CAO   10.00000000   0.00000000   10.00000000
  6 RAD   181.66308000   TH   3.29231000
  6 CC   -6.79070000
  6 N1   2.26411995   N2   2.26421831   N3   2.26431764
  6 GTB   U   'ZNS   '
  7 CAO   10.00000000   0.00000000   10.00000000
  7 RAD   28.58489000   TH   42.00000000
  7 CC   -0.81789800
  7 AIR
  8 CV   0.00000000   TH   8.00000000
  8 N1   1.43707900   N2   1.43723589   N3   1.43739199
  8 GTB   U   'FUSILB   '
  8 DECEN   0.00000000   7.50000000   0.00000000 29
  8 GT   -90.00000000   0.00000000 29
  8 PRISM   RANGLE   1.60000000E+01
 10 TH   -42.00000000
 11 CV   0.00000000   TH   -9.23892362
 11 N1   -2.26411995   N2   -2.26421831   N3   -2.26431764
 11 GTB   U   'ZNS   '
 11 DECEN   0.00000000   0.00000000   0.00000000   3
 11 AT   UAH/CAO .00000001   0.00000000

```
   .. DECEN        0.00000000              0.00000000         0.00000000   1
12 BT          0.97160686              0.00000000      1
13 CV          0.00000000    TH       -50.00000000
13 -AIR
14 CV          0.00000000    TH        0.00000000
14 -AIR
15 CV          0.00000000    TH        0.00000000
15 -AIR
END
```

CLEAR APERTURE DATA
(Y-coordinate only)

SURF	X OR R-APER.	Y-APER.	REMARK	X-OFFSET	Y-OFFSET
1	125.0000		Soft CAO		
2	137.5000		User CAO	0.0000	187.5000
3	30.0000		User CAO	0.0000	30.0000
4	10.0000		User CAO	0.0000	10.0000
5	10.0000		User CAO	0.0000	10.0000
6	10.0000		User CAO	0.0000	10.0000
7	10.0000		User CAO	0.0000	10.0000
8	8.1727		Soft CAO		
9	8.4486		Soft CAO		
10	8.7245		Soft CAO		
11	15.9938		Soft CAO		
12	19.0861		Soft CAO		
13	19.4163		Soft CAO		
14	19.8420		Soft CAO		
15	19.8420		Soft CAO		

NOTE: CAO, CAI, EAO, and EAI input is semi-aperture.
      RAO and RAI input is full aperture.

UNUSUAL APERTURE DATA

SURF   APERTURE SPECIFICATIONS

8	POLYGON APERTURE WITH 4 VERTICES (OUTSIDE)

```
          X          Y
       8.0000     8.0000
       8.0000    -8.0000
      -8.0000    -8.0000
      -8.0000     8.0000
```

9	POLYGON APERTURE WITH 4 VERTICES (OUTSIDE)

```
          X          Y
       8.0000    11.3137
       8.0000   -11.3137
      -8.0000   -11.3137
      -8.0000    11.3137
```

10	POLYGON APERTURE WITH 4 VERTICES (OUTSIDE)

```
          X          Y
       8.0000     8.0000
       8.0000    -8.0000
      -8.0000    -8.0000
      -8.0000     8.0000
```

UAH/CAO   8

IMAGE
PHYSICAL OPTICS ANALYSIS

Polarization is off, coatings are ignored.
    0.100000E+00   50   0.000000E+00   0.000000E+00   0.000000E+00   0.000000E+00
  IMAGE> SYNOPSYS AI> IMAGE
  PHYSICAL OPTICS ANALYSIS

Polarization is off, coatings are ignored.
FORMAT: VARIANCE (ICOL/M) HBAR NRYS 0 GBAR [XIP YIP]
         ----   ---- ----   ---- --- ---

  IMAGE> WARNING -- WAVEFRONT COORDS. ROTATED
MIXED GENERIC ANALYSIS MAY BE INACCURATE.

EVALUATING IMAGE AT WAVELENGTH   2.06700 REL. FIELD   -1.00000   0.00000
COORD XFRM   -0.1255E-10   0.6492E-04   0.1571E+01 ILLUM. COSINE   0.1000E+01
UNVIGNETTED F/NUMBER IN YZ PLANE: 0.2622E+01

RAYS THRU PUPIL   THRU LENS   ENERGY/RAY   LENS TRANS

        293   293   0.100000E+01   0.100000E+01
    VARIANCE   STD. DEV.   STREHL R.   XIP   YIP
  0.374719E-04   0.612143E-02   0.998522   0.472035E-06   0.110471E-15
  0.374719E-04   0.612143E-02   0.998522   0.472035E-06   0.110471E-15
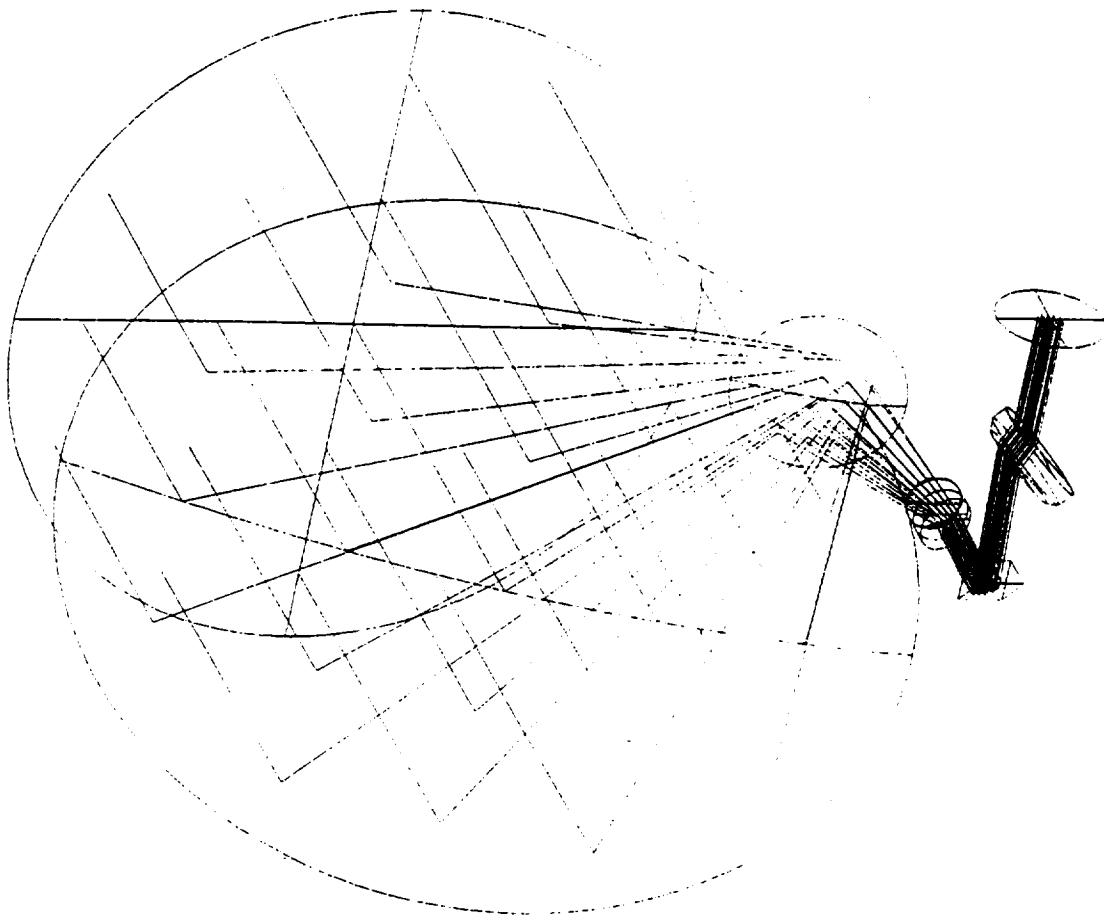
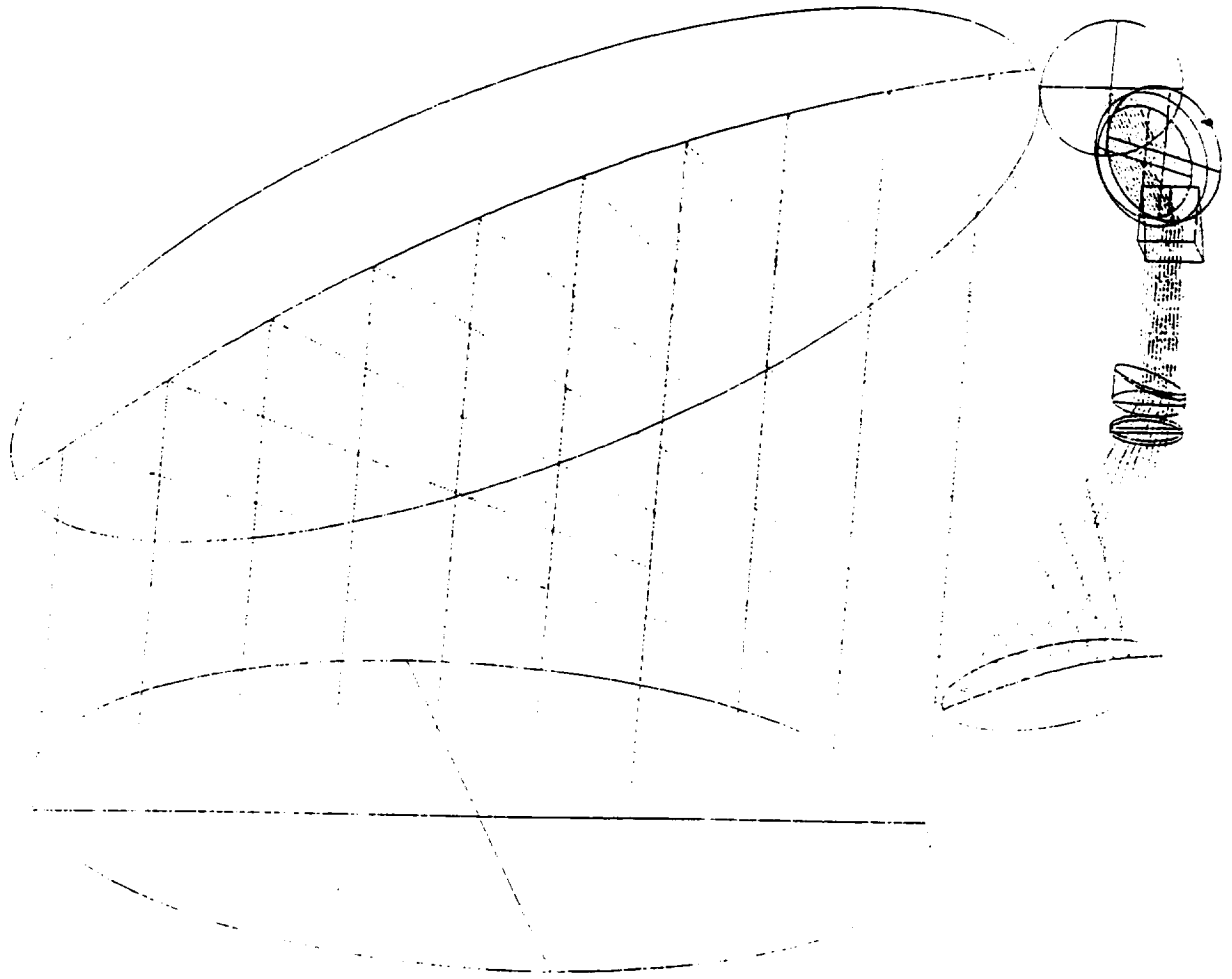Fig.1 Optical layout and derotator position, and the telescope top FOV rays.

Fig. 2 Optical layout and derotator position viewed from 90 degrees azimuth, and the telescope top FOV rays.
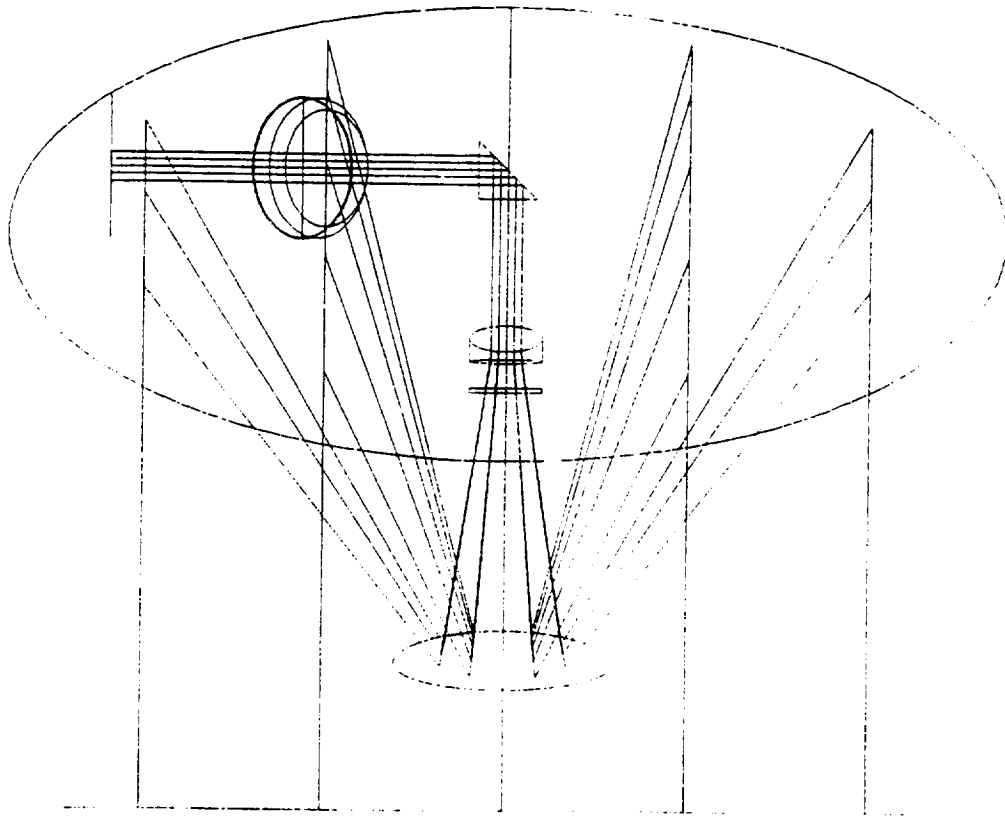
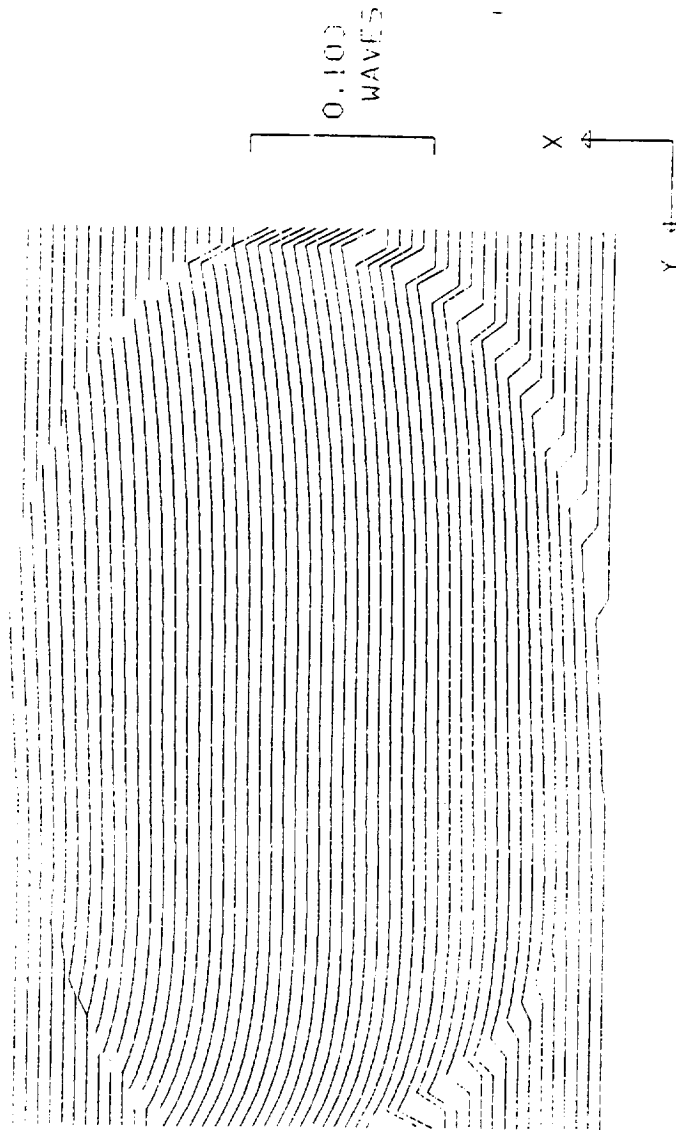Fig. 3 Optical layout and derotator position viewed from 0 degree azimuth, and the telescope top FOV rays.

Fig. 4 Wavefront model for the top FOV (Standard deviation = 0.005 waves).
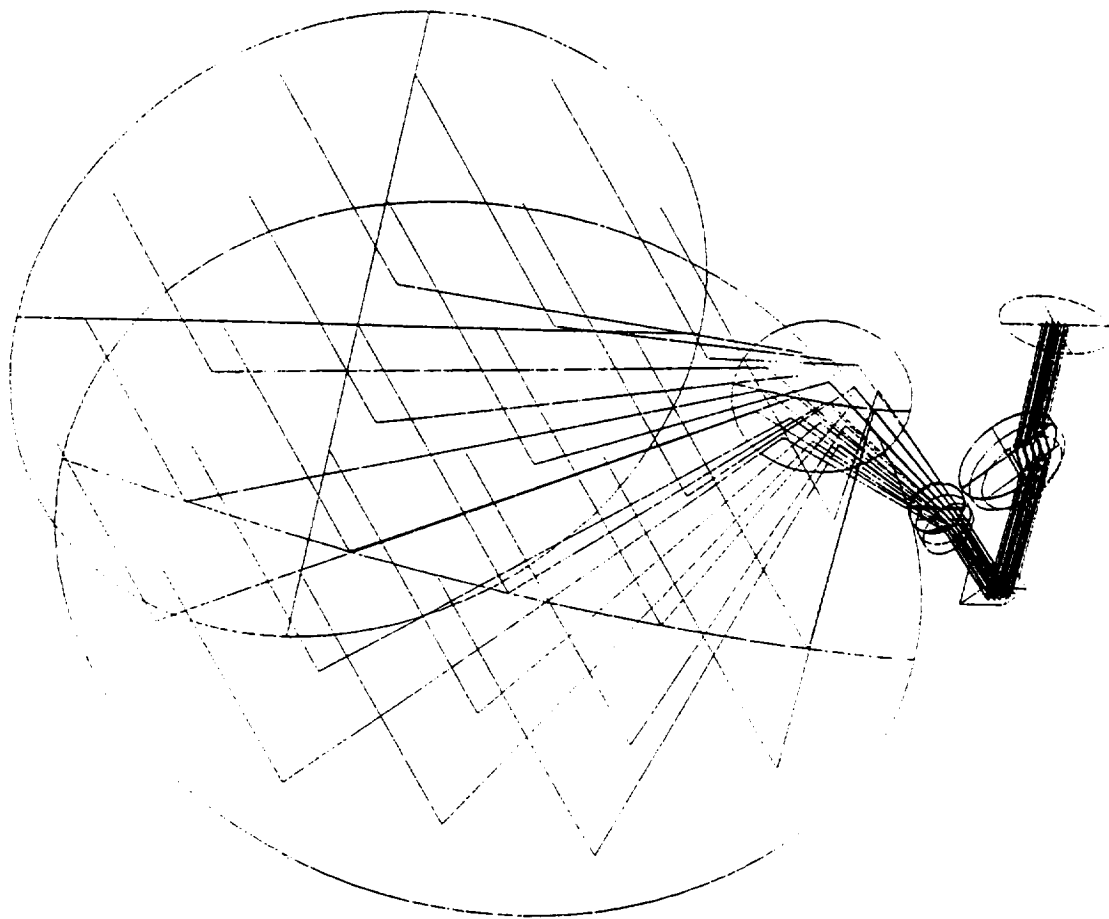
Fig.5 Optical layout and derotator position, and the telescope bottom FOV rays.
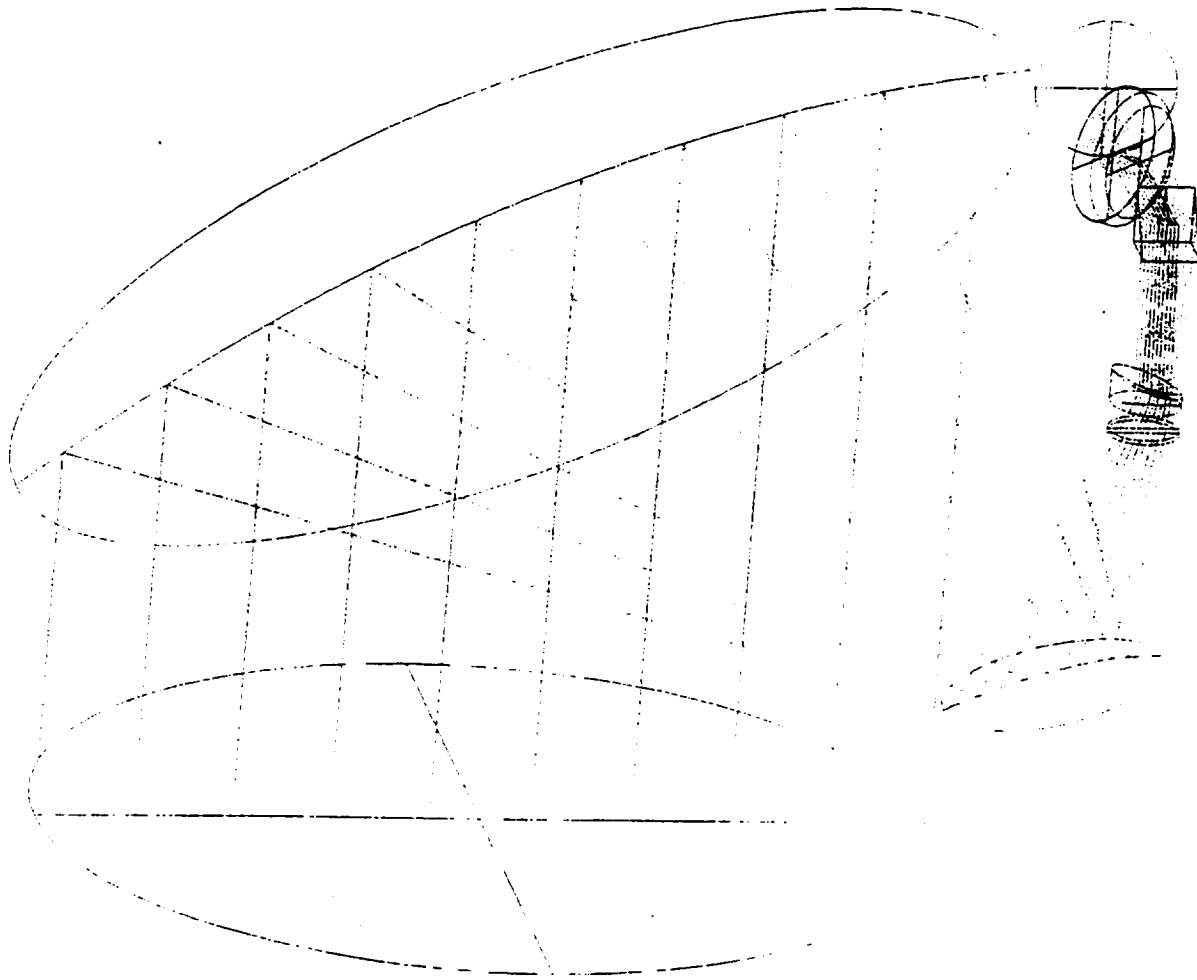
Fig. 6 Optical layout and derotator position viewed from 90 degrees azimuth, and the telescope bottom FOV rays.

Fig. 7 Optical layout and derotator position viewed from 0 degree azimuth, and the telescope bottom FOV rays.

Fig. 8 Wavefront model for the bottom FOV (Standard deviation = 0.006 waves).
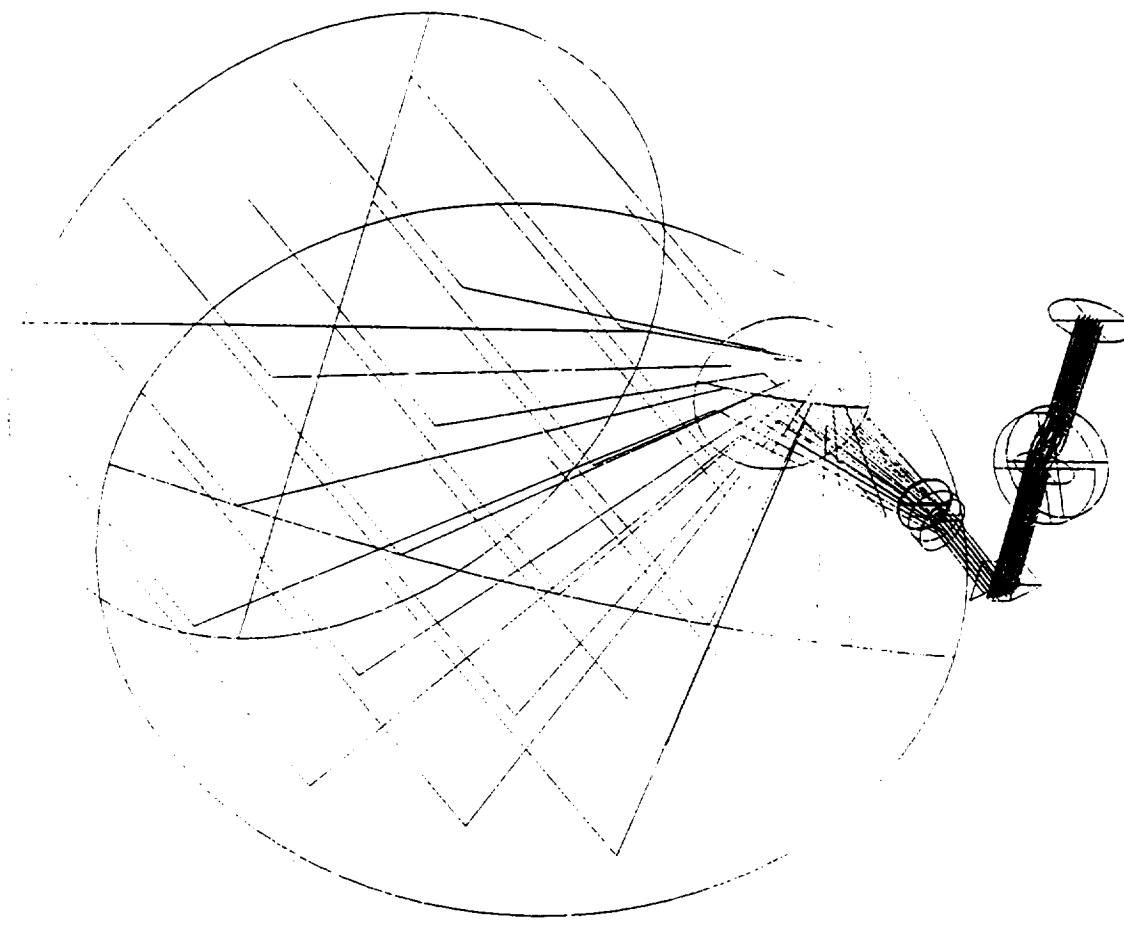
Fig. 9 Optical layout and derotator position viewed from 120 degrees azimuth, and the telescope right FOV rays.

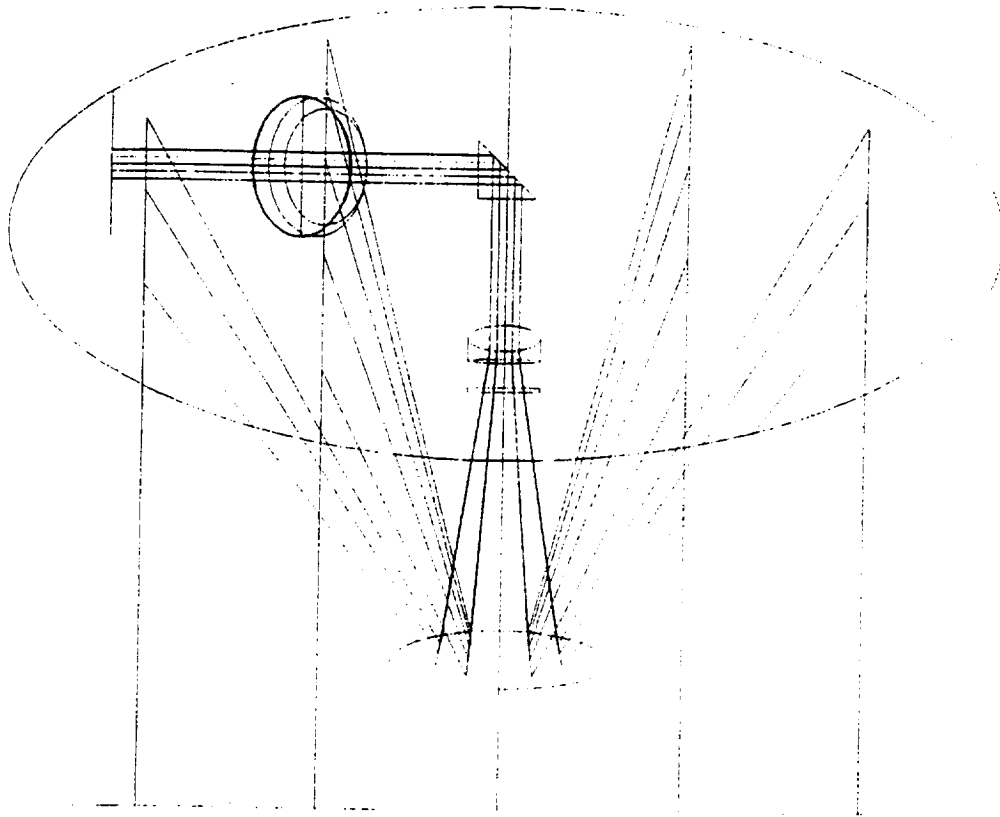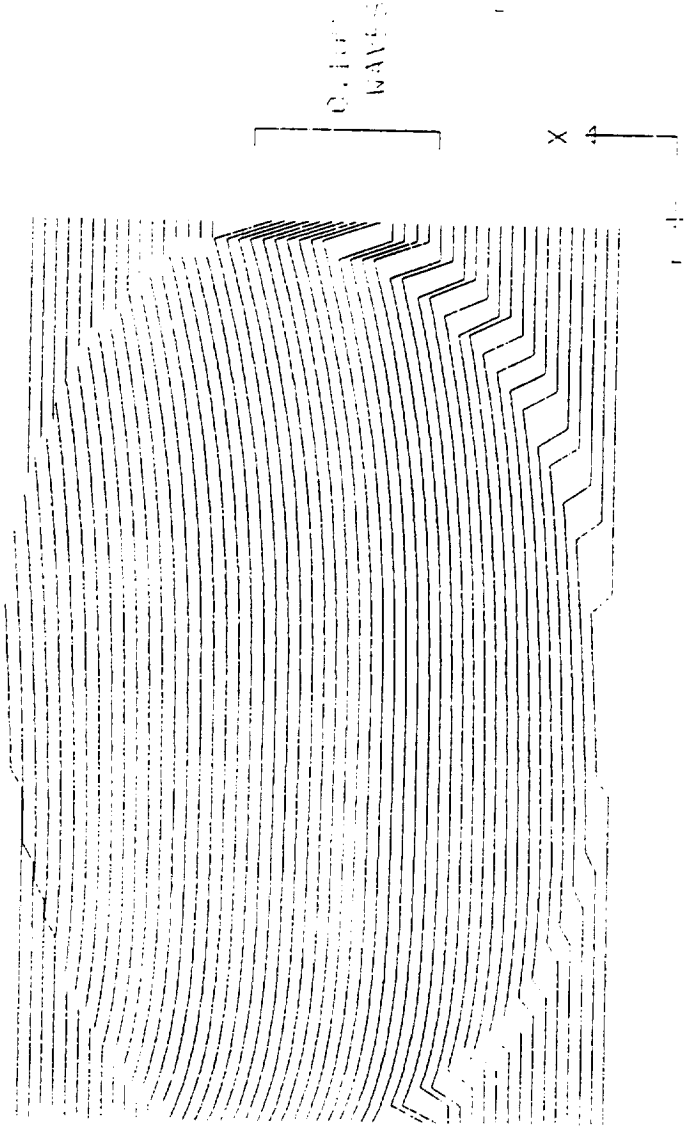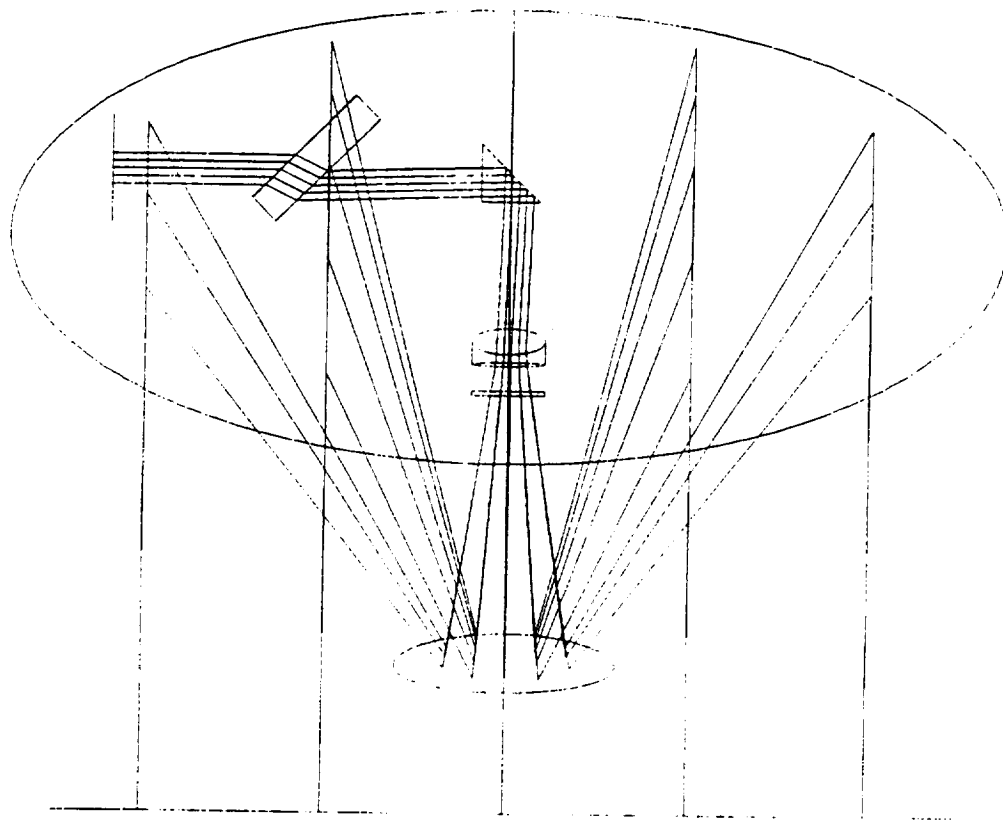Fig. 10 Optical layout and derotator position viewed from 90 degrees azimuth, and the telescope right FOV rays.
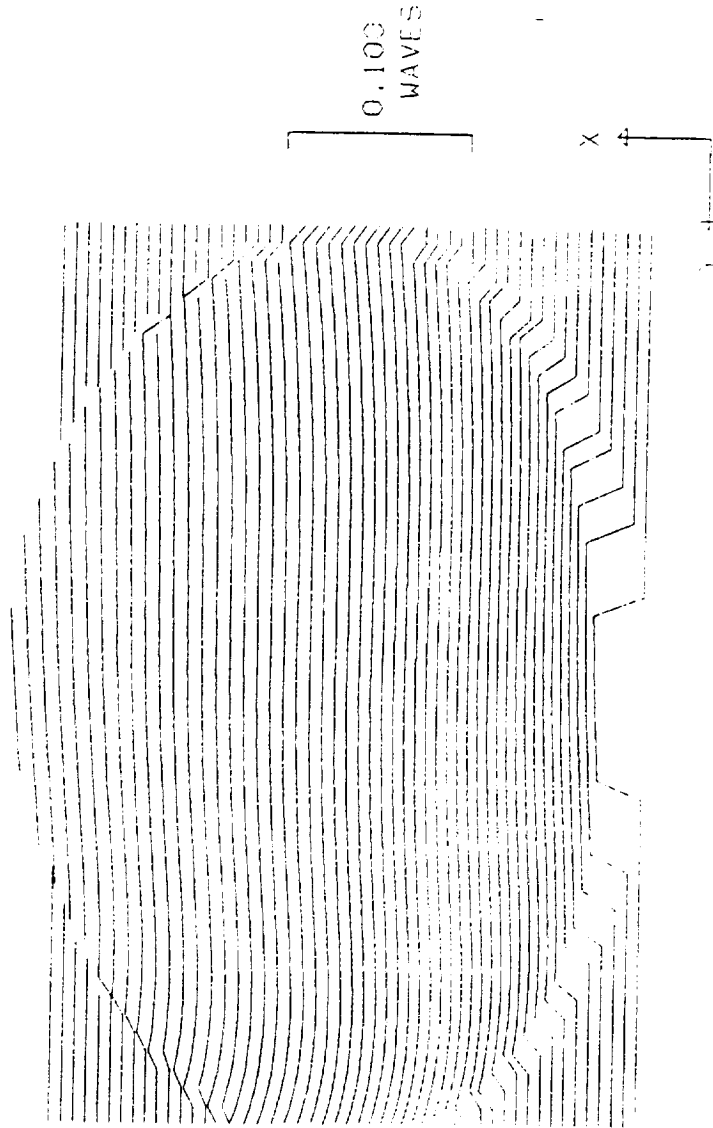
Fig. 11 Wavefront model for the right FOV (Standard deviation = 0.006 waves).

PARAMETERS	SIDE 1	SIDE 2
RADIUS OF CURVATURE	R1 INFINITE	R2 INFINITE
RADIUS TOLERANCE		
TOLERANCE		
IRREG. TOLERANCE		
FINISH		
COATING		
CLEAR AP.	S1 25.0000	S2 25.0000
SAGITTA DIA.	Y1 0.00000	Y2 0.00000
DIA. FACE	B1 27.2860	B2 27.2860
DIA. BEVEL	Y1 25.2540	Y2 25.2540
FACE WIDTH	D1 1.0160	D2 1.0160
BEVEL WIDTH	C1 0.1270	C2 0.1270
FACE ANGLE		
WEDGE ANGLE	TH 9.2389	
THICKNESS	0.9716°	
THK. TOL.		
WEDGE TOL.		
FLAT TIR		
DIAMETER	DIA 27.5400	
DIA. TOL.		
DIAMETERAL ZNS.		
GRADE	CLEAR-TRAN	
MINIMUM		
MELT		
PART		
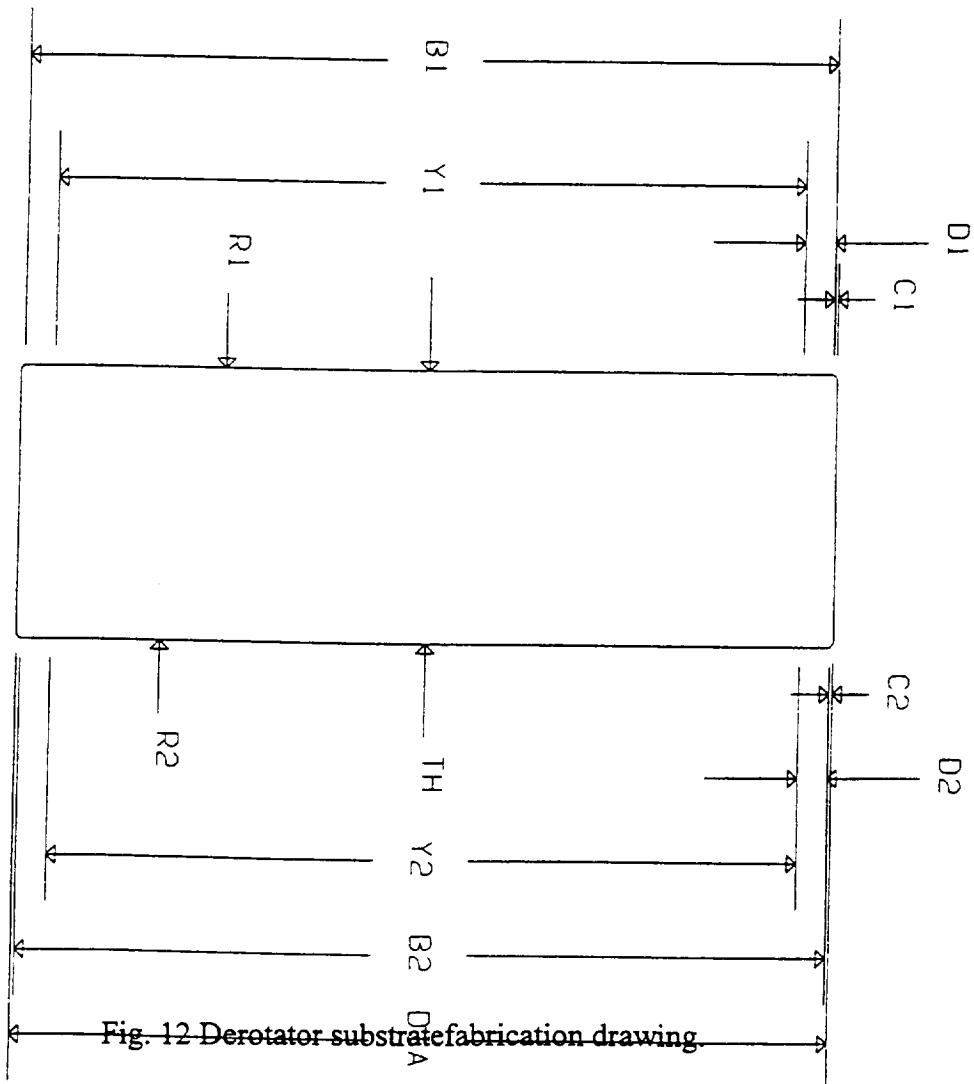
Fig. 12 Derotator substrate fabrication drawing.

SCALE	4.000 X	
DATE	02-24-199?	
DESIGNER		APPROVED
CHECKER		
TEST WAVL		SYNOPSYS LOG 63
DIMENSIONS mm		

NUMBER
REV.

DEROTATOR

2.2   Lag Angle Compensator

A single two-axis steering mirror concept has been devised to perform the lag angle compensation. The two-axis concept will also allow correction of any unpredictable fixed and zero mean variable misalignments that may be introduced during the launch or during the lidar operation on orbit. The correction for the variable misalignments may not be necessary depending on the lidar opto-mechanical design, the spacecraft type, and the vibration characteristics of other instruments onboard. Therefore, further analysis is required to determine if this capability should be included in the instrument design. If necessary, operational and design requirements will be defined. We name the technology that corrects any fixed unpredictable misalignment errors the autoalignment (AA) technology. The autoalignment mechanism must be capable of detecting the transmitter, LO, or signal beam misalignment magnitude and direction, and then realigning the errant beam using an active control loop. The misalignment error may be measured using the large signal from the surface return or using onboard alignment sensors.

The LAC/AA two-axis mirror will be driven by a pointing controller using the laser pulse timing and the scanner encoder signals, the spacecraft inertial navigation and GPS data, and perhaps the data from a network of alignment sensors or the signal from the earth surface. At this time, both piezoelectric and magnetorestrictive actuators are being considered for controlling the mirror motion. It should be noted that the alignment tolerance of 3 microradians refers to the telescope input (space side), and is relaxed by the telescope magnification for the signal beam de-rotator and LAC/AA mirror. For example, for a 25X telescope that is being carried in the design points, the alignment tolerance is 75 microradians on the lidar side of the telescope.

The lag angle compensator (LAC) is misnamed because it must correct for other misalignments besides lag angle. The $80\mu r$ angular misalignment due to the clocking of the primary wedge during PRT is a prime example. Perhaps it should be called something like "beam misalignment compensator". Another question is whether the various real misalignments can be taken care of by one tilt actuated mirror, especially if the compensations required are at odds with each other in some way. For example, is one misalignment telling the BMC to move one way while another misalignment is telling it to move a different way.

One would like the incident beam footprint on the BMC to be centered at the mirror pivot point (which should be at the center of the mirror). This would allow the beam to be centered on the imaging lens prior to the detector. However, the derotator will nutate the incident beam in an elliptical path on the BMC (circular path if BMC were normal to the beam). The beams emerging from the derotator are parallel and collimated but decentered with respect to each other. This means that the beam incident on the imaging lens will nutate in a circle about the lens optical axis. There will be an angle on the beam after the imaging lens, and this angle will nutate in a cone about the detector location. Obviously, this angle will have to be kept small if we are to avoid SNR loss. That means a long focal length. But then the diffraction spot size gets bigger on the detector. However, when we throw other beam misalignments in the mix (such as the 2 mr residual during PRT) which the BMC is suppose to remove, then the path traced out on the

imaging lens will no longer be circular, and the beam tilt emerging on the other side will vary in direction and magnitude. These issues will need closer examination.

Using the optical design developed earlier for a space-based coherent lidar, the receiver optical train has been modeled on the ZEMAX optical design and analysis code. This model will allow for defining the range and resolution requirements of the LAC/AA mirror motion, and specifying the receiver optical and mechanical tolerances. The following sections define the major parameters necessary required for defining the LAC requirements. As a baseline, the lidar has been assumed to be operating from a Shuttle orbit and have a 50 cm telescope.

2.2.1 Beam Footprint Size At Target

The probe beam leaves the 50 cm diameter aperture of the telescope collimated. The slant range to the top of the atmosphere is 381 km. The beam footprint size at this location will depend upon whether the beam footprint can be considered to be in the far field. If so, then the footprint size can be determine using the Fraunhoffer diffraction approximation. The ratio of the telescope aperture squared divided by the range should be much less than the operational wavelength:

$$(25)^2 / (3.81 \times 10^7) = 1.64 \times 10^{-5} \text{ cm} = 0.16 \text{ microns}$$

This is smaller than the operational wavelength by a factor of 12. This is sufficient to allow us to use the Frauhoffer diffraction approximation, i.e. we can get the beam footprint size by taking the Fourier Transform of the telescope pupil.

$$F\{cyl (r/d)\} = (d^2/4) \text{ Somb}(d\rho) \qquad (1)$$

where $\rho = r/\lambda z$ in the image plane.

The first zero of the diffraction pattern occurs when:

$$d\rho = 1.22 \qquad (2)$$

Substituting for ρ yields

$$r = (1.22 \ \lambda \ z)/ d \qquad (3)$$

where $\lambda = 2 \ \mu$; $z = 381$ km; $d = 50$ cm.

This yields a beam footprint diameter of $Dfp = 3.72$ meters at the top of the atmosphere.

2.2.2 Speckle Size At Entrance Pupil

This illuminated spot on top of the atmosphere acts like a coherent diffuse source when viewed by the Receiver telescope. This means that there will be a laser speckle pattern in the plane of the Receiver entrance pupil. The size of the speckle grain can be found from:

$$dg = 2.4 \lambda z / Dfp \qquad (4)$$

Using the values λ, z, and Dfp from above...

$$dg = 54.24 \text{ cm}$$

Thus the typical speckle grain size is roughly the same as diameter of the telescope entrance pupil.

2.2.3 Detector Considerations

Beat Signal

The intensity at the detector due to two coherent light fields of slightly different frequencies is given by Eq.5 (where r & p refer to reference and probe beams respectively):

$$I(t) = B [(Ir + Ip) + \sqrt{Ir Ip} \cos\{(\omega r - \omega p)t + (\phi r - \phi p)\}] \qquad (5)$$

The second term in Eq.5 is the beat signal. The mean square beat signal is

$$MSBS = B^2 Ir Ip \qquad (6)$$

As already mentioned, the returning probe signal is extemely weak. However, if we are detecting the MSBS, then increasing the strength of the reference increases the MSBS.

Signal/Noise

In classical interferometry, the greater the mismatch between Ir and Ip in terms of power the lower the fringe contrast. However, if we take the ratio of the MSBS with the MSNS (mean square noise signal), we obtain the SNR:

$$SNR = (\eta \ Ir \ Ip)/[h\nu \ \Delta\omega \ (Ir + Ip)] \qquad (7)$$

As the strength of the reference gets large compare to the probe, Ip in the denominator becomes insignificant and can be ignored. Then Ir cancels out leaving:

$$SNR = (h\eta/ h\nu \ \Delta\omega) \ Ip \qquad (8)$$

Coherence Condition At Detector

Suppose the reference and probe beams are of equal intensity and fall normally on two side-by-side square detectors. If the OPD between the two beams is zero, then each detector puts out the same in-phase beat signal. If we add the two signals, they reinforce each other Next, suppose that for one detector the two incident wavefronts are separated by an OPD of a half wave. Now the two signals from the detectors are out of phase by 180 degrees. If we add them, they cancel each other out This same signal cancellation would happen if we replaced the two detectors with one having twice the size.

Beam Tilt and Footprint at Detector

The above behavior implies a maximum allowable tilt tolerance between the two wavefronts at the detector. The worst case is if there is an OPD of a half wave across the detector. For the 75 micron LIDAR detector, the half wave constraint imposes a limiting tilt between probe and reference wavefronts of 13.3 mr.

As an example, suppose that the lens feeding the detector has a 100 mm focal length. For a planar probe wavefront tilted 13.3 mr at the input side of the focusing lens, the beam footprint at the detector will shift laterally 1.33 mm. If the input beam diameter is 20 mm, the beam footprint (Airy Disc) size at the detector will be around 24 microns. In this case, the beam will have shifted entirely off the detector. The message...the limit set by coherence is not self-sufficient but must be considered within the context of the overall optical design.

2.2.4 Important Time Scales of the LIDAR

The following *assumes* a LIDAR altitude of 350 km, an orbital speed of 7.5 km/sec, and a 30 degree conscan angle. This yields a slant range to the ground of 404.14 km. (The wedge generating the conscan rotates at 60 degrees/sec.) The laser probe pulse length at the resonator is 0.2 microseconds. These numbers are not cast in concrete and are subject to some revision. Their use here is simply to help indentify key time scales important for angular alignment of the return beam. (The value for the velocity of light used here is 2.99793×10^5 km/sec.)

There are two critical time scales of interest. The first is the pulse round trip time (PRTT) between the LIDAR and the ground along the slant path. This is 2696 microseconds. The second is the pulse reception time (PRT) due to continuous light scattering through the 23 km atmospheric slant path. This is 154.6 microseconds. During PRTT the primary wedge will have rotated 0.162 degrees, and the satellite will have moved about 20.2 meters along its orbital path. During PRT the primary wedge will have rotated 0.009 degrees, and the satellite will have moved 1.16 meters.

2.2.5 Beam Alignment Issues

It is critical that the LIDAR probe beam be accurately aligned to the local reference beam (which is itself aligned to the system optical axis) during their mutual interaction with the detector. This

alignment tolerance is 75 microradians in exit pupil space. There are two broad classes of alignment correction. The first is "anticipated correction" which occurs before the probe beam re-enters the LIDAR telescope. This happens during PRTT. The second is "dynamic correction" which occurs during active illumination of the detector by the probe beam. This happens during PRT. There are several induced return beam misalignments due to wedge rotation and satellite motion.

Beam Alignment Issue 1

The primary scanning wedge is Germanium. To generate a 30 degree beam tilt on the outgoing beam requires that the inherent wedge angle be 8.789 degrees. If there were no conscan then the return beam would be perfectly compensated and realigned with the telescope optical axis. However, with conscan the probe beam re-entering the optical system will see a different clocking of the primary wedge than when it left. This introduces entrance pupil angular cross-coupling into an orthogonal axis of 1396 microradians during PRTT, and 80 microradians during PRT.

The probe beam can be realigned by a compensation wedge (derotator) oriented 90.162 degrees with respect to the primary wedge. The compensation wedge must also rotate continuously at 60 degrees/sec. Only anticipated correction can be accomplished by the derotator. The 80 microradian dynamic correction must be accomplished with the LAC mirror.

Beam Alignment Issue 2

a. Lag Angle

The satellite attitude control continuously orients the LIDAR telescope so that it points toward nadir. During a PRTT this means that the telescope is now pointing with a 3 microradian offset relative to the return beam (as shown in Figure 13). This is called lag angle. The component designated LAC in Figure 14 must provide anticipated correction during PRTT such that when the probe beam is incident on LAC, the reflected beam will be parallel to the system optical axis. Note: During PRT, the lag angle change is 0.17 microradians (at the entrance pupil) and requires no dynamic correction by the LAC mirror.

b. Variation in Lag Angle

The lag angle is subject to change due to variations in altitude, orbital velocity, and spacecraft pointing. Table 4 shows the size of these changes for changes in altitude of ±20 km, velocity changes of ±7 m/s, and pointing changes of ± 0.10. These parameter changes are based on theoretical predictions. It can be seen from Table 1 that the induced lag angle changes are well under the 3 microradian tolerance.
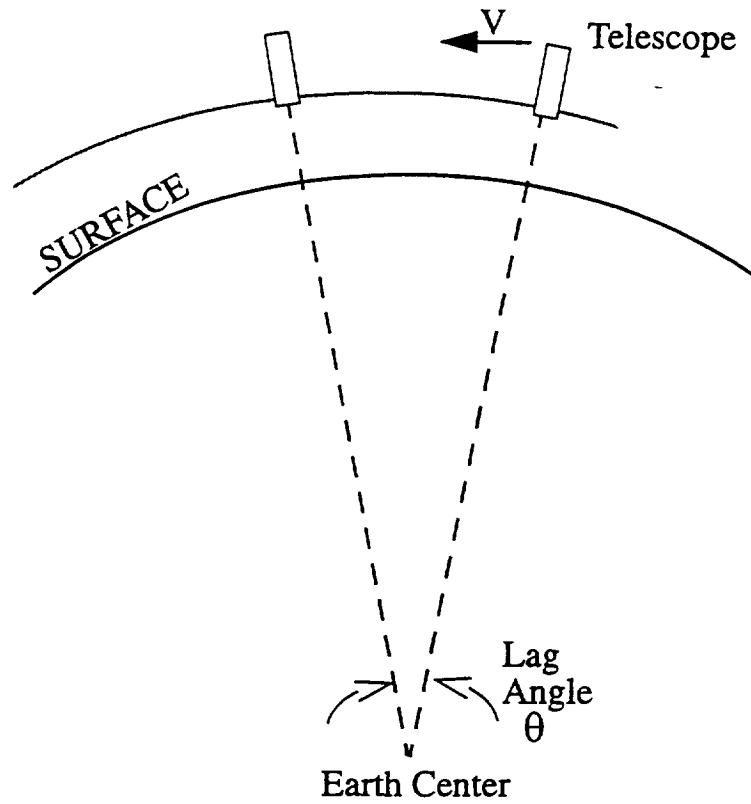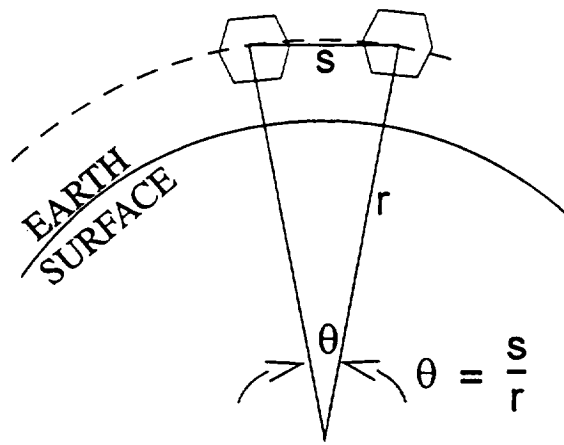
Figure 13. Lag Angle due to spacecraft motion.

$$\theta = \frac{s}{r}$$

$$r = 6371 + 350 \text{ km}$$
$$S = 2.7 \text{ ms} \times 7.5 \text{ km/s}$$
$$= 20.2 \text{ m}$$

Figure 14. Lag angle during the pulse round trip time.

Table 4. Lang Angle Variations

Orbit Parameter	Variation	Change in Lag Angle
Altitude	+/- 20 km	+/- 0.16 µrad
Orbital Velocity	+/- 7 m/s	+/- 0.003 µrad
Pointing	+/- 0.1 deg	+/- 0.003 µrad

C. Lag Variation With Wedge Orientation

What kind of lag angle variation might we expect as the probe beam is launched at different azimuth angles relative to the ground track of the satellite? As a *first cut* at this problem we examine the difference in lag angle for two extreme cases: A) the beam launched at 1800; B) the beam launched at 0^0. We *assume* that the average round trip time is 2.696 ms and that the satellite has moved 20.22 m along its orbital path in that time. We also assume that the travel time from the pupil to the ground is the same for both cases, i.e.1.348 ms.

Light returning from the ground footprint will have a little further to go because the satellite is moving away in Case A. The path will be shorter for Case B because the satellite is moving toward the ground footprint. The total round trip time will be different for each case which means the lag angle will also be different.

We find the length of the return slant path by:

$$L_{RSP} = \sqrt{(350 \text{ km})^2 + (202.072 \text{ km} \pm 20.22 \text{ m})^2}$$

The difference in transit time is 0.067 µs, which leads to a lag angle change of 0.07 nr.

Beam Alignment Issue 3

a. Surface Angular Offset

The lag angle discussed previously was measured from the center of the Earth due to nadir tipping of the platform. There is another angular offset due to the displacement of the spacecraft along its orbital path during PRTT as measured from the surface of the Earth. This offset is 43.3 µr. This assumes that as soon as the light leaves the telescope pupil it no longer shares in the orbital motion of the satellite. This means that the probe beam strikes the Earth as if from a stationary platform. Justification is found in the dictum: "The speed of light is independent of the motion of the source." However, the work done by R.Gudimetlal of Oregon Graduate Institute has shown

that this 43.3 μr offset angle should not actually occur because of self-compensating effects pre-dicted by special relativity.

b. Variation in Surface Angular Offset

If the surface angular offset is not taken care of by special relativity effects, the variation in this angle as a function of changes in altitude, orbital velocity, and look angle (pointing) is about +/- 0.045 micro-radian and can be ignored.

b. Surface Angular Offset Due to Atmospheric Thickness

Again, if special relativity doesn't enter into it, the surface angular offset change due to scatter from the top of the atmosphere vs that from the ground is negligible.

Beam Alignment Issue 4

For centuries, astronomers have had to introduce an angular offset when observing the "station-ary" stars to compensate for the orbital motion of the Earth around the Sun. This phenomenon is called "stellar aberration". The compensation is accomplished by tilting the telescope by an amount given by the ratio of the orbital velocity to the speed of light (i.e. v/c).

At first glance, there appears to be a potentially equivalent effect for the orbiting LIDAR telescope. It is moving relative to a stationary source on the ground. The ratio of orbital velocity to the speed of light introduces a 25 microradian angular offset. If this is a "real" effect, the LAC mirror must compensate for it.

The lag angle compensator (LAC) is misnamed because it must correct for other misalignments besides lag angle. The 80μr angular misalignment due to the clocking of the primary wedge dur-ing PRT is a prime example. Perhaps it should be called something like "beam misalignment compensator". Another question is whether the various real misalignments can be taken care of by one tilt actuated mirror, especially if the compensations required are at odds with each other in some way. For example, is one misalignment telling the BMC to move one way while another misalignment is telling it to move a different way.

One would like the incident beam footprint on the BMC to be centered at the mirror pivot point (which should be at the center of the mirror). This would allow the beam to be centered on the imaging lens prior to the detector. However, the derotator will nutate the incident beam in an elliptical path on the BMC (circular path if BMC were normal to the beam). The beams emerging from the derotator are parallel and collimated but decentered with respect to each other. This means that the beam incident on the imaging lens will nutate in a circle about the lens optical axis. There will be an angle on the beam after the imaging lens, and this angle will nutate in a cone about the detector location. Obviously, this angle will have to be kept small if we are to avoid SNR loss. That means a long focal length. But then the diffraction spot size gets bigger on the detector. However, when we throw other beam misalignments in the mix (such as the 2 mr

residual during PRT) which the BMC is suppose to remove, then the path traced out on the imaging lens will no longer be circular, and the beam tilt emerging on the other side will vary in direction and magnitude. These issues will need closer examination.

2.3 Polarization and coating analysis

The primary and secondary mirrors of the 25 cm lidar telescope, developed by the UAH personnel, has been gold plated. Therefore, it became necessar to perform a polarization and coating analysis to better define the telescope performance. As part of this effort, a polarization ray tracing analysis and a polarization mapping function modeling were performed. It was then shown that the output intensity is 97.8 % of input at 2.067 mm wavelength.

The polarization mapping function is shown in figure 15, and the polarization ray tracing and intensity data are provided in the preceding pages.
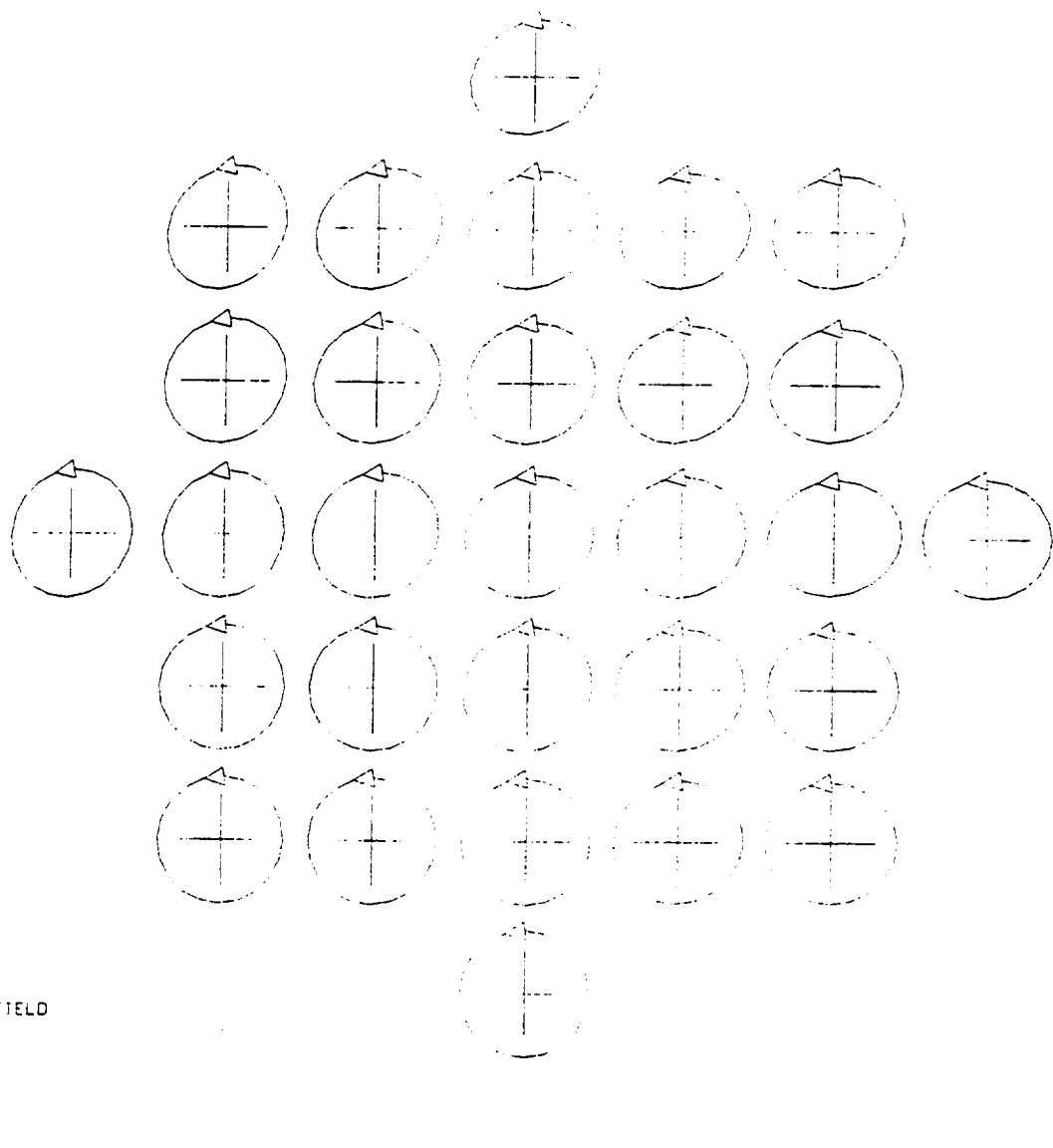
Figure 15. Polarization mapping of gold-plated telescope.

```
      STACK DATA
      CONTROL WAVELENGTH =    2.0000 MICRONS
      CONTROL ANGLE =     0.000 DEG.


                        OPTICAL    PHYSICAL
            SURF NO.    THICKNESS  THICKNESS   INDEX    IMAG. INDEX
                        (WAVES)    (MICRONS)
         INCIDENT MEDIUM                       1.0000
              2         0.0000     0.000000    1.0000
         SUBSTRATE                             0.5460    13.9000

SYNOPSYS AI> SURF. NO.    COATING
-------------------
   1 Dummy surface
   2 CUSTOM COATING  2
   3 CUSTOM COATING  2
SYNOPSYS AI
    SURF. NO.   MAGN.          X              Y              Z            PHASE
-------------------------------------------------------------------------------
Incid. S  1 0.707107E+00  0.000000E+00  0.707107E+00  0.000000E+00  0.000000E+00
Incid. P  1 0.707107E+00  0.707107E+00  0.000000E+00  0.000000E+00  0.900000E+02
Refr.  S  1 0.707107E+00  0.000000E+00  0.707107E+00  0.000000E+00  0.000000E+00
Refr.  P  1 0.707107E+00  0.707107E+00  0.000000E+00  0.000000E+00  0.900000E+02
Incid. S  2 0.707107E+00  0.707107E+00  0.000000E+00  0.000000E+00  0.900000E+02
Incid. P  2 0.707107E+00  0.000000E+00 -0.707107E+00  0.000000E+00  0.180000E+03
Refl.  S  2 0.703504E+00  0.703504E+00  0.000000E+00  0.000000E+00 -0.825215E+02
Refl.  P  2 0.702758E+00  0.000000E+00  0.461731E+00 -0.529786E+00  0.189028E+03
Incid. S  3 0.703504E+00  0.703504E+00  0.000000E+00  0.000000E+00 -0.825215E+02
Incid. P  3 0.702758E+00  0.000000E+00  0.461731E+00 -0.529786E+00 -0.170972E+03
Refl.  S  3 0.700177E+00  0.700177E+00  0.000000E+00  0.000000E+00 -0.255579E+03
Refl.  P  3 0.698104E+00  0.000000E+00 -0.672005E+00 -0.189097E+00 -0.161247E+03
V1: (X,Y,Z),Phase  0.700177E+00   0.000000E+00   0.000000E+00 -0.255579E+03
V2: (X,Y,Z),Phase  0.000000E+00  -0.672005E+00  -0.189097E+00 -0.161247E+03
INTENSITY: Apod., Polar., Prod.  0.100000E+01  0.977596E+00  0.977596E+00
SYNOPSYS AI
    SURF. NO.   MAGN.          X              Y              Z            PHASE
-------------------------------------------------------------------------------
Incid. S  1 0.707107E+00 -0.707107E+00  0.000000E+00  0.000000E+00 -0.900000E+02
Incid. P  1 0.707106E+00  0.000000E+00  0.707106E+00 -0.989898E-03  0.000000E+00
Refr.  S  1 0.707107E+00 -0.707107E+00  0.000000E+00  0.000000E+00 -0.900000E+02
Refr.  P  1 0.707106E+00  0.000000E+00  0.707106E+00 -0.989898E-03  0.000000E+00
Incid. S  2 0.707107E+00  0.707107E+00  0.000000E+00  0.000000E+00  0.900000E+02
Incid. P  2 0.707106E+00  0.000000E+00 -0.707106E+00  0.989898E-03 -0.180000E+03
Refl.  S  2 0.703503E+00  0.703503E+00  0.000000E+00  0.000000E+00 -0.825185E+02
Refl.  P  2 0.702759E+00  0.000000E+00  0.461930E+00 -0.529614E+00 -0.170975E+03
Incid. S  3 0.703503E+00  0.703503E+00  0.000000E+00  0.000000E+00 -0.825185E+02
Incid. P  3 0.702759E+00  0.000000E+00  0.461930E+00 -0.529614E+00 -0.170975E+03
Refl.  S  3 0.700169E+00  0.700169E+00  0.000000E+00  0.000000E+00 -0.255563E+03
Refl.  P  3 0.698114E+00  0.000000E+00 -0.673078E+00 -0.185279E+00 -0.161269E+03
V1: (X,Y,Z),Phase  0.700169E+00   0.000000E+00   0.000000E+00 -0.255563E+03
V2: (X,Y,Z),Phase  0.000000E+00  -0.673078E+00  -0.185279E+00 -0.161269E+03
INTENSITY: Apod., Polar., Prod.  0.100000E+01  0.977600E+00  0.977600E+00
SYNOPSYS AI>  IMAGE> Rayset  Thru lens  Energy/Ray  Energy Thru  *Polarization
    293       293       0.100000E+0  0.100000E+01   0.977435E+00
IMAGE
IMAGE
```

SYSTEM SPECIFICATIONS

OBJECT DISTANCE	(TH0)	INFINITE	FOCAL LENGTH	(FOCL)	679.0055
OBJECT HEIGHT	(YPP0)	INFINITE	BACK FOCAL LENGTH		102.3569
MARG RAY HEIGHT	(YMP1)	125.0000	IMAGE DISTANCE	(BACK)	102.3569
MARG RAY ANGLE	(UMP0)	0.0000	CELL LENGTH	(TOTL)	49.9977
CHIEF RAY HEIGHT	(YPP1)	0.0000	F/NUMBER	(FNUM)	2.7160
CHIEF RAY ANGLE	(UPP0)	0.0802	GAUSSIAN IMAGE HT	(GIHT)	0.9506
ENTR PUPIL SEMI-APERTURE		125.0000	EXIT PUPIL SEMI-APERTURE		27.2176
ENTR PUPIL LOCATION		0.0000	EXIT PUPIL LOCATION		-45.4904

X-OBJECT HEIGHT	(XPP0)	INFINITE			
X-MARG RAY HEIGHT	(XMP1)	125.0000	X-CHIEF RAY HT	(XPP1)	0.0000
X-MARG RAY ANGLE	(VMP0)	0.0000	X-CHIEF RAY ANGLE	(VPP0)	0.0802

WAVL (uM)	2.07700	2.06700	2.05700
UNITS		MM	
APERTURE STOP SURFACE (APS)		1	SEMI-APERTURE 125.00000
FOCAL MODE		ON	
MAGNIFICATION		-6.79005E-10	
GLOBAL OPTION		ON	

POLARIZATION MODE IS ON.
OBJECT IS CIRCULAR-RIGHT.

SURFACE DATA

SURF	RADIUS	THICKNESS	MEDIUM	INDEX	V-NUMBER
0	INFINITE	INFINITE	AIR		
APS	INFINITE	225.00000	AIR		
2A	-412.13152 O	-175.00232	-AIR		
3	-89.19634 O	102.35687S	AIR		
IMG	INFINITE				

KEY TO SYMBOLS

A	SURFACE HAS TILTS AND DECENTERS	B	TAG ON SURFACE
G	SURFACE IS IN GLOBAL COORDINATE	L	SURFACE IS IN LOCAL COORDINATE
O	SPECIAL SURFACE TYPE	P	ITEM IS SUBJECT TO PICKUP
S	ITEM IS SUBJECT TO SOLVE		

SPECIAL SURFACE DATA

SURFACE NO. 2 -- CONIC SURFACE
CONIC CONSTANT (CC) -1.000000
SEMI-MAJOR AXIS (b) -4.121315E+12   SEMI-MINOR AXIS (a)   4.121315E+07

SURFACE NO. 3 -- CONIC SURFACE
CONIC CONSTANT (CC) -3.497670
SEMI-MAJOR AXIS (b) 35.711819   SEMI-MINOR AXIS (a)   -56.439025

TILTS AND DECENTERS DATA

SURF	TYPE	X	Y	Z	ALPHA	BETA	GAMMA
2	REL	0.00000	-187.50000	0.00000	0.0000	0.0000	0.0000

KEY TO SURFACE TYPES

GLB   GLOBAL COORDINATES   LOC   LOCAL COORDINATES

2.4 Detector focusing lens design

A simple Plano convex lens with focal length of 100 mm and a beam splitter of 2 mm thick have been placed behind the derotator to focus the receiving 10 mm beam to the detector. The point spread function (diffraction intensity) pattern is shown in figure 16. The airy disk radius is about 26 μm. It should be noted that the signal beam pattern can be further improved depending on the local oscillator beam spread function at the detector surface.
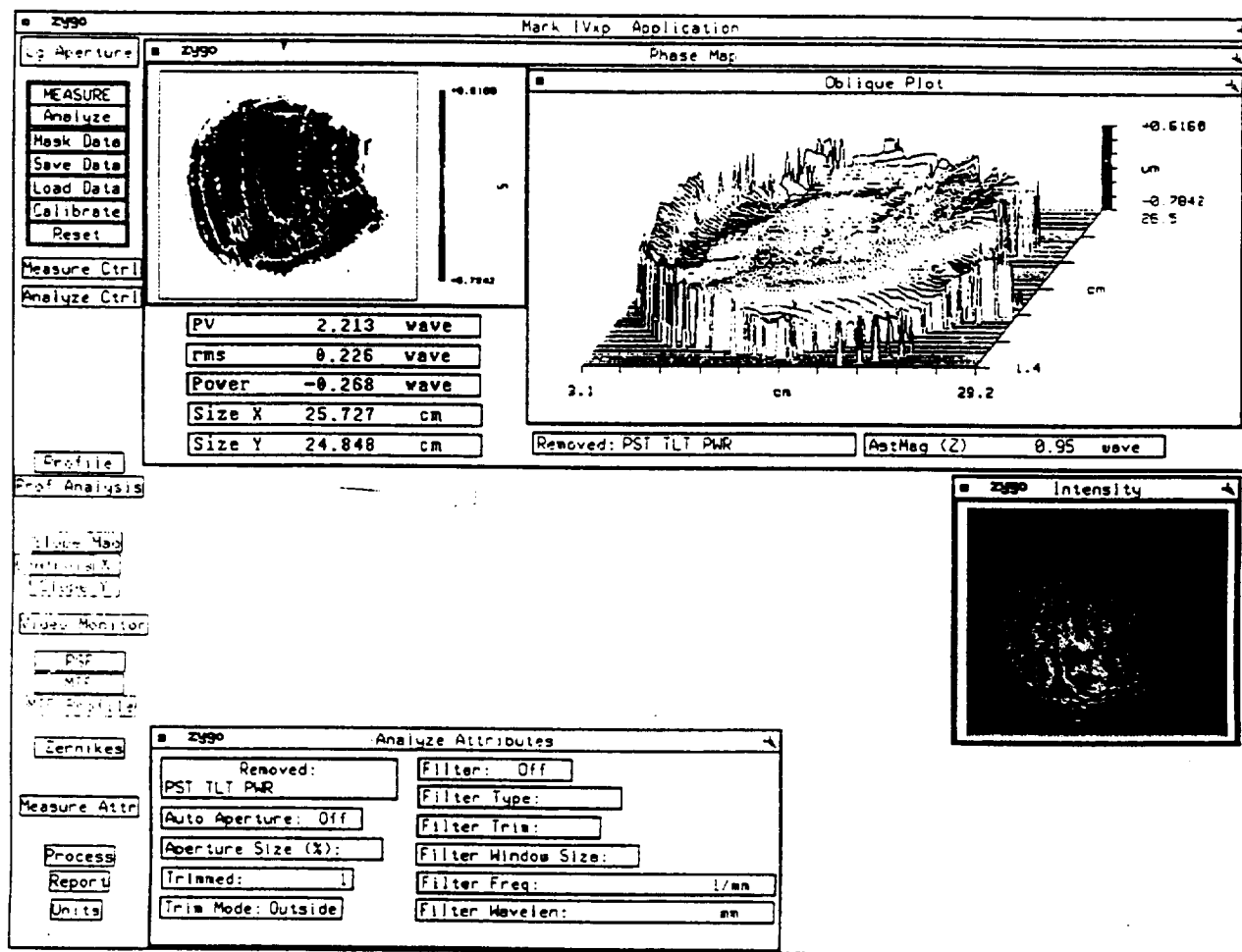

Figure 16. Signal beam diffraction intensity pattern at the detector surface.

2.5   Telescope Testing

The telescope primary mirror was characterized using a ZYGO interferometer operating at 633 nm wavelength. The ZYGO measurements provided the figure error and surface finish data. Figure 17 illustrates the results of this measurement which are also listed below.

Figure Error   peak-to-valley   2.2 wave at 633 nm   0.674 wave at 2.067 μm
               RMS   0.23 wave at 633 nm   0.07 wave at 2.067 μm

Surface Finish   Estimated RMS   50 Angstroms

The surface finish of the secondary mirror was measured by a WYKO interferometer using the. Taly-surf method. The RMS value of the surface finish for the secondary mirror was mmeasured to be 26 Angstroms. It should be noted that these measurements were performed prior to gold plating the mirrors.
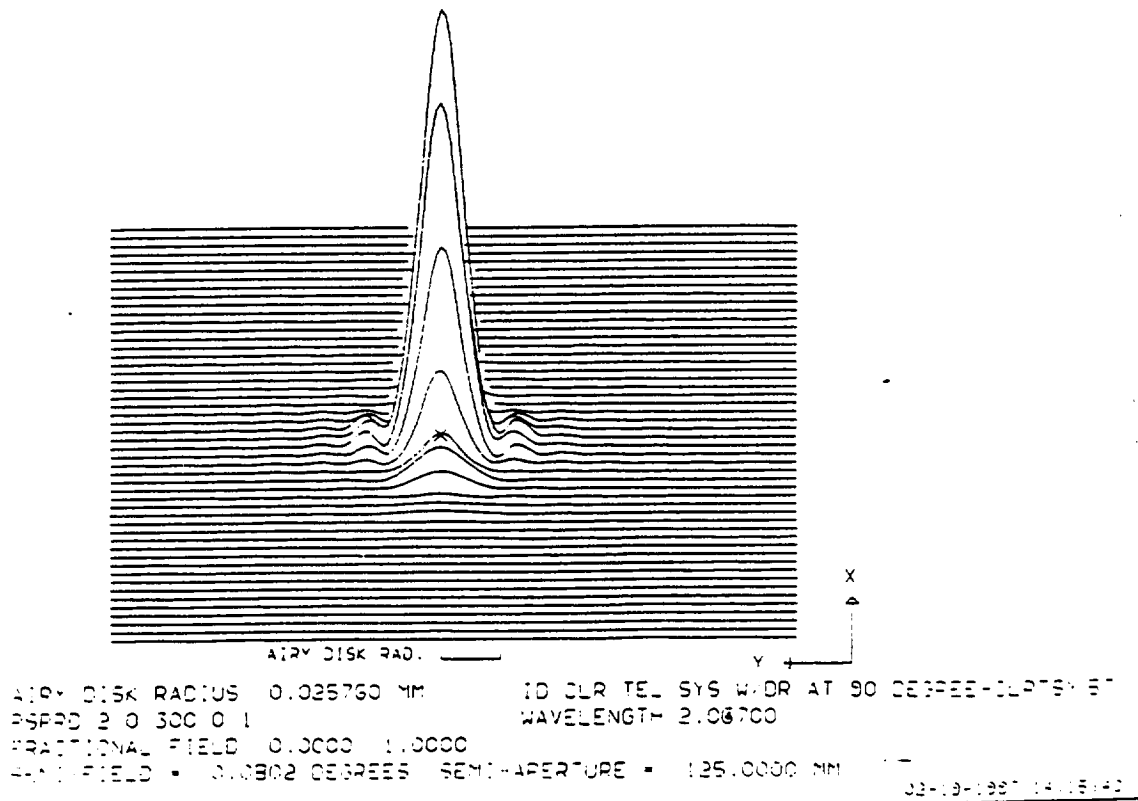

Figure 17. ZYGO measurement of the telescope primary mirror.

2.5.1 Testing of Gold-Plated Mirrors

The coherent lidar system requirements demand that the primary and secondary mirrors of the telescope to have a very high reflectivity. This is necessary for minimizing the signal loss and introducing a very low phase shift between the polarizing states. The gold plating over post-polished Nickel plated mirrors has been selected for serving this purpose.

The gold plating on primary and secondary mirrors of the coherent lidar telescope was performed by Epner Technology Incorporated, Brooklyn, New York. The thickness of plating is about 1- 2 μm. This plating has good quality of adhesion and hardness. It dose not require adhesive layer and protective layer like regular vacuum gold coating. The gold plated mirrors can be cleaned by soft cloth and tissue with alcohol or acetone, and has a reflectivity coefficient similar to that of pure gold.

A small sample of post-polished Nickel plated mirror was plated together with telescope's mirrors. And the sample was tested by the Automatic Ellipsometer of CAO. The index of refraction of the gold plated sample was measured on the ellipsometer with a HeNe source at 633nm wavelength. The index of refraction of pure gold at the same wavelength was obtained from CRC Physics-Chemistry Handbook for comparison. The reflectivity and phase of each polarization state for both cases were calculated using Fresnel coefficients formulation and plotted in MathCad software as shown the following pages. Although the indices of refarction from measurement and CRC handbook are somewhat different, the plots are showing almost no difference on the reflectivity and phase shift. Since a source at 2 microns wavelength is not available for the ellipsometer, the index of refraction for the actual lidar operating wavelength can only be obtained from the CRC handbook. The calculated results and plots are also provided. Since, the reflectivity and phase shift properties improve for the longer wavelengths, these results presented here can readily be used to for predicting the performance of the telescope and analyzing the overall lidar performance.

$$\lambda = 0.63 \cdot 10^{-6} \qquad nc = 0.202 - 3.389i$$

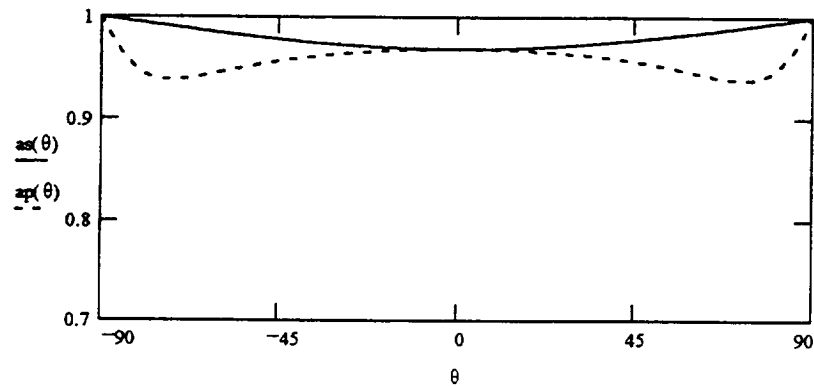$$c = 3 \cdot 10^8 \qquad \omega = \frac{2 \cdot \pi \cdot c}{\lambda} \qquad \omega = 2.992 \cdot 10^{15}$$

$$\theta = -90, -89 .. 90$$

$$\beta(\theta) = \frac{\omega}{c} \cdot \sin(\theta \cdot deg)$$

$$K1x(\theta) = \sqrt{\left[\left(\frac{\omega}{c}\right)^2 - \beta(\theta)^2\right]} \qquad K2x(\theta) = \sqrt{\left[\left(\frac{\omega}{c}\right)^2 \cdot nc^2 - \beta(\theta)^2\right]}$$

$$rs(\theta) = \frac{K1x(\theta) - K2x(\theta)}{K1x(\theta) + K2x(\theta)} \qquad rp(\theta) = \frac{K2x(\theta) - nc^2 \cdot K1x(\theta)}{K2x(\theta) + nc^2 \cdot K1x(\theta)}$$

$$as(\theta) = |rs(\theta)| \qquad ap(\theta) = |rp(\theta)|$$

$$\Phi s(\theta) = \arg(rs(\theta)) \quad \Phi sdeg(\theta) = \frac{180}{\pi} \cdot \Phi s(\theta) \qquad \Phi p(\theta) = \arg(rp(\theta)) \quad \Phi pdeg(\theta) = \frac{180}{\pi} \cdot \Phi p(\theta)$$

$$Rs(\theta) = as(\theta)^2 \qquad Rp(\theta) = ap(\theta)^2$$

$$Rp(0) = 0.938 \qquad Rp(50) = 0.908$$
$$Rs(0) = 0.938 \qquad Rs(50) = 0.96$$

$$\frac{Rs(\theta)}{Rp(\theta)}$$

(graph: vertical axis from 0.6 to 1, horizontal axis θ from −90 to 90)

$$\delta(\theta) = \Phi sdeg(\theta) - \Phi pdeg(\theta)$$

$$\delta(50) = 29.362 \qquad \delta(40) = 17.719 \qquad \delta(35) = 13.286$$
$$\delta(30) = 9.602 \qquad \delta(20) = 4.172 \qquad \delta(10) = 1.03$$

$$\frac{\delta(\theta)}{}$$

(graph: vertical axis 0 to 180, horizontal axis θ from −90 to 90)
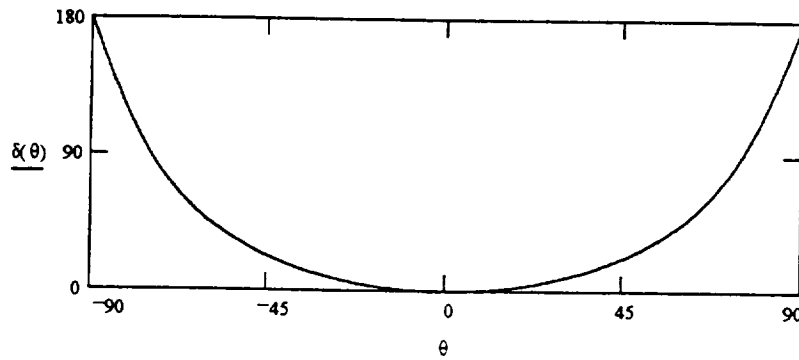
$$D(\theta) = \frac{|Rs(\theta) - Rp(\theta)|}{Rs(\theta) + Rp(\theta)}$$

$$D(50) = 0.028 \qquad D(40) = 0.018 \qquad D(30) = 0.01$$

$$D(20) = 0.004 \qquad D(10) = 0.001 \qquad D(5) = 2.67 \cdot 10^{-4}$$

$$\frac{D(\theta)}{}$$

(graph: vertical axis 0 to 0.06, horizontal axis θ from −90 to 90)
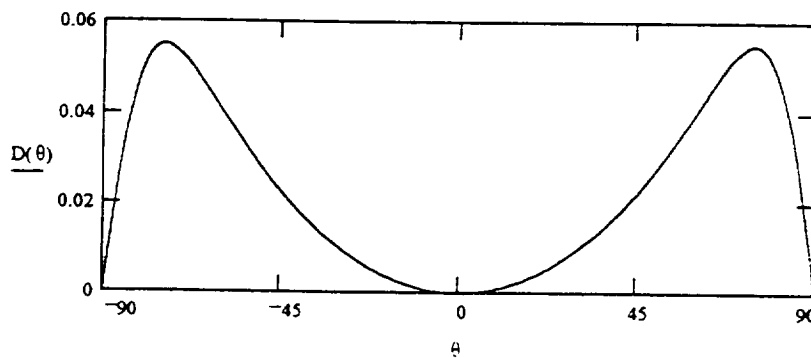
$\lambda = 0.62 \cdot 10^{-6}$ $nc = 0.13 - 3.16i$

$c = 3 \cdot 10^{8}$ $\omega = \dfrac{2 \cdot \pi \cdot c}{\lambda}$ $\omega = 3.04 \cdot 10^{15}$

$\theta = -90, -89 .. 90$

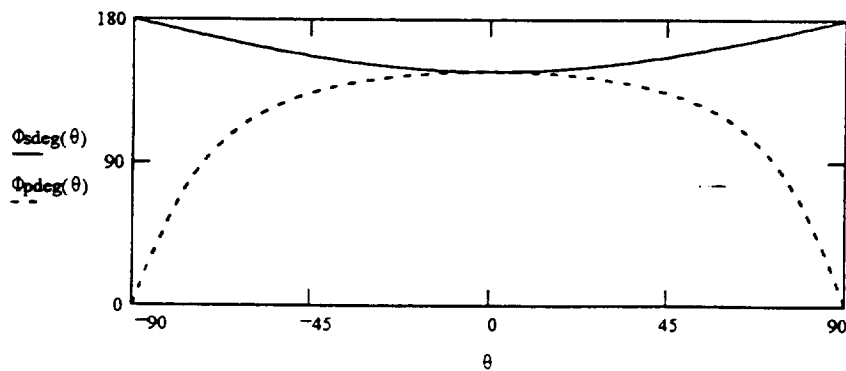$\beta(\theta) = \dfrac{\omega}{c} \cdot \sin(\theta \cdot \deg)$

$K1x(\theta) = \sqrt{\left[\left(\dfrac{\omega}{c} \right)^2 - \beta(\theta)^2 \right]}$ $K2x(\theta) = \sqrt{\left[\left(\dfrac{\omega}{c} \right)^2 \cdot nc^2 - \beta(\theta)^2 \right]}$

$rs(\theta) = \dfrac{K1x(\theta) - K2x(\theta)}{K1x(\theta) + K2x(\theta)}$ $rp(\theta) = \dfrac{K2x(\theta) - nc^2 \cdot K1x(\theta)}{K2x(\theta) + nc^2 \cdot K1x(\theta)}$

$as(\theta) = |rs(\theta)|$ $ap(\theta) = |rp(\theta)|$

$\Phi s(\theta) = \arg(rs(\theta))$ $\Phi sdeg(\theta) = \dfrac{180}{\pi} \cdot \Phi s(\theta)$ $\Phi p(\theta) = \arg(rp(\theta))$ $\Phi pdeg(\theta) = \dfrac{180}{\pi} \cdot \Phi p(\theta)$
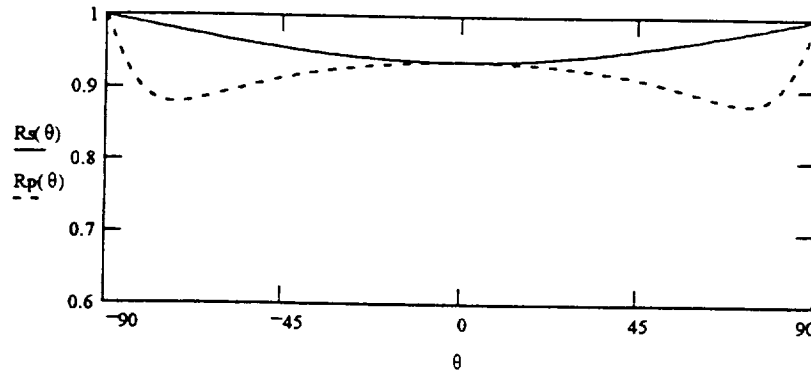
$$Rs(\theta) = as(\theta)^2 \qquad Rp(\theta) = ap(\theta)^2$$

Rp(0) = 0.954	Rp(50) = 0.932
Rs(0) = 0.954	Rs(50) = 0.971

$$\delta(\theta) := \Phi sdeg(\theta) - \Phi pdeg(\theta)$$

δ(50) = 31.326	δ(40) = 18.963	δ(35) = 14.234
δ(30) = 10.296	δ(20) = 4.478	δ(10) = 1.107

$$D(\theta) = \frac{|Rs(\theta) - Rp(\theta)|}{Rs(\theta) + Rp(\theta)}$$

D(50) = 0.02	D(40) = 0.013	D(30) = 0.007
D(20) = 0.003	D(10) = $7.922 \cdot 10^{-4}$	D(5) = $1.98 \cdot 10^{-4}$

$\lambda := 2.0 \cdot 10^{-6}$ $nc := 0.546 - 13.9i$

$c := 3 \cdot 10^{8}$ $\omega := \dfrac{2 \cdot \pi \cdot c}{\lambda}$ $\omega = 9.425 \cdot 10^{14}$

$\theta := -90, -89 .. 90$

$\beta(\theta) := \dfrac{\omega}{c} \cdot \sin(\theta \cdot deg)$

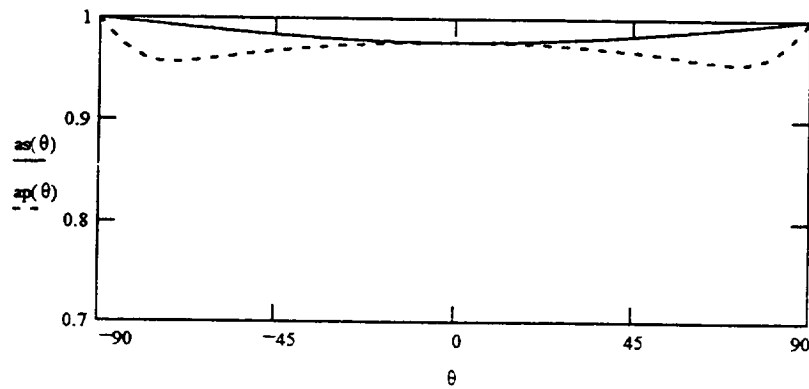$$K1x(\theta) := \sqrt{\left[\left(\dfrac{\omega}{c}\right)^2 - \beta(\theta)^2\right]} \qquad K2x(\theta) := \sqrt{\left[\left(\dfrac{\omega}{c}\right)^2 \cdot nc^2 - \beta(\theta)^2\right]}$$

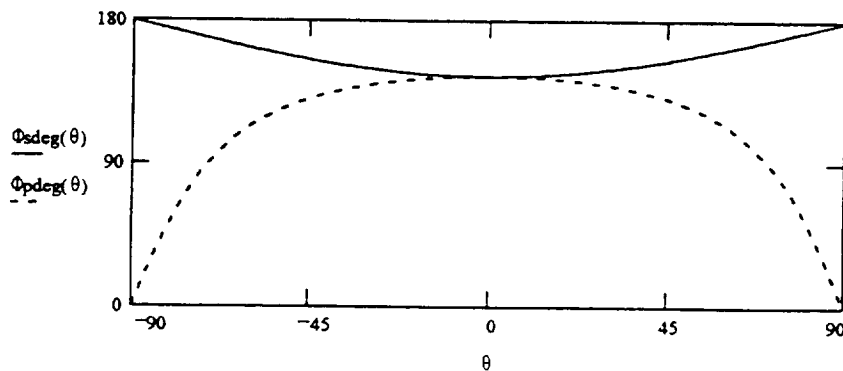$$rs(\theta) := \dfrac{K1x(\theta) - K2x(\theta)}{K1x(\theta) + K2x(\theta)} \qquad rp(\theta) := \dfrac{K2x(\theta) - nc^2 \cdot K1x(\theta)}{K2x(\theta) + nc^2 \cdot K1x(\theta)}$$

$as(\theta) := |rs(\theta)| \qquad\qquad ap(\theta) := |rp(\theta)|$
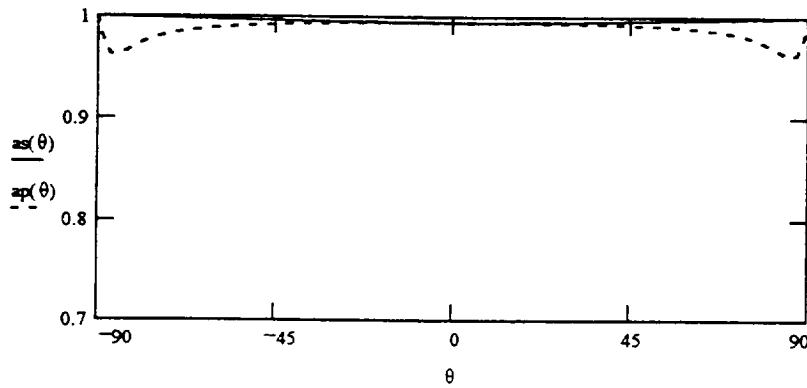
$\Phi s(\theta) := arg(rs(\theta)) \quad \Phi sdeg(\theta) := \dfrac{180}{\pi} \cdot \Phi s(\theta) \qquad \Phi p(\theta) := arg(rp(\theta)) \quad \Phi pdeg(\theta) := \dfrac{180}{\pi} \cdot \Phi p(\theta)$
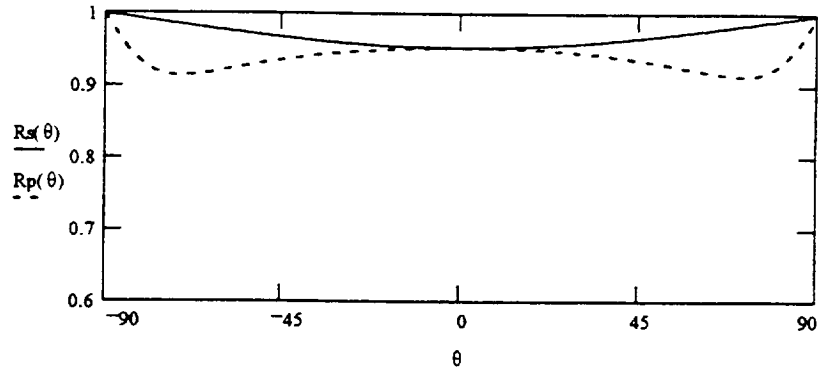
$$Rs(\theta) = as(\theta)^2 \qquad Rp(\theta) = ap(\theta)^2$$
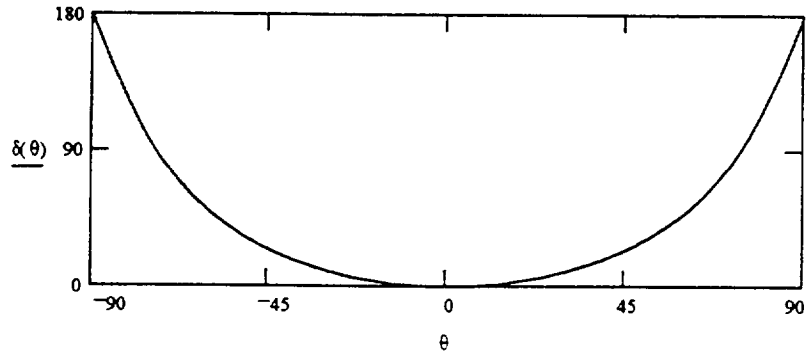
$$Rp(0) = 0.989 \qquad Rp(50) = 0.983$$
$$Rs(0) = 0.989 \qquad Rs(50) = 0.993$$
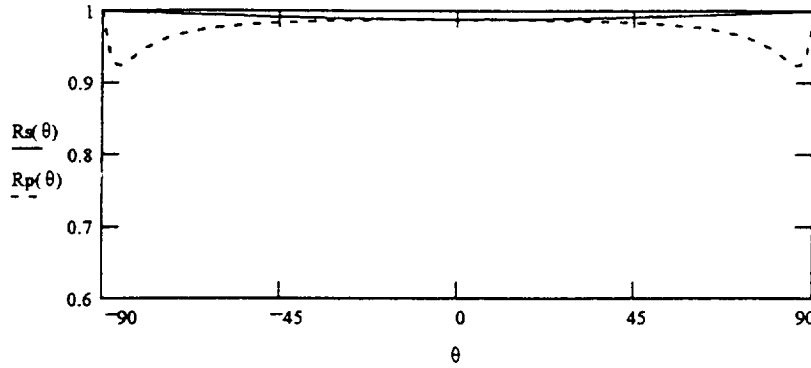
$$\delta(\theta) = \Phi sdeg(\theta) - \Phi pdeg(\theta)$$

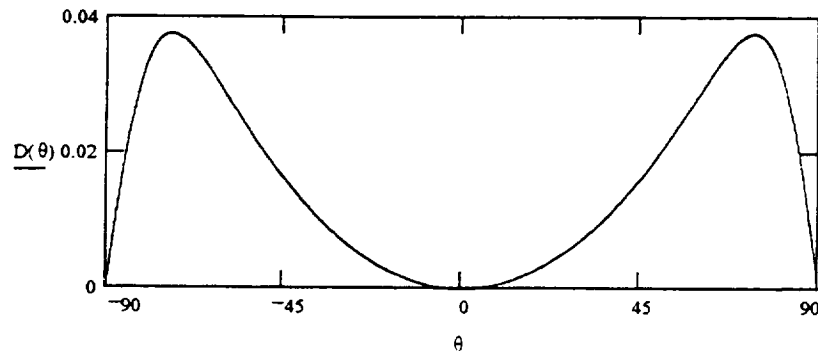$$\delta(50) = 7.493 \qquad \delta(40) = 4.433 \qquad \delta(35) = 3.302$$
$$\delta(30) = 2.374 \qquad \delta(20) = 1.024 \qquad \delta(10) = 0.252$$
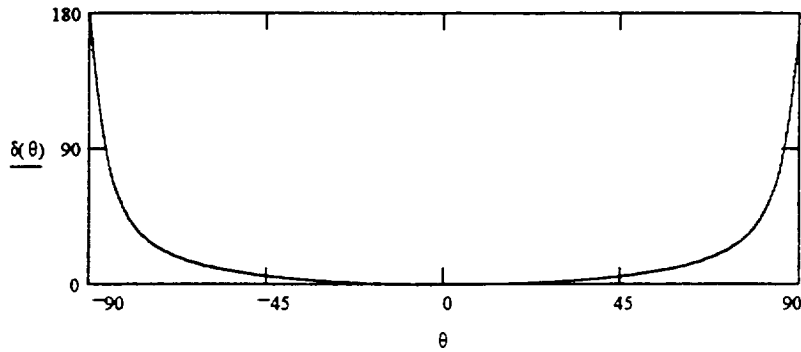
$$D(\theta) = \frac{|Rs(\theta) - Rp(\theta)|}{Rs(\theta) + Rp(\theta)}$$

$$D(50) = 0.005 \qquad D(40) = 0.003 \qquad D(30) = 0.002$$

$$D(20) = 7.018 \cdot 10^{-4} \qquad D(10) = 1.727 \cdot 10^{-4} \qquad D(5) = 4.303 \cdot 10^{-5}$$
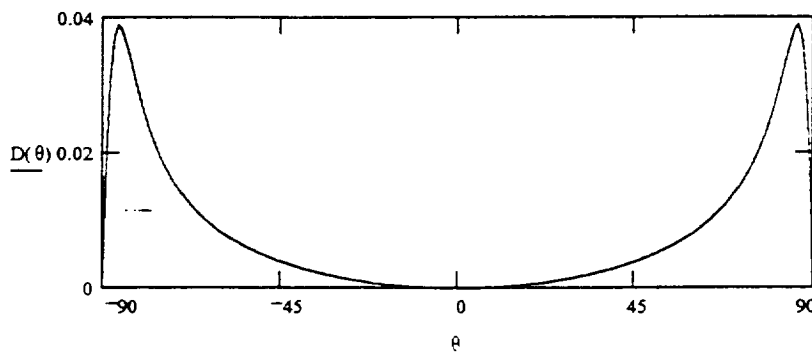
3.0   Breadboard/Testbed Lidar System

A solid state pulsed coherent lidar system capable of measuring atmospheric winds using the existing NASA/MSFC 100 mJ, Tm:YAG, single frequency laser was designed and its performance analyzed under this delivery order. As part of this effort, a number of trade-off analyses were performed and various design options were evaluated. This system was to be designed in such a way that it would allow for the development of a rugged and reliable lidar system with sufficient flexibility for incorporating other laser systems such as those under development at Langley Research Center, Jet Propulsion Laboratory and Coherent Technologies, Inc. for NASA/MSFC. Although the lidar system is intended for wind measurements from ground-based stations, its design must consider the major aircraft and space operational requirements such as signal detection over wide bandwidth and long pulse round trip times.

The system design is illustrated in Figure 1. The transmitter laser uses a part of the output beam of a low power, continuous wave (CW) laser (seed or injection oscillator) to generate stable, single frequency pulses. The transmitter laser pulses are then expanded by an off-axis, afocal telescope before being deflected by 30 degrees by an optical element. If the desired scan pattern is continuous conical, then the scanner optical element is continuously rotated by a precision motor to provide a conical pattern in the atmosphere. The remaining part of the seed laser output beam is used for frequency locking of a programmable, frequency-agile CW local oscillator (LO) laser. The output of this laser is directed to the optical detector to be mixed with the signal beam. In order to compensate for the large Doppler shift due to the spacecraft motion and minimize the required bandwidth of the detector and receiver, the frequency of the LO laser is varied about the seed laser frequency with the azimuth angle of the conical scan. The lidar optical train includes a small rotating wedge (derotator) and a steering mirror (beam misalignment compensator or BMC). The derotator rotation is synchronized with the scanner to compensate for the signal beam misalignment due to the scanner continuous motion during the pulse round trip time. The derotator is not required if a a step-stare scan pattern is utilized. The BMC, through an active control system, corrects for the misalignments due the scanner motion during the pulse reception time and the change in the spacecraft inertial nadir pointing angle during the pulse round trip time. After passing through the derotator and BMC, the returned photons are launched into a fiber to be combined in a fiber coupler with the local oscillator beam. The output of the fiber optic coupler is focused onto a high-quantum efficiency, wideband detector optimized for heterodyne detection.

Based on this optical analysis and the previously developed telescope design , the lidar optical layout was specified defining all the optical components and their relative positions. A detailed optical design analysis was performed that is described in chapter 2 of this report. This analysis provided the optical fabrication and alignment tolerances for each optical components, and defined their performance parameters. The fabrication drawings for the costume-made optical components were produced and the off-the-shelf compnents were specified.

Based on the lidar optical layout design and the system optical requirements, a mechanical design and analysis was performed that resulted in a complete lidar structure design and the designs of various lidar optical mounts and positioning elements.

Transmitter Laser

PZT Driver

Injection Locking Loop

Detector

Pulsed Laser

BS

Mirror

Seed Laser

MM Optics

Isolator

Laser Freq. Controller

Freq. Monitor

Frequency Locking FB Control

Det.

BS

LO Laser

Frequency-Agile LO Laser

BS

Beam Misalignment Compensator

De-Rotator

λ/4

Lens

Control Signal

Control Signal

Polarizing BS

Scanner

Optical Fiber

Coupler

Lens

Telescope

Lidar Detector/ Pre-Amplifier

Laser Controller

ScanController

IF Receiver

A/D

Computation & Control System

Data Recorder

Control Signal

Scan Controller

Scanner Motor

Platform Inertial/GPS Data

Data Transmitter

Figure 1. Solid State Coherent Doppler Lidar System Diagram.

The mechanical design analysis effort included investigation and study of various design options for mounting and packaging different subsystems and components of the lidar breadboard and support structure. Some of the major subsystems and components include the wedge scanner, telescope, routing mirrors, polarizing beam splitter, lasers and detectors. Attempts were made to mount these components in a stress-free and stable manner. It was also intended to provide a design that is highly flexible and allow easy accessibility to all the optical components. Figure 2 shows the lidar support structure, and figures 3-5 illustrate the integrated support structure and the lidar subsystems. Figure 6 shows the lidar system with the NASA/MSFC 100 mJ laser at the bottom, the scanner motor/encoder at the top, and the optical subsystem in the middle of the structure. The optical subsystem includes the telescope, lag angle compensator, the transmitt/ receive optical train, and the signal detector/amplifier.

SUPPORT STRUCTURE
BREADBOARD LIDAR SYSTEM
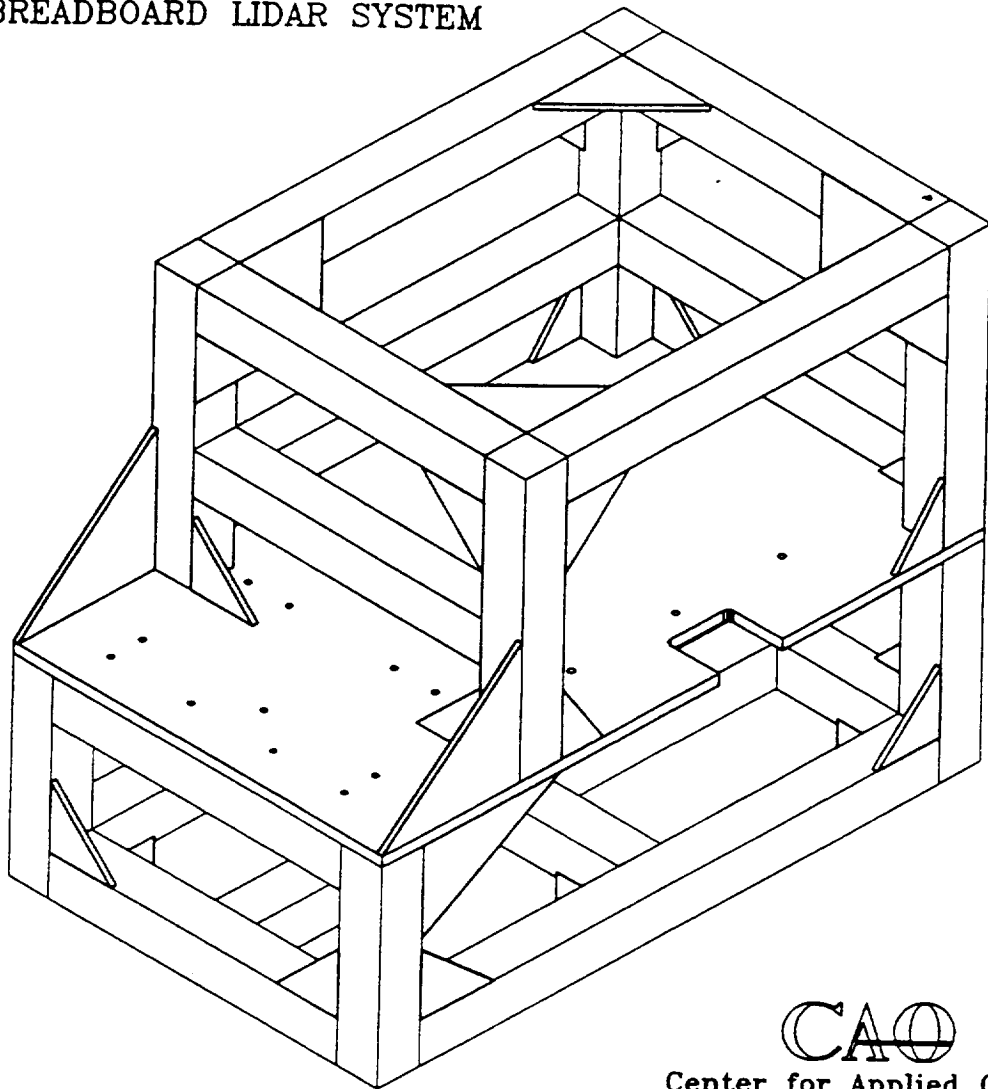
Center for Applied Optics

Figure 2. Support Structure for the breadboard lidar system.

SIDE VIEW
BREADBOARD LIDAR SYSTEM
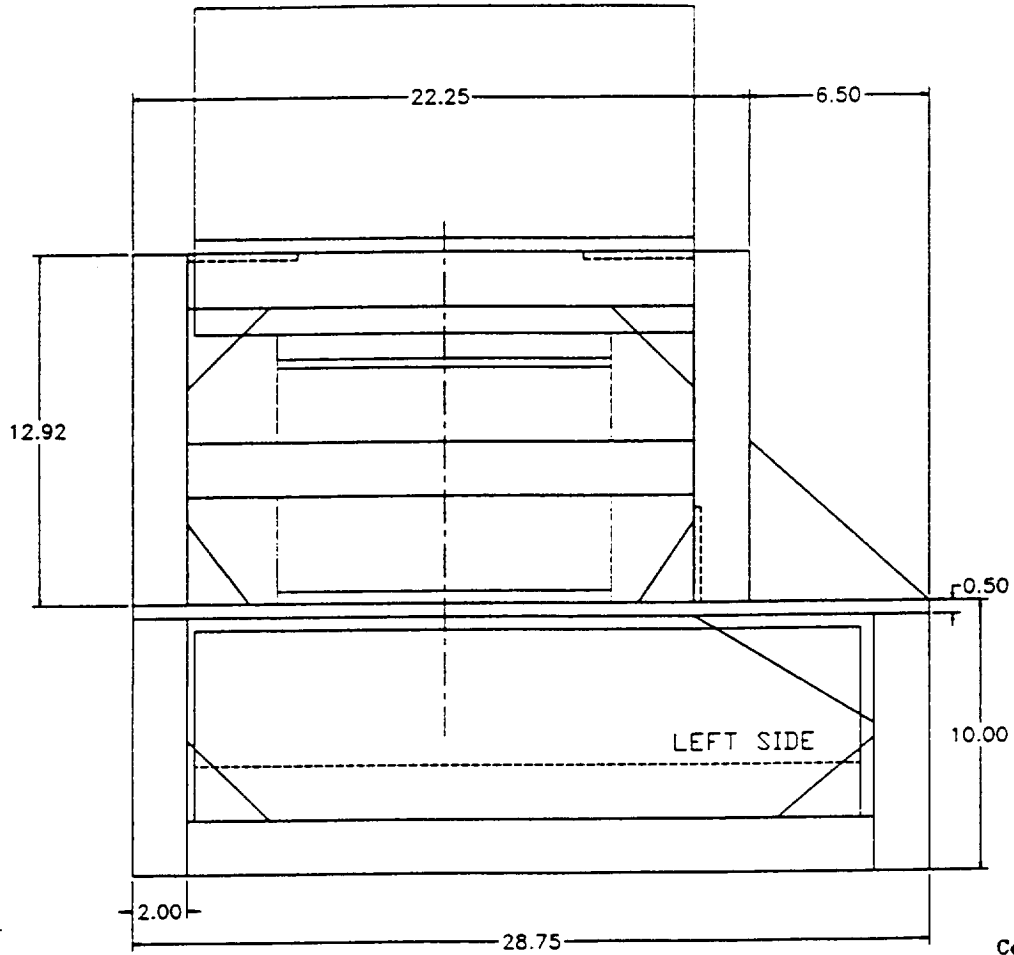
Figure 3. Breadboard lidar system side view.

FRONT VIEW
BREADBOARD LIDAR SYSTEM

SCANNER
ENVELOPE
(18" X 18" X 12")

SUPPORT
STRUCTURE
(2" SQ. TUBES)

TELESCOPE
(14.75" X 12" X 9")

22.92

18.00

CAO
Center for Applied Optics
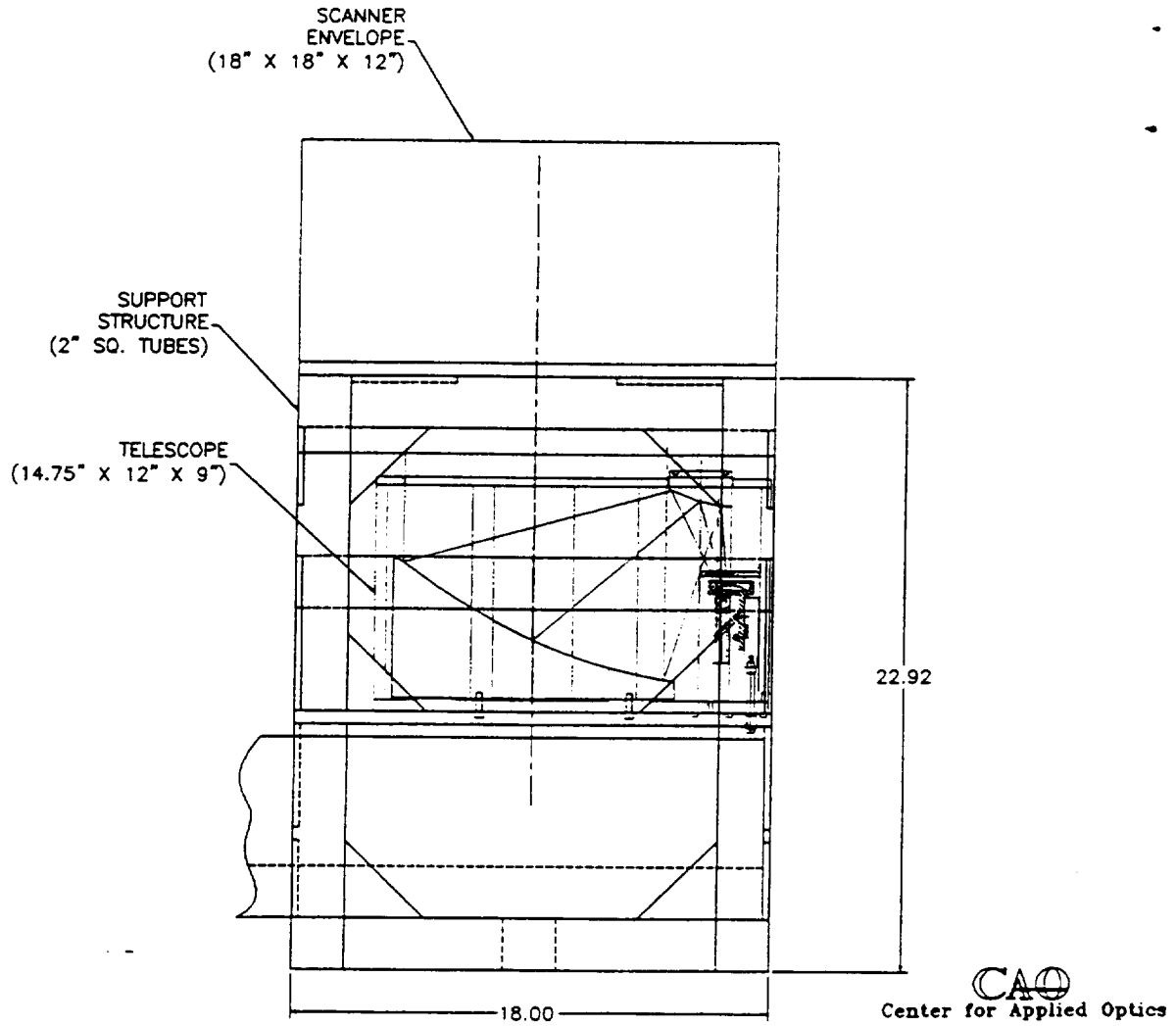
Figure 4. Breadboard lidar system front view.
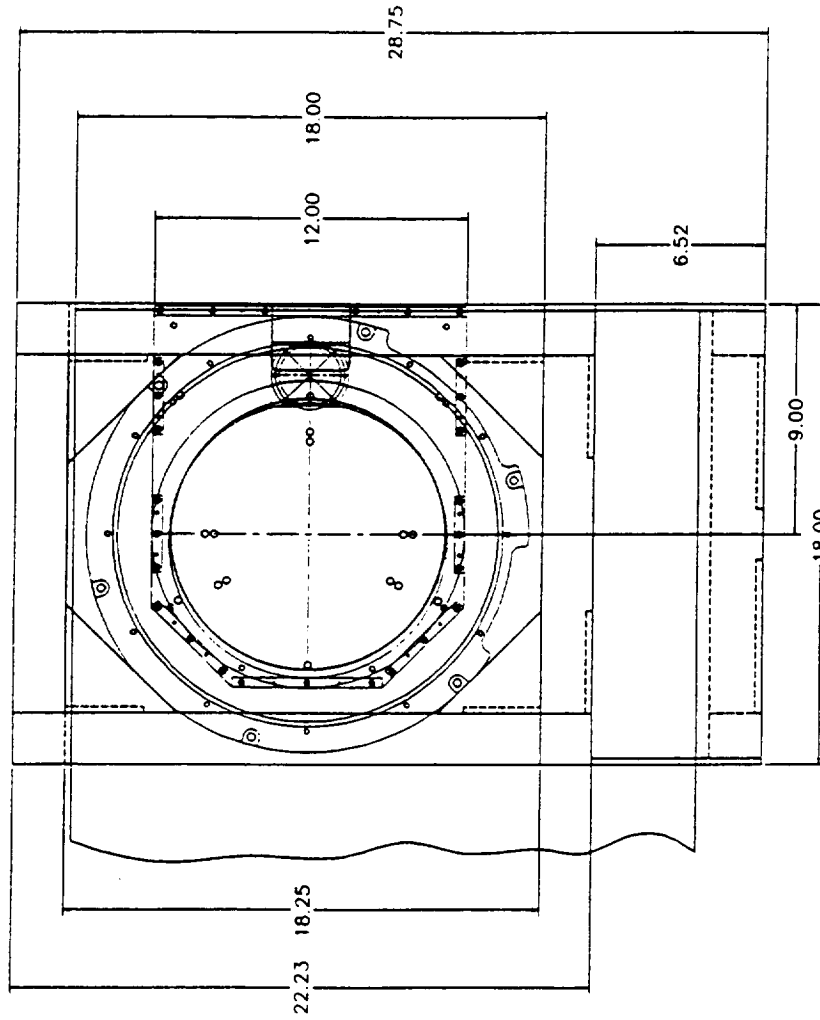
Figure 5. Breadboard lidar system top view.
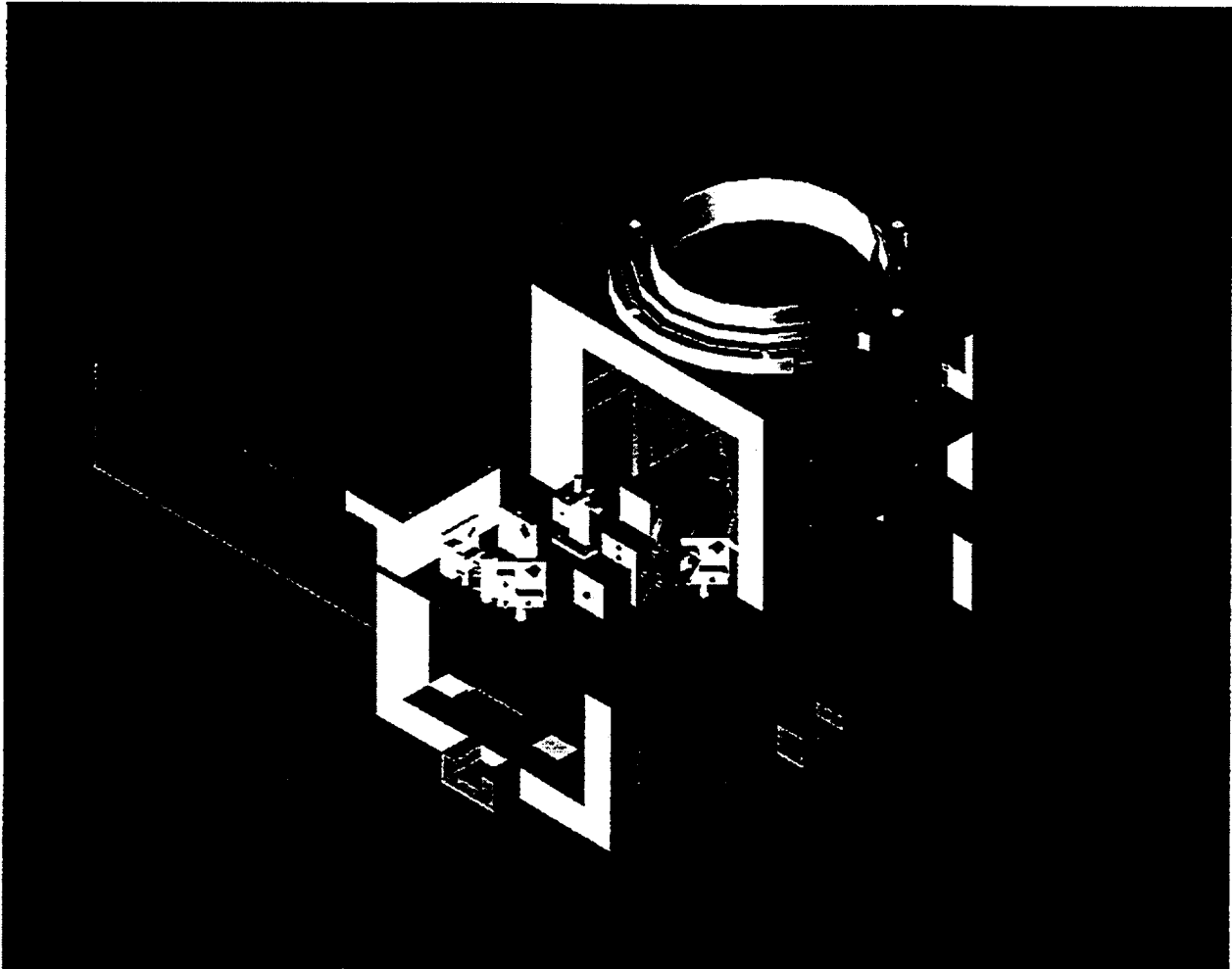
Figure 6. Breadboard Lidar System.

The lidar structure includes a small optical plate for mounting all the lidar receiver optical elements including the signal and local oscillator beams routing and focusing elements, and the lidar signal detector. The structure has been designed such that the transmitter/receiver telescope, the transmitter laser, and the receiver optics will maintain a high degree of alignment with respect with each other stability over a wide range of operational environments. A large number of detailed mechanical drawings was submitted to MSFC over the performance period of this DO, describing all the details of the lidar mechanical designs. Figure 7 shows the actual telescope developed by UAH for this system. The results of the telescope measurements are summarized in chapter 2. The telescope design is based on a novel off-axis catadioptric design with a magnification of 25 and aperture size of 25 cm. Figure 8 shows the actual wedge scanner element that was specified by the UAH personnel and acquired by NASA/MSFC. The wedge material is Silicon and has a 28 cm clear aperture.
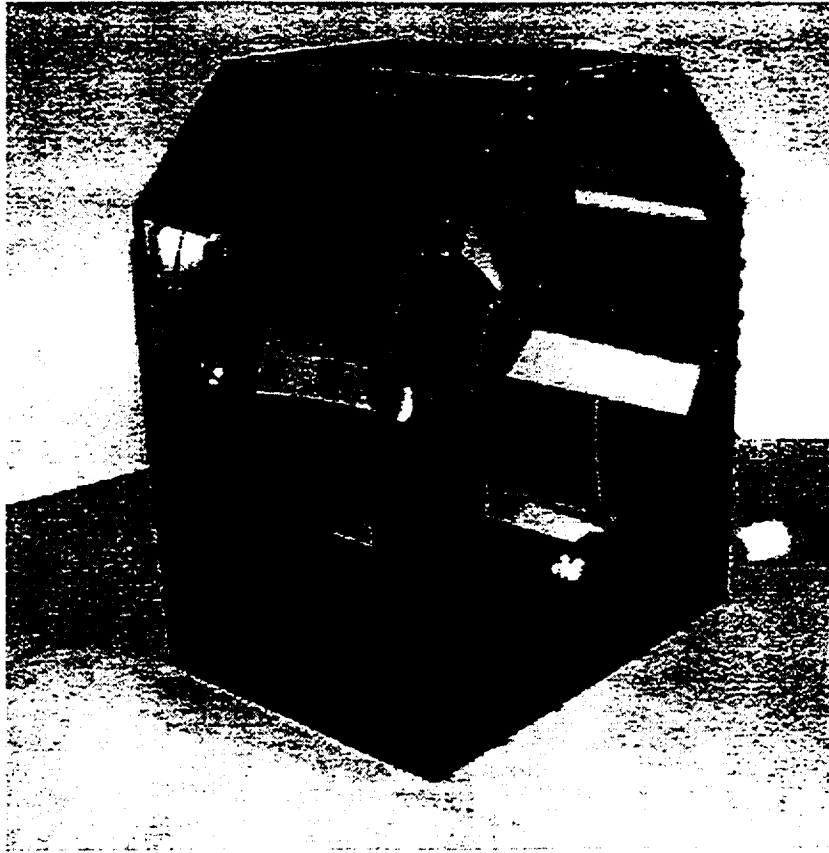
Figure 7. Compact Lidar Telescope.
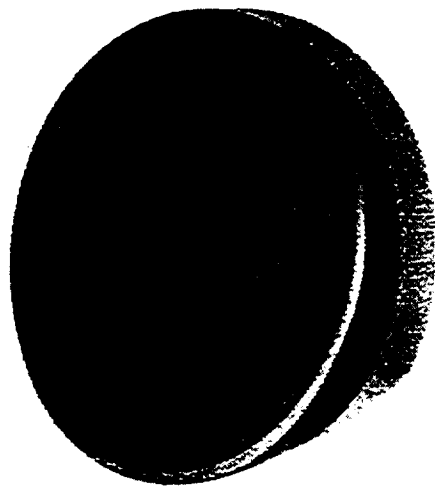
Figure 8. 28 cm Silicon Wedge Scanner Element.

The lidar system optical layout and mechanical design was later modified to a much more compact and lower mass design based on the accommodation requirements of the Space Shuttle Hitchhiker canisters. The lidar modification became necessary when the NASA/MSFC scientists envisioned an opportunity for deployment of a similar system in space onboard a Space Shuttle and in two or three Hitchhiker canisters. Therefore, the UAH personnel modified the lidar breadboard design to be developed as a testbed for a Hitchhiker mission. The trade-off of this design change was less flexibilty and accessibility to the optical components. Figure 9 is a complete lidar testbed drawing showing all the lidar subsystems and major components.
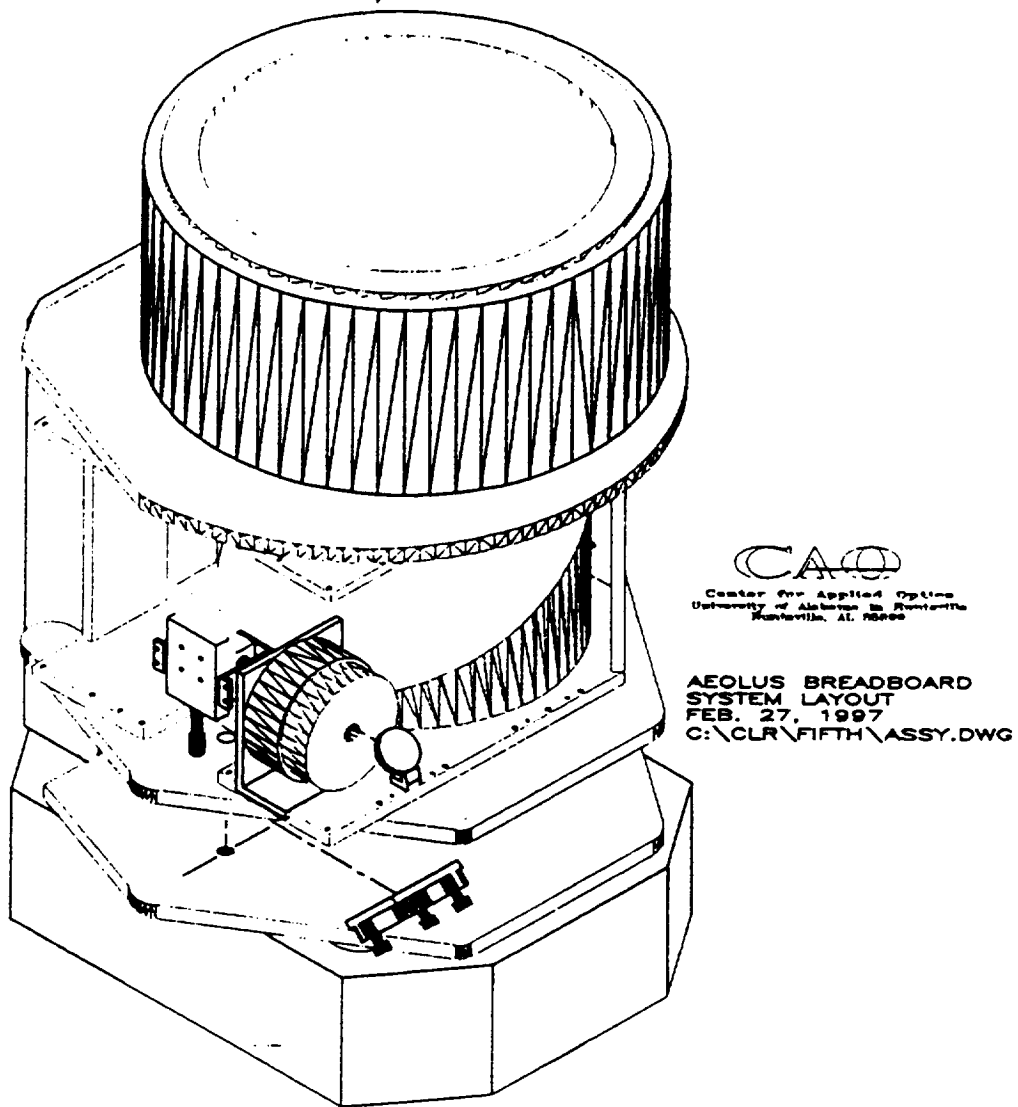
Figure 9. Lidar system testbed design.

Figures 10 and 11 show the side views of the lidar system and the actual dimensions of various lidar components. Meeting the mass and volume constraints of the Hitchhiker are very challenging, and require careful mechanical and thermal design analyses. The design provide a relatively advanced design concept for the development of the actual flight instrument. For the actual Hitchhiker mission, the lidar transmitter/receiver assembly will be placed in one canister and all the electronics including the signal processor will be placed in another canister.
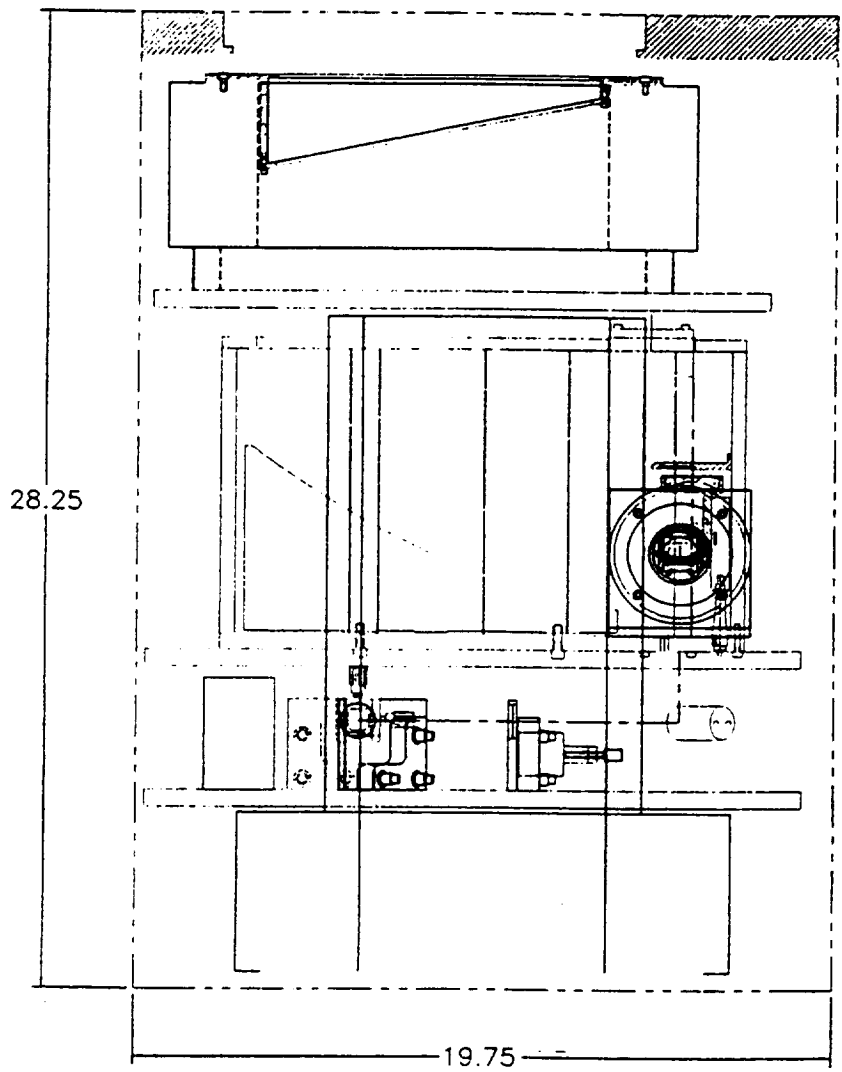
CAO

Center for Applied Optics
University of Alabama in Huntsville
Huntsville, Al, 35899

AEOLUS BREADBOARD
SYSTEM LAYOUT
FEB. 27, 1997
C:\CLR\FIFTH\LAYOUT10.DWG

Figure 10. Lidar system testbed side view.

4.0 DETECTOR CHARACTERIZATION

4.1 INTRODUCTION

A number of semiconductor detectors, operating at 2 micron wavelength region, were characterized and their heterodyne detection properties were analyzed. The detector measurements were performed using the Detector Characterization Facility (DCF) that had previously been developed by the UAH personnel at NASA/MSFC. A detail description of the DCF design and capabilities was provided in the NASA report NAS8-38609/DO77, and the DFC principles of measurements, calibration and data analysis procedures were reported in the NASA report NAS8-38609/DO 118. Figure 1 shows the Detector Characterization Facility at NASA/ MSFC. The DCF is capable of providing all the necessary detection parameters for design, development and calibration of coherent and incoherent solid state laser radar (lidar) systems. The coherent lidars in particular require an accurate knowledge of detector heterodyne quantum efficiency, nonlinearity properties and voltage-current relationship as a function of applied optical power. At present no detector manufacturer provides these quantities or adequately characterizes their detectors for heterodyne detection operation. In addition, the detector characterization facility measures the detectors DC and AC quantum efficiencies noise equivalent power and frequency response up to several GHz. The DCF is also capable of evaluating various heterodyne detection schemes such as balanced detectors and fiber optic interferometers. It should also be noted that the DCF design was further improved to allow for characterization of diffractive and holographic optical elements and other critical optical components of coherent lidar systems.

Figure 1. Detector Characterization Facility.

4.2 CHARACTERIZATION OF A 2-MICRON InGaAs DETECTOR

A number of 75 and 100 microns diameter InGaAs detector with a cutoff wavelength of 2.5 and 2.2 microns, acquired from Sensors Unlimited and Epitaxx were fully characterized in the NASA/MSFC Detector Characterization Facility. The following data are the results of the measurements performed on a Epitaxx detector identified by model number: 100GR2.2T and serial number: 9515E3130. This detector is not suitable for a space-based lidar due to its limited bandwidth, however it can be used for ground-based and some airborne applications that do not require signal detection over a wide bandwidth. As can be seen from the measrement results summerized in this report, this type of detectors is best suited for direct detection applications which require low dark current.

RESPONSIVITY AND LINEARITY MEASUREMENTS

V_B=0.00 V

Notes:
Detector anode terminated by 50 ohms
With laser beam blocked, InAs laser power monitor detector reads 21 mV and
detector direct output is 0.0 mV.

InAs Power Monitor (mV)	Detector Output (mV)	Incident Power P_{in} (mW)	Detector current I_d (mA)
76	5.1	0.112872	0.0992
99	7.3	0.157653	0.1420
152	12	0.260844	0.2335
210	17.3	0.37377	0.3366
300	25	0.549	0.4864
323	26.6	0.593781	0.5175
402	32.6	0.747594	0.6342
504	38.7	0.946188	0.7529
602	43.1	1.136994	0.8385
727	47.1	1.380369	0.9163
802	49.2	1.526394	0.9572
935	52.1	1.785345	1.0136
1110	55.3	2.12607	1.0759
1210	56.8	2.32077	1.1051
1340	58.4	2.57388	1.1362
1420	59.2	2.72964	1.1518
1670	61.7	3.21639	1.2004
1810	62.9	3.48897	1.2237
1940	63.8	3.74208	1.2412
2010	64.3	3.87837	1.2510
2190	65.2	4.22883	1.2685
2300	65.8	4.443	1.2802

V_B=2.00 V

Notes:
Detector anode terminated by 50 ohms
With laser beam blocked, InAs laser power monitor detector reads 21 mV and detector direct output is 0.5 mV.

InAs Power Monitor (mV)	Detector Output (mV)	Incident Power P_{in} (mW)	Detector current I_d (mA)
52	4	0.066144	0.0681
96	8.5	0.151812	0.1556
158	14.3	0.272526	0.2685
214	18.8	0.381558	0.3560
310	27.1	0.56847	0.5175
409	30.7	0.761223	0.5875
500	31.1	0.9384	0.5953
603	31.3	1.138941	0.5992
709	31.4	1.345323	0.6012
836	31.5	1.592592	0.6031
901	31.6	1.719147	0.6051
1110	31.7	2.12607	0.6070
1200	31.7	2.3013	0.6070
1330	31.8	2.55441	0.6089
1420	31.8	2.72964	0.6089

$I_d=0.93P_{in}$

$I_d=1.05P_{in}(1-0.40P_{in})$

V_B=3.00 V

Notes:
Detector anode terminated by 50 ohms
With laser beam blocked, InAs laser power monitor detector reads 20 mV and detector direct output is 0.6 mV.

InAs Power Monitor (mV)	Detector Output (mV)	Incident Power P_{in} (mW)	Detector current I_d (mA)
55	4.8	0.071985	0.0817
106	10.8	0.171282	0.1984
200	20.3	0.3543	0.3833
304	29.1	0.556788	0.5545
400	35.9	0.7437	0.6868
484	43.3	0.907248	0.8307
654	45.8	1.238238	0.8794
787	46.1	1.497189	0.8852
880	46.2	1.67826	0.8872
923	46.3	1.761981	0.8891
1130	46.4	2.16501	0.8911
1220	46.5	2.34024	0.8930
1390	46.6	2.67123	0.8949
1470	46.6	2.82699	0.8949

V_B=3.50 V

Notes:

Detector anode terminated by 50 ohms

With laser beam blocked, InAs laser power monitor detector reads 20 mV and detector direct output is 0.7 mV.

InAs Power Monitor (mV)	Detector Output (mV)	Incident Power P_{in} (mW)	Detector current I_d (mA)
66	6.5	0.093402	0.1128
108	11.7	0.175176	0.2140
148	16.3	0.253056	0.3035
214	23.2	0.381558	0.4377
320	32.9	0.58794	0.6265
405	39.5	0.753435	0.7549
524	47.4	0.985128	0.9086
662	57.7	1.253814	1.1089
811	58.7	1.543917	1.1284
1010	59.1	1.93137	1.1362
1150	59.3	2.20395	1.1401
1270	59.4	2.43759	1.1420
1410	59.5	2.71017	1.1440
1600	59.6	3.0801	1.1459
1780	59.7	3.43056	1.1479
1880	59.7	3.62526	1.1479

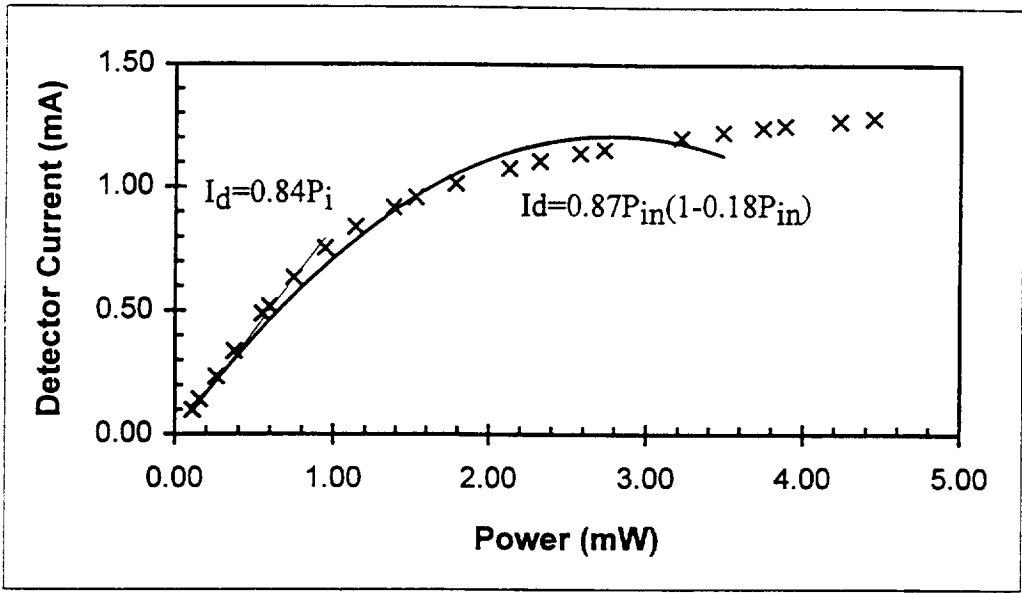## V_B=4.00 V

Notes:
Detector anode terminated by 50 ohms
With laser beam blocked, InAs laser power monitor detector reads 20 mV and detector direct output is 0.7 mV.

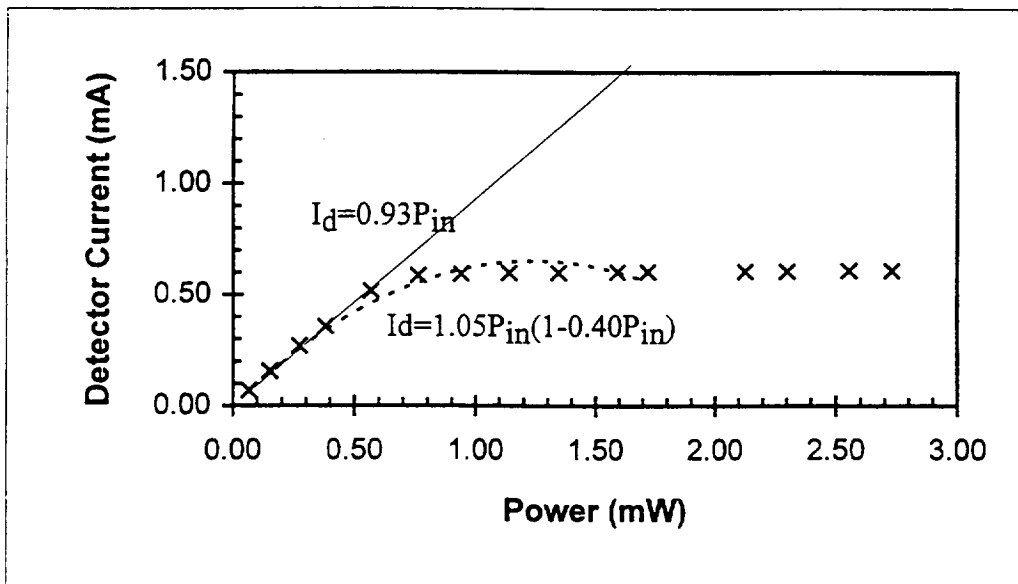| InAs Power Monitor (mV)	Detector Output (mV)	Incident Power P_{in} (mW)	Detector current I_d (mA)
96	10.7	0.151812	0.1946
200	23	0.3543	0.4339
305	34	0.558735	0.6479
402	42.8	0.747594	0.8191
515	52.3	0.967605	1.0039
614	58.9	1.160358	1.1323
715	65.3	1.357005	1.2568
838	75.8	1.596486	1.4611
951	78.8	1.816497	1.5195
1160	79.7	2.22342	1.5370
1205	79.7	2.311035	1.5370
1301	79.9	2.497947	1.5409
1429	80.1	2.747163	1.5447
1548	80.2	2.978856	1.5467
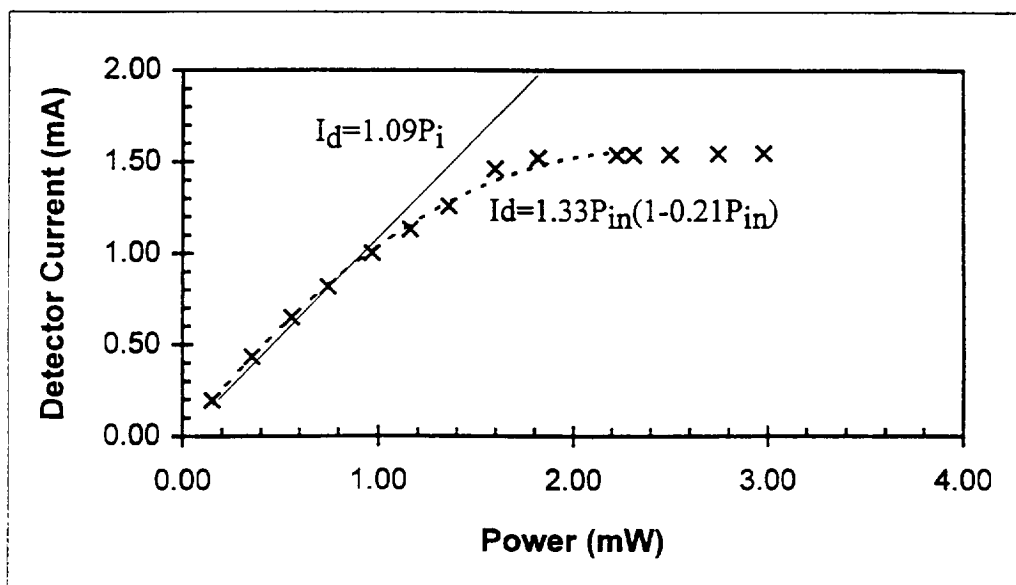
V_B=4.50 V

Notes:
Detector anode terminated by 50 ohms
With laser beam blocked, InAs laser power monitor detector reads 20 mV and
detector direct output is 0.7 mV.

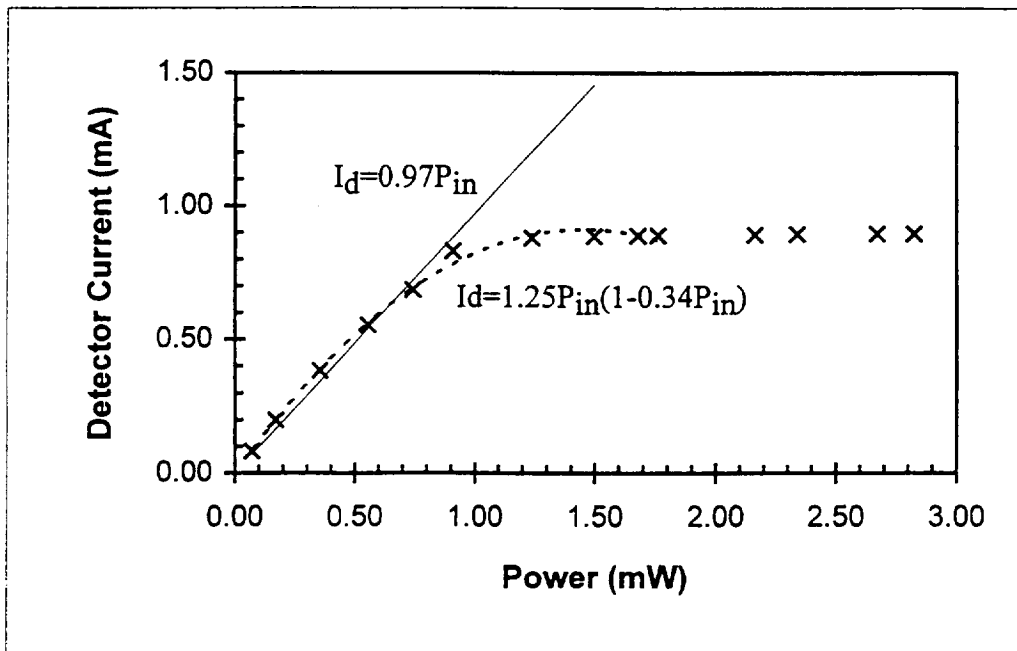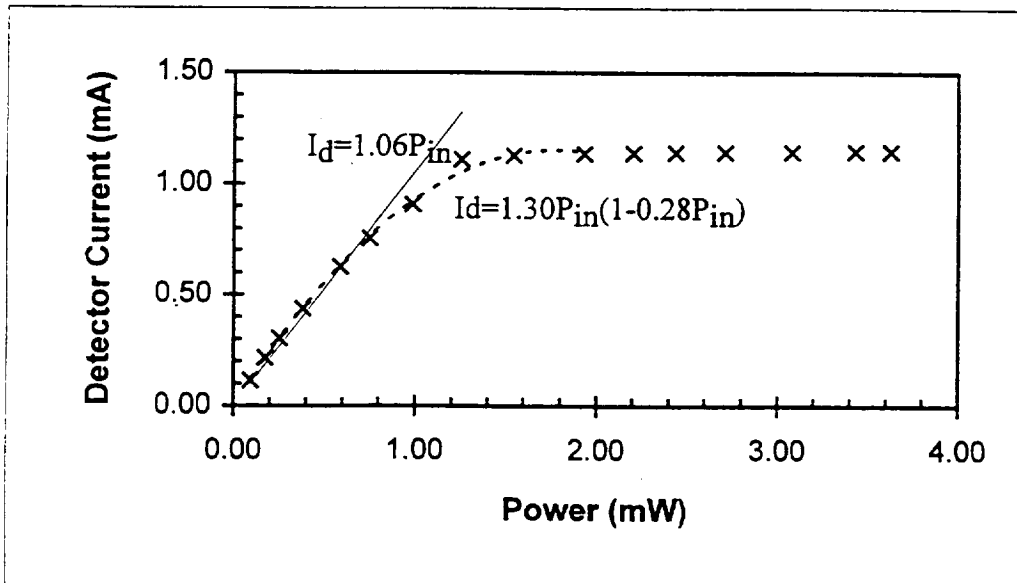| InAs Power Monitor (mV)	Detector Output (mV)	Incident Power P_{in} (mW)	Detector current I_d (mA)
40	3.5	0.04278	0.0545
93	11	0.145971	0.2004
206	25.8	0.365982	0.4883
304	37.9	0.556788	0.7237
432	51.4	0.806004	0.9864
533	61.1	1.002651	1.1751
658	71.9	1.246026	1.3852
793	82.1	1.508871	1.5837
858	86.7	1.635426	1.6732
1012	96.1	1.935264	1.8560
1090	100.7	2.08713	1.9455
1180	108.3	2.26236	2.0934
1310	118.7	2.51547	2.2957
1470	120.8	2.82699	2.3366
1690	121.7	3.25533	2.3541
1810	122	3.48897	2.3599
1890	122.2	3.64473	2.3638
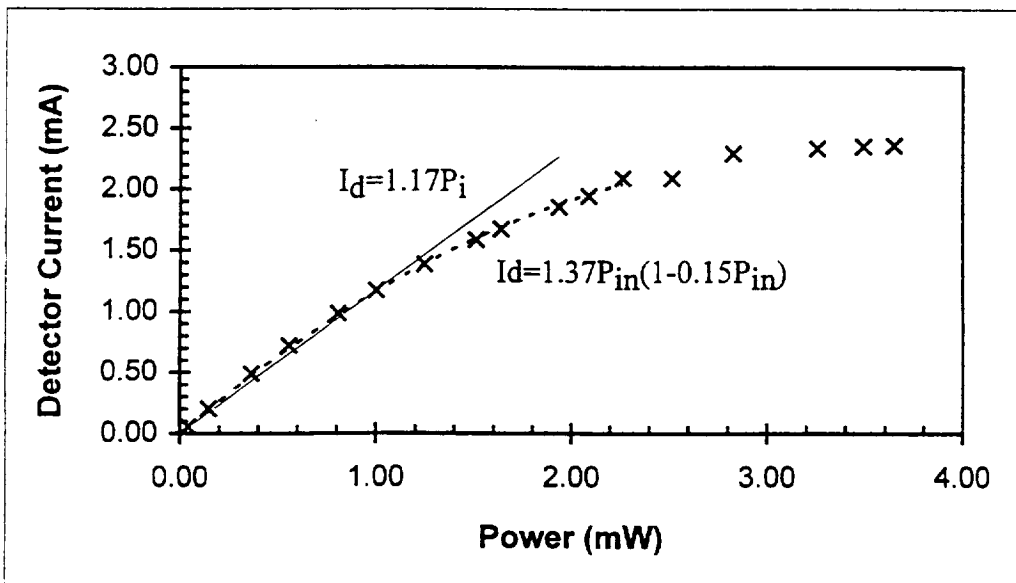
V_B=5.00 V

Notes:
Detector anode terminated by 50 ohms
With laser beam blocked, InAs laser power monitor detector reads 20 mV and detector direct output is 0.9 mV.

InAs Power Monitor (mV)	Detector Output (mV)	Incident Power P_{in} (mW)	Detector current I_d (mA)
55	5.5	0.0523	0.0895
102	11.5	0.12092	0.2062
150	17.6	0.191	0.3249
205	24.1	0.2713	0.4514
328	38.4	0.45088	0.7296
408	47.6	0.56768	0.9086
512	58.8	0.71952	1.1265
604	68.3	0.85384	1.3113
700	77.1	0.994	1.4825
810	88	1.1546	1.6946
1000	104.7	1.432	2.0195
1210	121.4	1.7386	2.3444
1450	138.6	2.089	2.6790
1700	155	2.454	2.9981
2000	172.6	2.892	3.3405
2310	186.9	3.3446	3.6187
2520	199	3.6512	3.8541
2710	213.7	3.9286	4.1401
3020	225.2	4.3812	4.3638
3270	227	4.7462	4.3988
3520	228	5.1112	4.4183

$I_d=1.44P_i$

$I_d=1.64P_{in}(1-0.10P_{in})$
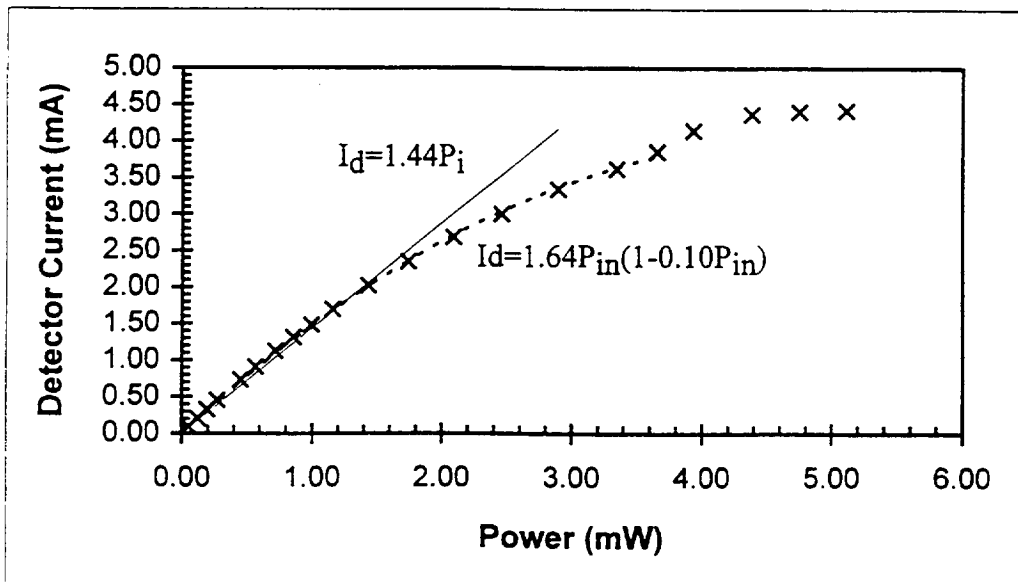
Detector Responsivity and Linearity
Summary of Results

V_B	Linear Responsivity		Non-Linear Responsivity	
(V)	ρ_0 (A/W)	η_{DC}	ρ (mA/mW)	α (1/mW)
0.00	0.84	0.5043	0.87	0.18
2.00	0.93	0.5583	1.05	0.40
3.00	0.97	0.5823	1.25	0.34
3.50	1.06	0.6364	1.30	0.28
4.00	1.09	0.6544	1.33	0.21
4.50	1.17	0.7024	1.37	0.15
5.00	1.44	0.8645	1.64	0.10
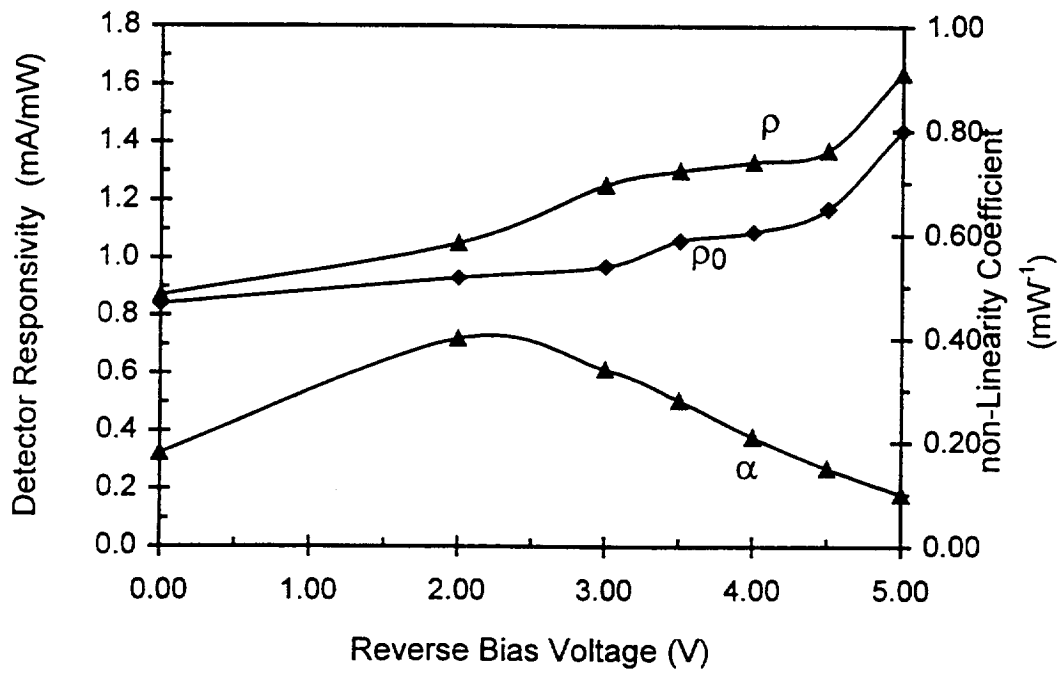
Voltage-Current Characteristics

Optical Power=0.0

Bias Current Monitor V_{Bi} (mV)	Bias Voltage Monitor V_B (mV)	Detector Voltage V_d (V)	Detector Current I_d (μA)	Detector Resistance R_d (Ω)
0.0	0.0	0.00000	0.000	
51.9	51.9	-0.05190	0.000	1588491.4
128.2	128.1	-0.12810	-0.081	2006867.4
254.3	254.2	-0.25421	-0.101	6951491.4
408.5	408.4	-0.40841	-0.121	2927443.4
549.5	549.3	-0.54931	-0.202	1332638.1
650.5	650.2	-0.65022	-0.302	417187.4
718.1	717.5	-0.71753	-0.605	191705.8
747.6	746.8	-0.74684	-0.806	96275.4
845.5	843.6	-0.84370	-1.915	50965.8
956.9	952.1	-0.95235	-4.839	19867.8
1109.8	1095.3	-1.09605	-14.617	13275.5
1138.9	1121.4	-1.12231	-17.641	6064.9
1269.4	1232.3	-1.23422	-37.399	4167.5
1401.0	1332.6	-1.33614	-68.952	2050.3
1670.7	1500.5	-1.50932	-171.573	1571.3
1727.9	1530.4	-1.54063	-199.093	984.4
1886.1	1604.9	-1.61947	-283.468	855.4
2004.0	1654.0	-1.67214	-352.823	690.1
2157.0	1711.0	-1.73411	-449.597	602.5
2256.0	1744.0	-1.77053	-516.129	465.6
2690	1868	-1.91059	-828.629	377.4
3283	1998	-2.06458	-1295.363	
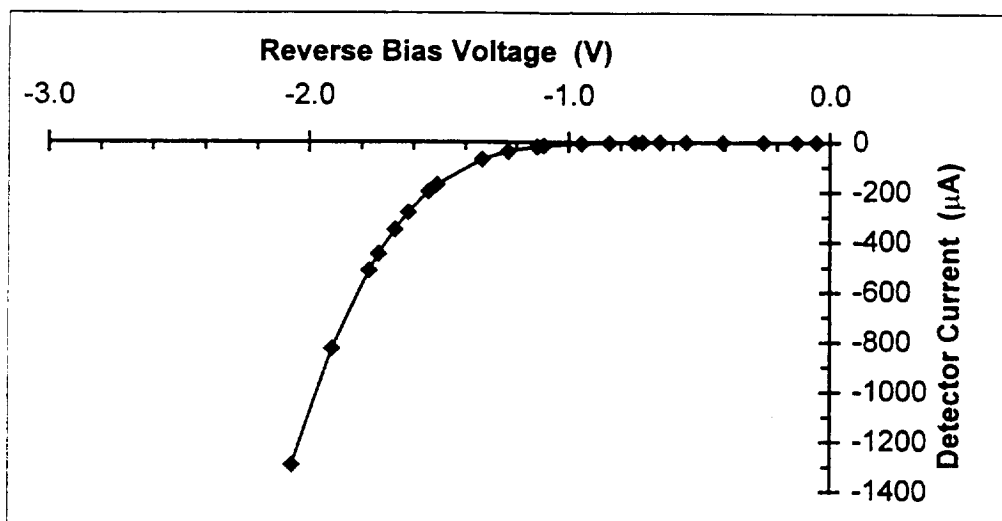
Optical Power=0.233 mW

Bias Current Monitor V_{Bi} (mV)	Bias Voltage Monitor V_B (mV)	Detector Voltage V_d (V)	Detector Current I_d (µA)	Detector Resistance R_d (Ω)
0.0	-138.0	0.13085	-139.113	
49.5	-91.3	0.08400	-141.935	63629.6
143.2	3.0	-0.01026	-141.331	221019.4
318.0	176.0	-0.18336	-143.145	170344.7
454.0	312.0	-0.31936	-143.145	140419.4
603.0	459.0	-0.46646	-145.161	66763.4
727.0	581.0	-0.58856	-147.177	134467.4
876.0	730.0	-0.73756	-147.177	92307.4
1009.0	860.0	-0.86772	-150.202	39359.4
1201.0	1047.0	-1.05498	-155.242	10363.0
1442.0	1255.0	-1.26469	-188.508	4311.9
1614.0	1382.0	-1.39402	-233.871	1996.7
1821.0	1506.0	-1.52232	-317.540	1237.4
2007.0	1596.0	-1.61730	-414.315	850.4
2220.0	1684.0	-1.71177	-540.323	625.4
2539.0	1791.0	-1.82976	-754.032	460.6
2987.0	1908.0	-1.96391	-1087.702	400.5
3000.0	1911.0	-1.96743	-1097.782	321.4
3417.0	2000.0	-2.07342	-1428.427	

Optical Power=0.443 mW

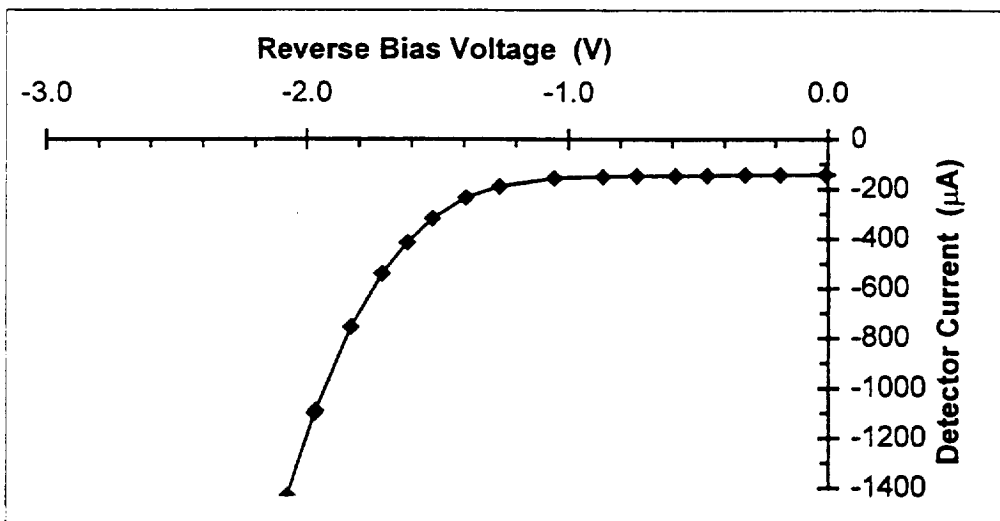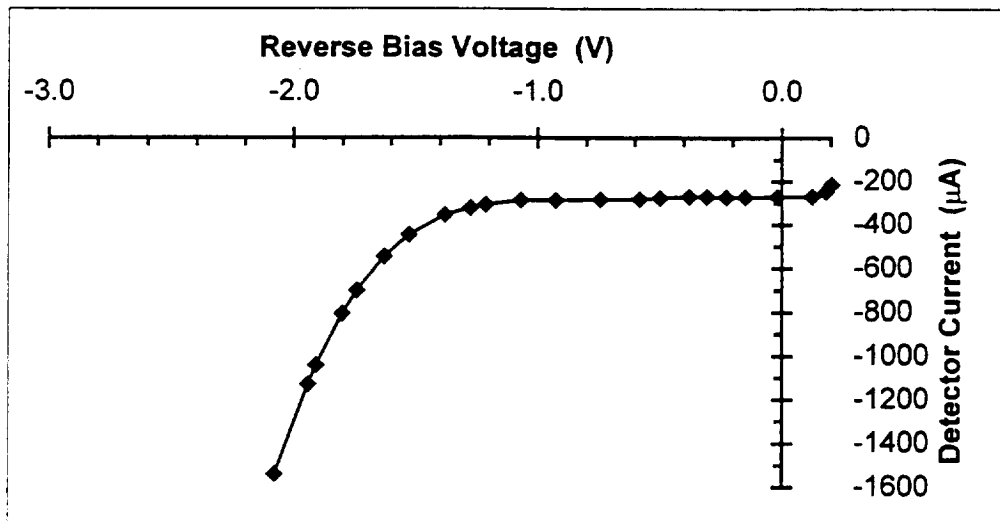| Bias Current Monitor V_{Bi} (mV)	Bias Voltage Monitor V_B (mV)	Detector Voltage V_d (V)	Detector Current I_d (μA)	Detector Resistance R_d (Ω)
0.0	-213.2	0.20215	-214.919	
51.3	-192.9	0.18025	-246.169	1422.7
129.6	-138.0	0.12413	-269.758	8068.4
273.8	5.1	-0.01902	-270.867	87507.4
406.0	135.3	-0.14933	-272.883	89288.3
483.0	212.0	-0.22604	-273.185	-57153.9
559.0	291.0	-0.30489	-270.161	-50209.9
632.0	364.0	-0.37789	-270.161	31630.1
756.0	482.0	-0.49620	-276.210	18268.1
845.0	566.0	-0.58046	-281.250	40888.7
1009.0	729.0	-0.74351	-282.258	68697.8
1196.0	912.0	-0.92672	-286.290	80899.4
1339.0	1055.0	-1.06972	-286.290	14187.4
1501.0	1197.0	-1.21275	-306.452	5645.2
1578.0	1258.0	-1.27458	-322.581	3440.7
1713.0	1361.0	-1.37924	-354.839	2027.3
1946.0	1503.0	-1.52595	-446.573	1300.6
2140.0	1599.0	-1.62703	-545.363	842.6
2399.0	1704.0	-1.74001	-700.605	669.0
2557	1759	-1.80035	-804.435	490.0
2885	1853	-1.90647	-1040.323	432.7
3000	1882	-1.93993	-1127.016	342.6
3524	1998	-2.07707	-1538.306	

Reverse Bias Voltage (V)

Optical Power=0.965 mW

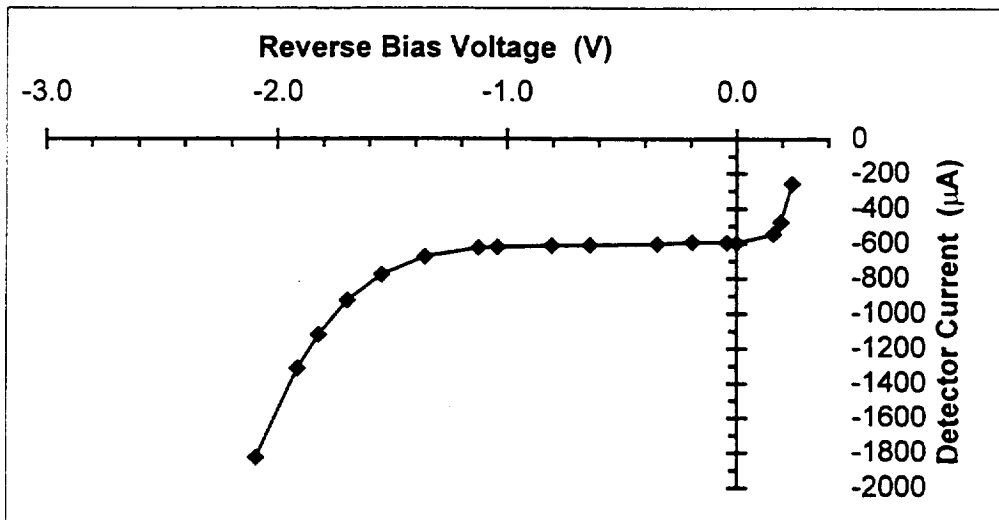| Bias Current Monitor V_{Bi} (mV)	Bias Voltage Monitor V_B (mV)	Detector Voltage V_d (V)	Detector Current I_d (μA)	Detector Resistance R_d (Ω)
0.0	-256.0	0.24274	-258.065	
256.0	-218.0	0.19344	-477.823	284.6
352.0	-189.0	0.16097	-545.363	1667.7
561.0	-29.0	-0.00157	-594.758	4429.1
601.0	14.0	-0.04442	-591.734	-38239.8
749.0	164.0	-0.19431	-589.718	33338.5
912.0	316.0	-0.34688	-600.806	23180.7
1211.0	607.0	-0.63830	-608.871	45683.4
1382.0	776.0	-0.80740	-610.887	39929.8
1623.0	1009.0	-1.04081	-618.952	26256.7
1711.0	1093.0	-1.12502	-622.984	5750.9
1994.0	1325.0	-1.35966	-674.395	2735.6
2278.0	1507.0	-1.54695	-777.218	1342.2
2567.0	1649.0	-1.69657	-925.403	796.9
2877.0	1764.0	-1.82167	-1121.976	557.7
3150.0	1846.0	-1.91357	-1314.516	386.8
3811.0	2000.0	-2.09384	-1825.605	

Optical Power=1.43 mW

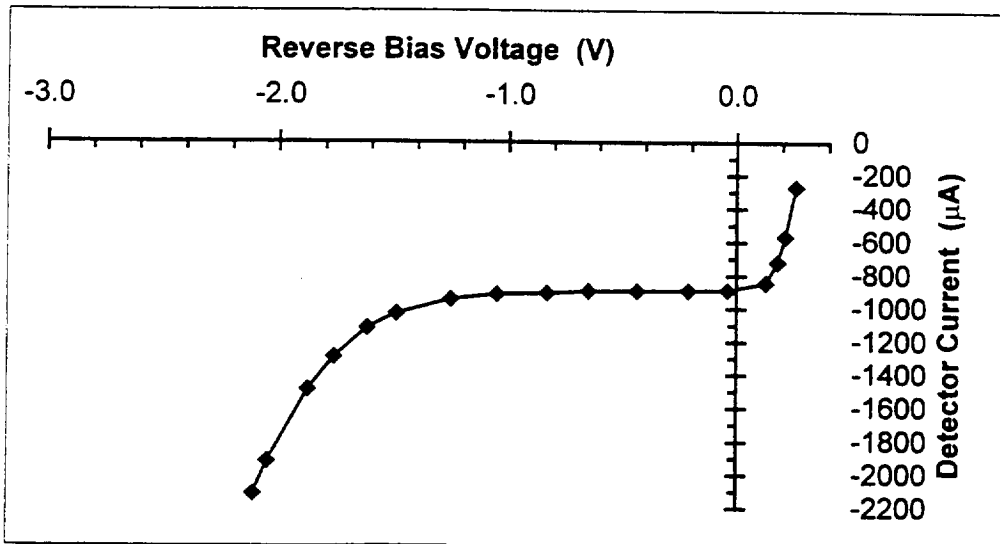| Bias Current Monitor V_{Bi} (mV)	Bias Voltage Monitor V_B (mV)	Detector Voltage V_d (V)	Detector Current I_d (μA)	Detector Resistance R_d (Ω)
0.0	-269.0	0.25506	-271.169	
325.0	-239.0	0.20978	-568.548	171.8
499.0	-215.0	0.17800	-719.758	297.6
667.0	-171.0	0.12758	-844.758	1291.4
877.0	-5.0	-0.04070	-889.113	7057.4
1054.0	168.0	-0.21391	-893.145	78617.8
1278.0	391.0	-0.43696	-894.153	432563.4
1491.0	604.0	-0.64996	-894.153	30269.2
1687.0	787.0	-0.83363	-907.258	18993.9
1913.0	1005.0	-1.05205	-915.323	10709.0
2145.0	1206.0	-1.25465	-946.573	3795.1
2462.0	1439.0	-1.49201	-1031.250	2081.3
2672.0	1560.0	-1.61762	-1120.968	1024.4
2979.0	1695.0	-1.76153	-1294.355	700.1
3279.0	1800.0	-1.87663	-1490.927	460.1
3853.0	1950.0	-2.04860	-1918.347	371.9
4098.0	2000.0	-2.10871	-2114.919	

Optical Power=2.00 mW

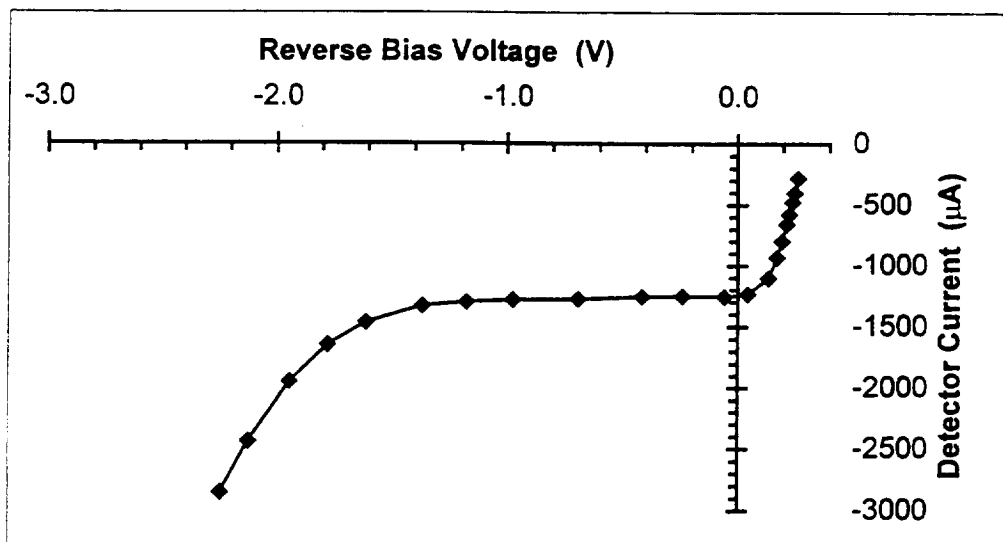| Bias Current Monitor V_{Bi} (mV)	Bias Voltage Monitor V_B (mV)	Detector Voltage V_d (V)	Detector Current I_d (μA)	Detector Resistance R_d (Ω)
0.0	-278.0	0.26360	-280.242	
129.0	-270.0	0.24933	-402.218	123.0
208.0	-264.0	0.23954	-475.806	130.8
318.0	-256.0	0.22626	-578.629	132.7
406.0	-249.0	0.21506	-660.282	145.7
560.0	-235.0	0.19381	-801.411	157.6
706.0	-220.0	0.17202	-933.468	194.1
902.0	-192.0	0.13531	-1102.823	429.6
1119.0	-106.0	0.04253	-1234.879	1271.8
1241.0	-5.0	-0.05956	-1256.048	15647.8
1420.0	177.0	-0.24141	-1253.024	
1597.0	351.0	-0.41556	-1256.048	19546.4
1895.0	629.0	-0.69460	-1276.210	20589.5
2183.0	910.0	-0.97596	-1283.266	17163.4
2406.0	1112.0	-1.17905	-1304.435	7510.5
2626.0	1301.0	-1.36965	-1335.685	2637.9
2994.0	1537.0	-1.61249	-1468.750	1305.0
3330	1694	-1.77877	-1649.194	692.7
3781	1846	-1.94626	-1950.605	437.6
4422	2000	-2.12549	-2441.532	330.0
4935	2099	-2.24595	-2858.871	

Optical Power=2.43 mW

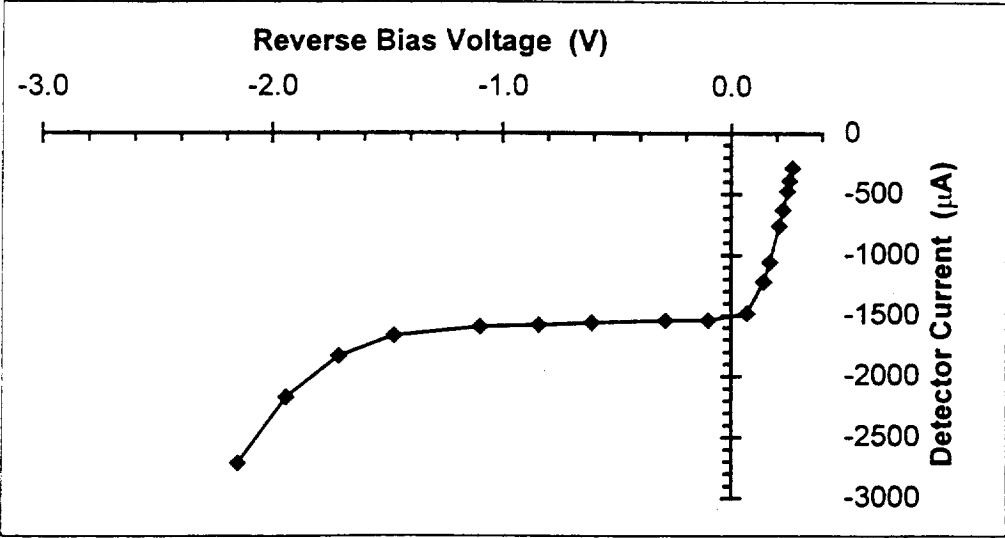| Bias Current Monitor V_{Bi} (mV)	Bias Voltage Monitor V_B (mV)	Detector Voltage V_d (V)	Detector Current I_d (μA)	Detector Resistance R_d (Ω)
0.0	-284.0	0.26928	-286.290	
112.0	-277.0	0.25684	-392.137	120.0
201.0	-271.0	0.24654	-475.806	122.6
366.0	-260.0	0.22756	-631.048	125.3
504.0	-250.0	0.21093	-760.081	138.0
827.0	-223.0	0.16859	-1058.468	151.3
1007.0	-204.0	0.14125	-1220.766	237.1
1328.0	-144.0	0.06773	-1483.871	761.8
1551.0	23.0	-0.10217	-1540.323	6106.0
1740.0	210.0	-0.28928	-1542.339	22912.5
2080.0	530.0	-0.61031	-1562.500	14824.2
2328.0	761.0	-0.84219	-1579.637	14690.9
2600.0	1017.0	-1.09902	-1595.766	7345.5
3038.0	1386.0	-1.47160	-1665.323	2590.8
3433.0	1616.0	-1.71015	-1831.653	924.6
3980.0	1827.0	-1.93856	-2170.363	496.9
4701.0	2009.0	-2.14848	-2713.710	

Optical Power=2.93 mW

Bias Current Monitor V_{Bi} (mV)	Bias Voltage Monitor V_B (mV)	Detector Voltage V_d (V)	Detector Current I_d (μA)	Detector Resistance R_d (Ω)
0.0	-287.0	0.27213	-289.315	
55.0	-285.0	0.26738	-342.742	109.4
308.0	-270.0	0.24005	-582.661	115.7
400.0	-264.0	0.22960	-669.355	120.3
616.0	-250.0	0.20513	-872.984	125.1
805.0	-236.0	0.18206	-1049.395	140.7
1185.0	-203.0	0.13108	-1399.194	159.9
1383.0	-179.0	0.09807	-1574.597	341.6
1724.0	-81.0	-0.01253	-1819.556	1020.9
1905.0	79.0	-0.17361	-1840.726	14707.4
2213.0	377.0	-0.47213	-1850.806	11254.2
2618.0	734.0	-0.83162	-1899.194	11985.9
3060.0	1159.0	-1.25750	-1916.331	4867.9
3549.0	1506.0	-1.61186	-2059.476	1273.9
4232.0	1806.0	-1.93170	-2445.565	702.9
4548.0	1902.0	-2.03910	-2667.339	418.8
4935.0	1996.0	-2.14828	-2962.702	
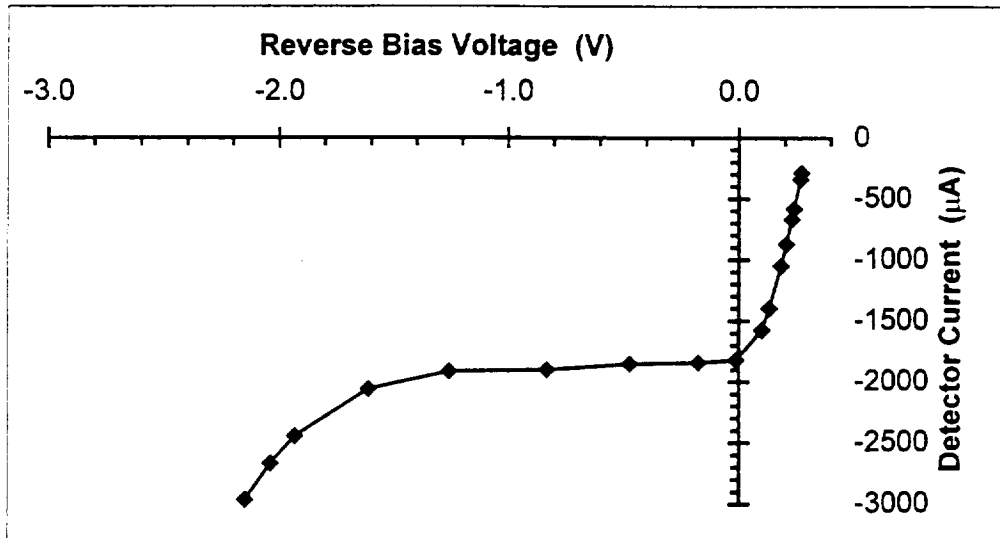
FAMILY OF V-I CURVES
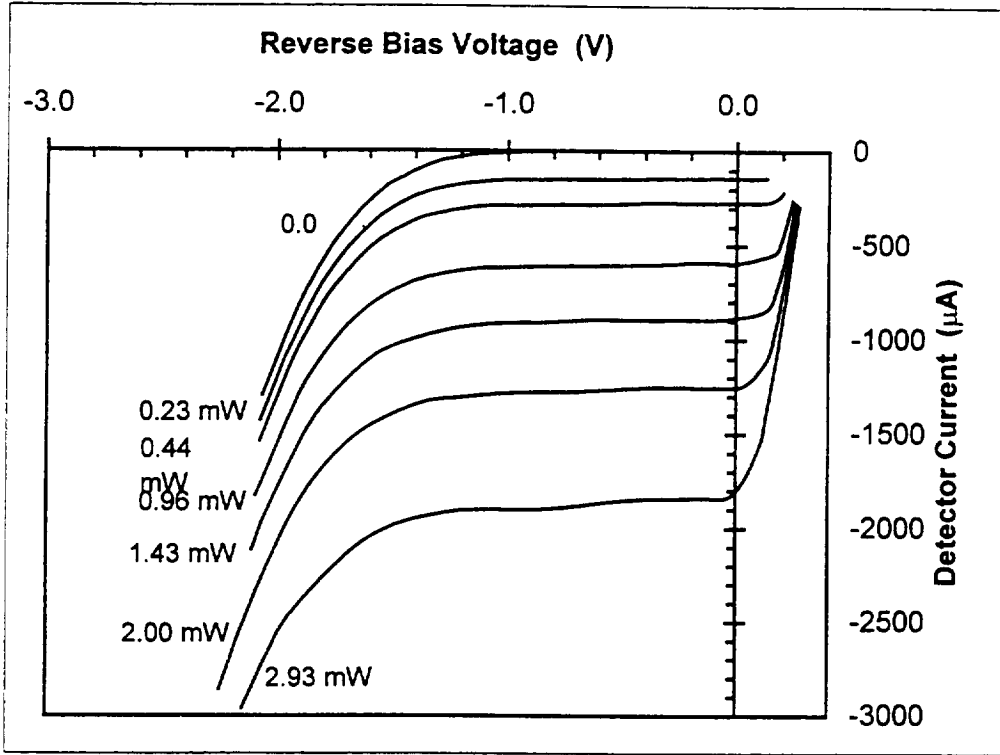
FREQUENCY RESPONSE MEASUREMENTS

VB= 0.0 V
amplifier bias=8.9mV

Frequency (MHz)	Beam #1 (mV)	Beam #2 (mV)	Het. Sig. (RMS mV)	Frequency Response	Detector RC Model	Het. Qum. Efficiency		MS Error
0					1.00			
6	76.2	22.8	1.84	0.97	0.997391	0.584792		0.000878
20	75.9	22.8	1.86	0.98	0.978402	0.60025		4.28E-06
40	76.3	22.9	2.06	1.08	0.922721	0.726678		0.02436
60	76.4	22.9	2.02	1.06	0.847889	0.697697		0.043755
100	76.3	22.9	1.84	0.96	0.692762	0.579754		0.073345
120	76.6	23.2	1.44	0.74	0.62501	0.346096		0.014279
140	76.5	23.2	1.26	0.65	0.565889	0.265371		0.007402
150	76.5	23.2	1.07	0.55	0.539428	0.191373		0.000201
160	76.5	23.2	0.85	0.44	0.514878	0.120768		0.005638
180	76.4	23.2	0.67	0.35	0.470976	0.075146		0.015391
200	76.5	23.1	0.65	0.34	0.433114	0.071119		0.009144
220	76.4	23	0.57	0.30	0.400318	0.05516		0.010629
250	76.2	23	0.56	0.29	0.358833	0.0534		0.004408
275	75.7	23	0.54	0.28	0.329922	0.050025		0.002197
300	76.2	23	0.52	0.27	0.305094	0.046043		0.001125
350	76.3	23	0.46	0.24	0.2648	0.035978		0.000613
400	76.6	23	0.3	0.16	0.233626	0.015235		0.005995
450	75.2	23	0.17	0.09	0.208865	0.004995		0.014261
500	74.8	23.1	0.12	0.06	0.188759	0.002486		0.015789
							MS Error	0.0086

C_d=32.8 pF
BW=96 MHz
RC Model

ηAC/ηDC vs Frequency (MHz)
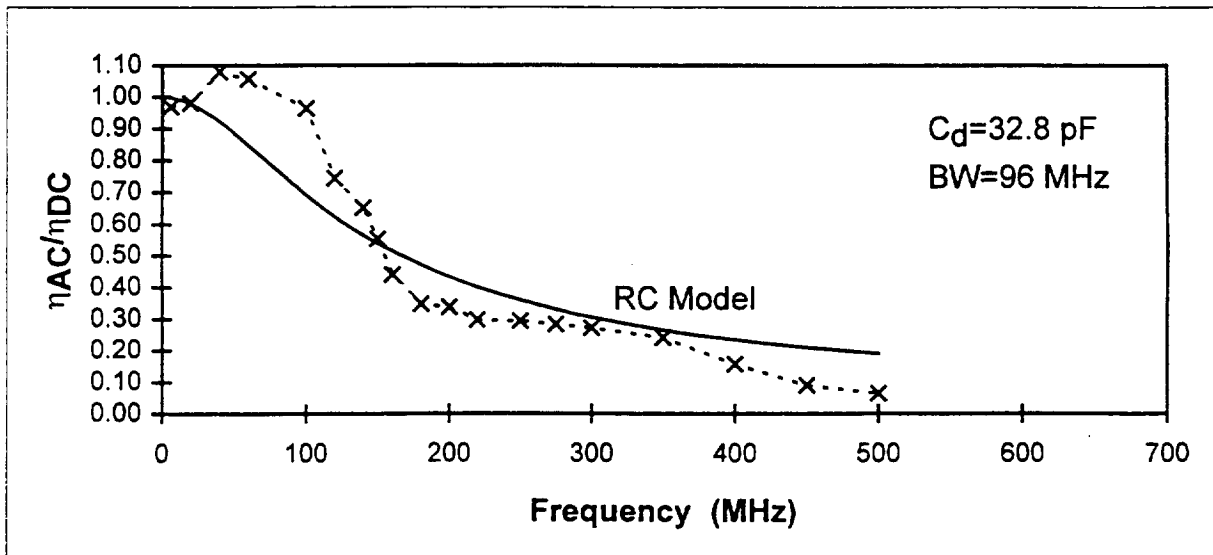
VB=-0.25 V

amplifier bias= 8.2mV

Frequency (MHz)	Beam #1 (mV)	Beam #2 (mV)	Het. Sig. (RMS mV)	Frequency Response	Detector RC Model	Het. Qum. Efficiency	
0					1.00		
10	75.3	21.8	1.80	0.96	0.996024	0.573693	0.001405
25	75.6	21.8	1.86	0.99	0.979196	0.60985	8.25E-05
40	76.6	22.1	1.98	1.03	0.950082	0.666278	0.006874
120	77	22.1	1.86	0.97	0.714314	0.584546	0.064133
140	76.6	22.1	1.72	0.90	0.658525	0.502784	0.057035
150	76.6	22.1	1.35	0.70	0.63258	0.309736	0.005145
175	77	22.1	0.93	0.48	0.573553	0.146136	0.008059
200	77	22.1	0.91	0.47	0.522429	0.139919	0.002406
225	77.3	22.1	0.76	0.39	0.478299	0.09717	0.007024
250	76.1	22.1	0.73	0.38	0.440153	0.091234	0.003353
275	76.1	22.1	0.7	0.37	0.407048	0.083889	0.001641
300	76.6	22.1	0.7	0.37	0.378169	0.083276	0.000168
350	76.4	22.1	0.62	0.32	0.330479	0.065521	4.28E-05
400	76.1	22.1	0.4	0.21	0.292943	0.027392	0.006971
450	76.1	22.1	0.22	0.12	0.262769	0.008286	0.021777
500	75.8	22.1	0.17	0.09	0.238055	0.00497	0.022154

MS Error 0.011571
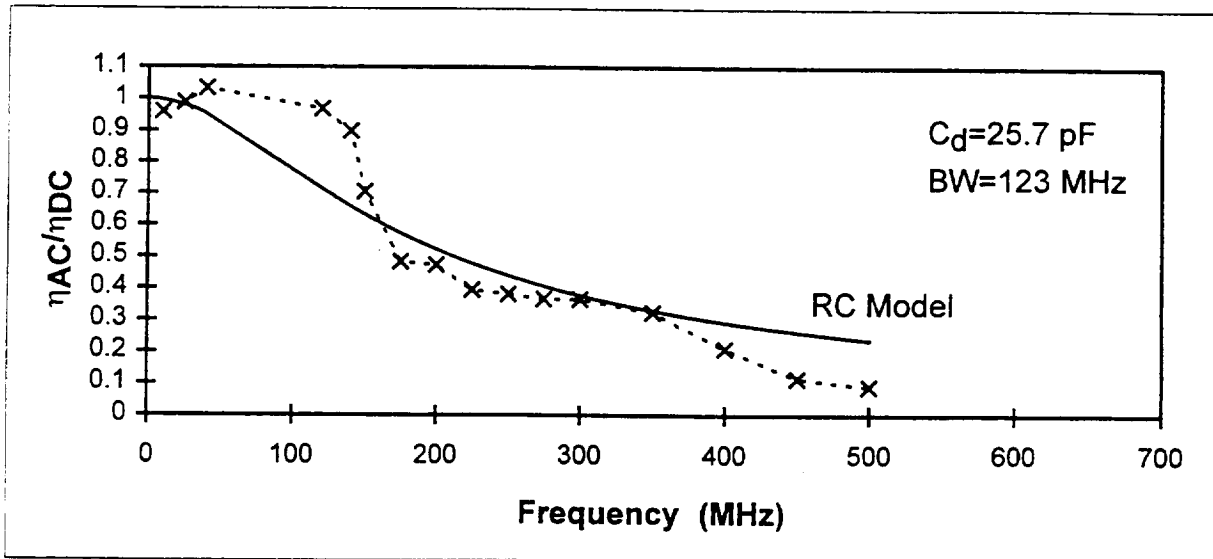
C_d=25.7 pF

BW=123 MHz

RC Model

amplifier bias= 8.2mV

Frequency (MHz)	Beam #1 (mV)	Beam #2 (mV)	Het. Sig. (RMS mV)	Frequency Response	Detector RC Model	Het. Qum. Efficiency	
0					1.00		
10	77.0	22.1	1.87	0.97	0.996562	0.590848	0.000566
30	77.0	22.1	1.95	1.01	0.975218	0.642483	0.001533
50	77.9	22.1	2.01	1.04	0.936347	0.673814	0.0105
130	77.4	22.1	1.97	1.02	0.717476	0.651939	0.092622
150	77.3	22.1	1.8	0.93	0.665999	0.545064	0.071992
175	77.9	22.1	1.2	0.62	0.607787	0.240165	0.000154
200	78.3	22.1	1.1	0.57	0.556481	0.200654	0.000108
250	78.3	22.1	0.89	0.46	0.472324	0.131354	0.000187
300	78.3	22.1	0.83	0.43	0.407761	0.11424	0.000399
350	77.9	22.1	0.62	0.32	0.357489	0.064111	0.001373
400	77.2	22.1	0.56	0.29	0.317597	0.052833	0.000713
430	77.3	22.1	0.48	0.25	0.297465	0.03876	0.002334
450	77.3	22.1	0.32	0.17	0.285343	0.017227	0.014219
500	76.5	22.1	0.26	0.14	0.258816	0.011506	0.015147
550	134.6	22.4	0.38	0.14	0.236663	0.013	0.008533
600	134	22.4	0.36	0.14	0.217913	0.011723	0.006544
650	160	22.4	0.33	0.11	0.201856	0.008163	0.007659
700	159.3	22.3	0.28	0.10	0.187961	0.005946	0.008168
750	186.7	22.3	0.2	0.06	0.175825	0.002568	0.012476
800	186.7	18.5	0.14	0.05	0.16514	0.001723	0.012682
850	185.5	18.5	0.13	0.05	0.155662	0.001495	0.01139
900	181.6	18.5	0.09	0.03	0.147201	0.000733	0.012756
						MS Error	0.013275

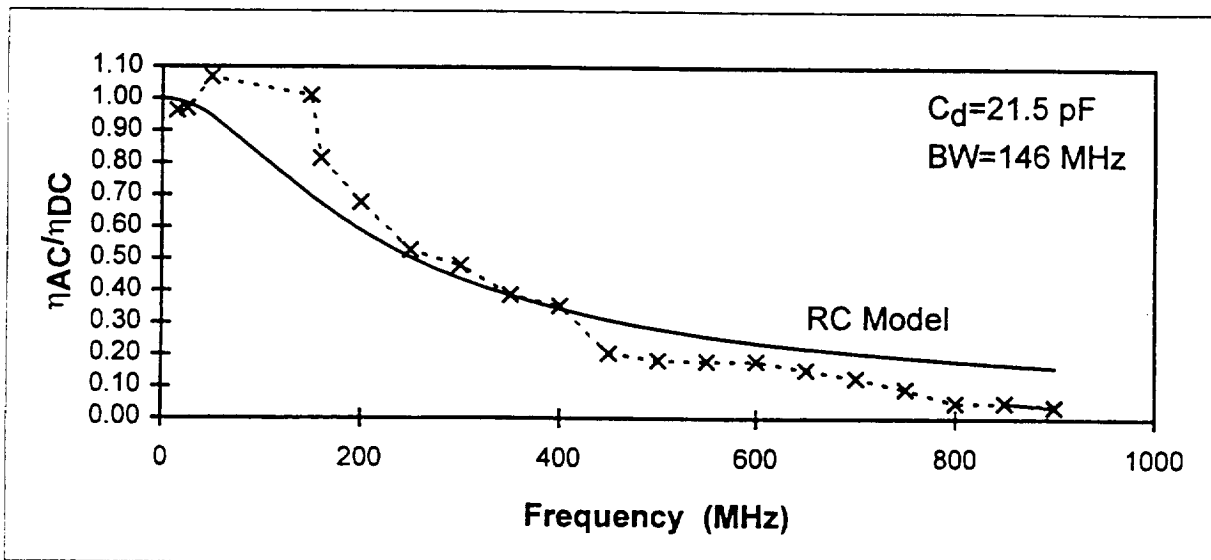

C_d=23.5 pF

BW=134 MHz
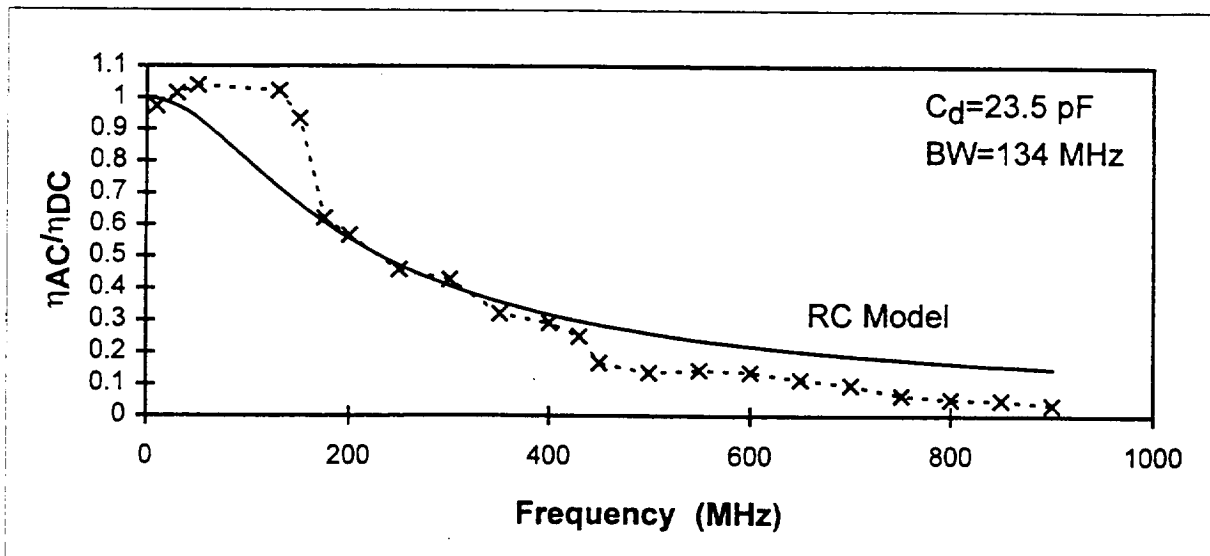
RC Model

VB= -0.75 V

amplifier bias= 8.6mV

Frequency (MHz)	Beam #1 (mV)	Beam #2 (mV)	Het. Sig. (RMS mV)	Frequency Response	Detector RC Model	Het. Qum. Efficiency	
0					1.00		
15	106.0	17.9	1.80	0.96	0.994132	0.577961	0.001026
25	106.7	17.9	1.82	0.97	0.985089	0.58666	0.000249
50	107.2	17.9	2.01	1.07	0.945763	0.711915	0.014889
150	109.2	17.6	1.89	1.01	0.698237	0.637498	0.097467
160	107.6	16.2	1.39	0.82	0.674848	0.414932	0.019695
200	109.2	16.4	1.18	0.68	0.590521	0.286726	0.007591
250	109.2	16.4	0.92	0.53	0.505235	0.174293	0.000534
300	147.7	14.7	0.87	0.48	0.438496	0.144138	0.001761
350	147.7	14.7	0.7	0.39	0.385832	0.093311	5.55E-07
400	147.7	14.7	0.64	0.35	0.343654	0.078001	9.58E-05
450	147.7	14.7	0.37	0.20	0.309327	0.02607	0.011024
500	147.7	14.7	0.33	0.18	0.280958	0.020738	0.009744
550	148.2	14.9	0.33	0.18	0.25718	0.020008	0.006111
600	148.7	14.9	0.33	0.18	0.236999	0.019936	0.0034
650	147.7	14.9	0.28	0.15	0.219677	0.014456	0.004559
700	145.7	14.9	0.23	0.13	0.204662	0.009896	0.006204
750	147.7	14.9	0.17	0.09	0.19153	0.005329	0.009831
800	145.6	14.9	0.09	0.05	0.179953	0.001516	0.017075
850	144.3	15	0.09	0.05	0.169675	0.001507	0.014532
900	146.1	15	0.07	0.04	0.160492	0.0009	0.015014
850	185.5	18.5	0.13	0.05	0.169675	0.001559	0.014329
900	181.6	18.5	0.09	0.03	0.160492	0.000764	0.015752
						MS Error	0.012313

Chart: η_{AC}/η_{DC} vs Frequency (MHz), with RC Model curve. $C_d=21.5$ pF, BW=146 MHz.
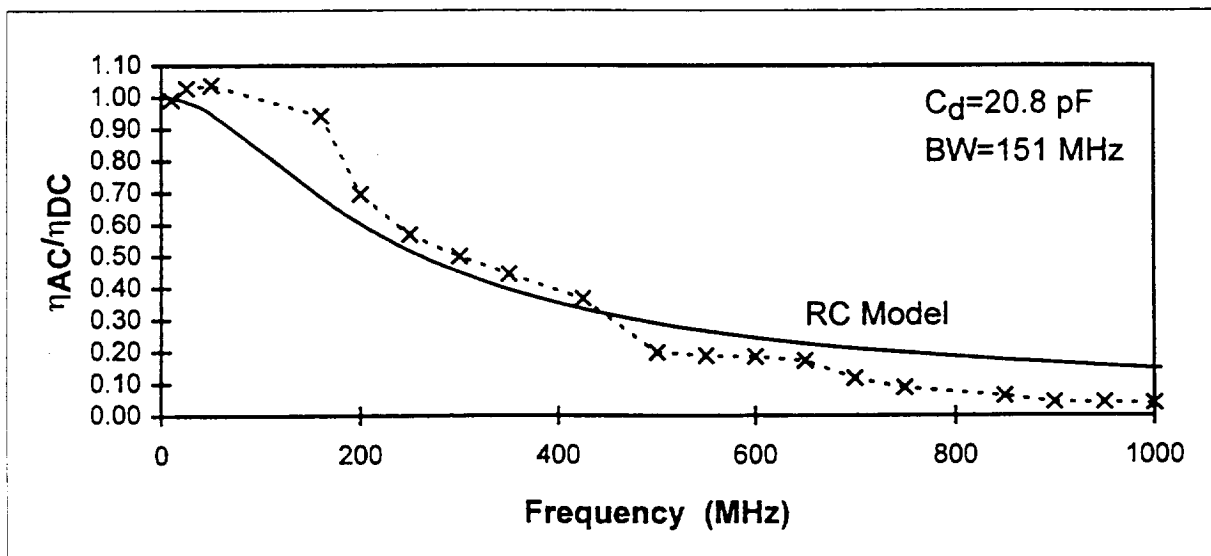
VB= -1.0 V

amplifier bias= 10.5mV

Frequency (MHz)	Beam #1 (mV)	Beam #2 (mV)	Het. Sig. (RMS mV)	Frequency Response	Detector RC Model	Het. Qum. Efficiency	
0					1.00		
10	95.2	19.7	1.72	0.99	0.997157	0.613453	3.55E-05
25	94.8	19.7	1.78	1.03	0.985978	0.660116	0.001783
50	95.2	19.9	1.82	1.04	0.948924	0.672244	0.007864
160	95.5	19.3	1.6	0.94	0.686864	0.553011	0.064636
200	99.5	22.8	1.43	0.70	0.603168	0.301837	0.008483
250	99.5	22.8	1.17	0.57	0.517668	0.202056	0.00262
300	99.9	22.8	1.03	0.50	0.450239	0.155893	0.002443
350	100.7	22.8	0.92	0.44	0.396744	0.123271	0.002264
425	100.6	22.8	0.76	0.37	0.335337	0.084216	0.001019
500	114.6	22.8	0.44	0.20	0.289588	0.024431	0.008424
550	115.6	22.8	0.42	0.19	0.265195	0.022049	0.005972
600	113.8	22.8	0.41	0.19	0.244468	0.021378	0.003533
650	128.2	22.8	0.41	0.17	0.226662	0.018762	0.002843
700	128.2	22.8	0.28	0.12	0.211214	0.00875	0.008618
750	175.3	21.2	0.23	0.09	0.197697	0.004847	0.012009
850	172.8	21.2	0.16	0.06	0.175186	0.002382	0.012864
900	173.2	21.5	0.11	0.04	0.165721	0.001092	0.01535
950	173.8	21.1	0.11	0.04	0.157214	0.00113	0.013152
1000	173.8	21.1	0.1	0.04	0.149527	0.000933	0.01229
1050	173.2	21.1	0.08	0.03	0.142548	0.0006	0.012445

MS Error 0.009932

C_d=20.8 pF
BW=151 MHz
RC Model

$\eta AC/\eta DC$

Frequency (MHz)

5.0 RELATED ACTIVITIES

5.1 TECHNICAL AND REVIEW MEETINGS

UAH personnel attended the NOAA Working Group on Space-Based Lidar Winds Meeting in Daytona Beach, Florida, January 21-23, 1997. In this meeting, the status of the NASA/MSFC and UAH 2-micron solid state coherent lidar efforts were described in these meetings. UAH personnel also attended meetings at the "Office of the Mission To the Plant Earth" in the NASA Headquarters on December 17, 1996, and the DOD/DOC/NASA Integrated Program Office (IPO) in Washington, DC, on January 10, 1997. In these meetings, the status of MSFC and UAH coherent lidar activities were reported and The results of the lidar alignment study was presented.

5.2 CONFERENCES

A conference paper, describing some of the work performed under this deliver order, was prepared and presented at the the Coherent Laser Radar Topical Meeting in Linkoping, Sweden, June 23-26, 1997. The summary of this paper is provided in fllowing pages.

DEVELOPMENT OF SOLID STATE COHERENT LIDARS
FOR GLOBAL WIND MEASUREMENTS

Farzin Amzajerdian
The University Of Alabama in Huntsville
Center for Applied Optics
Huntsville, Alabama 35899, USA
farzin.a@msfc.nasa.gov
(205) 895-6030 Ext. 452

Michael J. Kavaya
NASA Marshall Space Flight Center
Electro-Optics Branch, Mail Code EB53
Huntsville, AL 35812, USA
michael.kavaya@msfc.nasa.gov
(205) 544-8453

Abstract

Several key coherent lidar technologies have recently been developed, creating new possibilities for the development of compact, low power, and reliable wind lidar systems suitable for deployment in space. In this paper, the current state of the solid state coherent lidar technology and the status of the space-based systems development effort at NASA/MSFC will be discussed.

Summary

INTRODUCTION

Over the past 4 years, NASA Marshall Space Flight Center has been working; with collaboration with NASA Langley Research Center, Jet Propulsion Laboratory, University of Alabama in Huntsville, and private industry; toward further advancing solid state coherent Doppler lidar technology for global measurement of atmospheric winds from space platforms. This effort has resulted in the development of a number of key technologies creating new possibilities for the development of compact, low power, and reliable 2-micron coherent lidar systems suitable for deployment in space. By utilizing these technologies, three different spaceborne lidar

instruments have been designed and proposed; one as a technology demonstrator, another as an operational prototype stepping stone towards the development of a long-life-time operational instrument, and the third as a NPOESS 7-year life operational instrument. In this paper, the recent advances in the development of the key lidar components will be briefly described and the ongoing effort toward the development of the three space instruments will be described.

LIDAR SYSTEM

The solid state coherent lidar system design is illustrated in Figure 1. The transmitter laser uses a part of the output beam of a low power, continuous wave (CW) laser (seed or injection oscillator) to generate stable, single frequency pulses. The transmitter laser pulses are then expanded by an off-axis, afocal telescope before being deflected by 30 degrees by an optical element. If the desired scan pattern is continuous conical, then the scanner optical element is continuously rotated by a precision motor to provide a conical pattern in the atmosphere. The remaining part of the seed laser output beam is used for frequency locking of a programmable, frequency-agile CW local oscillator (LO) laser. The output of this laser is directed to the optical detector to be mixed with the signal beam. In order to compensate for the large Doppler shift due to the spacecraft motion and minimize the required bandwidth of the detector and receiver, the frequency of the LO laser is varied about the seed laser frequency with the azimuth angle of the conical scan. The lidar optical train includes a small rotating wedge (derotator) and a steering mirror (beam misalignment compensator or BMC). The derotator rotation is synchronized with the scanner to compensate for the signal beam misalignment due to the scanner continuous motion during the pulse round trip time. The derotator is not required if a a step-stare scan pattern is utilized. The BMC, through an active control system, corrects for the misalignments due the scanner motion during the pulse reception time and the change in the spacecraft inertial nadir pointing angle during the pulse round trip time. After passing through the derotator and BMC, the returned photons are launched into a fiber to be combined in a fiber coupler with the local oscillator beam. The output of the fiber optic coupler is focused onto a high-quantum efficiency, wideband detector optimized for heterodyne detection.

TECHNOLOGY DEVELOPED

The recent development of several key lidar components includes the demonstration of a 500 mJ diode-pumped transmitter laser at LaRC, a 25 mW frequency-agile local oscillator laser with tunability range of 8 GHz at JPL, and a 25 cm compact and thermally stable telescope at UAH and MSFC. The ongoing effort includes the development of a wideband, low-noise heterodyne receiver, a low-mass diffractive scanner, a compact wedge scanner, the signal beam derotator and BMC, a robust lidar structure at UAH and MSFC, and a 500 mJ transmitter laser at Coherent Technologies Inc (CTI). Many of these lidar components will be integrated into a complete lidar system in the near future, allowing the demonstration of all the developed technologies based on the space operational requirements.

Taking advantage of the progress in the development of all the key lidar technologies, MSFC has developed two different space instrument designs. One is a 100 mJ, 25 cm instrument designed for a Space Shuttle mission aimed at demonstrating the coherent lidar technology readiness for global wind profiling. The second instrument is a 500 mJ, 50 cm coherent lidar, suitable for a

relatively short duration free flyer or Shuttle mission, with the purpose of demonstrating the coherent lidar winds and aerosols measurement capabilities, and its autonomous and efficient operation in space. These instruments will establish a progressive path toward the development and deployment of a long life-time operational instrument that is very similar to the second instrument. The table below summarizes the status of the required technologies for these missions.
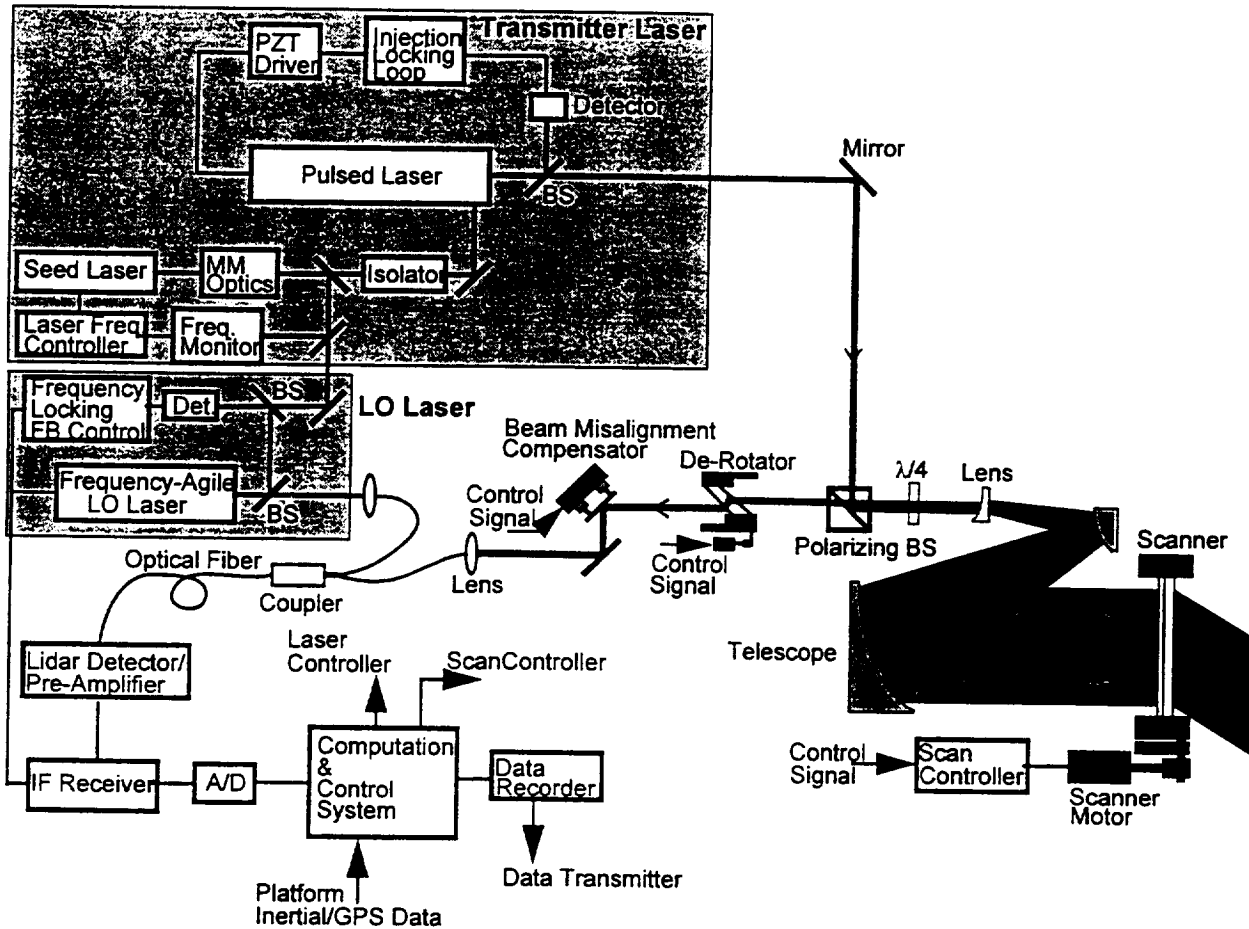

Figure 1. Solid State Coherent Doppler Lidar System Diagram.

In this paper, an overview of the recent progress in the development of the enabling technologies for space-based solid state coherent lidars will be provided. The designs of space-based instruments will be discussed, and the status of the first technology demonstrator instrument development will be reported.

ACKNOWLEDGMENTS

Technology	Status	Plan
Transmitter Laser	100 mJ, 6 Hz, fl. lamp-pumped (CTI, 93)	Build upon for Mission 1
	500 mJ, 10 Hz, diode-pumped (LaRC, 97)	Ground-based demonstrator system. Build upon for Mission 1. Perform technology demonstration measurements for Missions 2 and 3.
	500 mJ, 10 Hz, diode-pumped (CTI, 98)	Engineering model for Mission 2
Frequency-agile Local Oscillator Laser	25 mW, 8 GHz cont. tunability (JPL, 97)	Upgrade for mission 1
Compact Telescope	25 cm off-axis (UAH/MSFC, 96)	Use for Mission 1
	50 cm unit design (UAH, 96)	Missions 2 and 3
Scanner	28 cm Wedge Scanner (MSFC, 96)	Use for Mission 1
	5 cm experimental Diffractive Optical Element (DOE) (UAH/MSFC 97) 30 cm DOE Scanner (UAH/MSFC 98)	Develop for Missions 2 and 3
Derotator	Experimental unit (UAH/MSFC 97)	All missions if continuous conical scanning is chosen
Beam Misalignment Compensator	Experimental unit (UAH 97)	Use for all Missions
Receiver	Characterized and analyzed InGaAs detectors (UAH/MSFC 95) Fiber optic interferometer and balanced detectors evaluation (UAH/MSFC 97)	Use for all missions
Data Acquisition/ Processor and Controller Unit	Hardware Design (MSFC 98) Algorithm Development (MSFC 98) Hardware/software integration and test (MSFC 99)	Use for all missions with appropriate modifications

REFERENCES

1. Michael J. Kavaya et al, "Direct global measurements of tropospheric winds employing a simplified coherent laser radar using fully scalable technology and technique," SPIE Proceedings Vol. 2214, 1994.
2. A. Ahmad, F. Amzajerdian, C. Feng and Y. Li, "Design and fabrication of a compact lidar telescope", SPIE Proceedings Vol. 2832, pp. 34-42, 1996
3. htto://eo.msfc.nasa.gov/